AN OPTICAL STORAGE CAVITY-BASED, COMPTON-BACKSCATTER X-RAY SOURCE USING THE MKV FREE ELECTRON LASER

A DISSERTATION SUBMITTED TO THE GRADUATE DIVISION OF THE UNIVERSITY OF HAWAIʻI AT MĀNOA IN PARTIAL FULFILLMENT OF THE REQUIREMENTS FOR THE DEGREE OF

DOCTOR OF PHILOSOPHY

IN

PHYSICS

DECEMBER 2012

By
Michael R. Hadmack

Dissertation Committee:

Eric B. Szarmes, Chairperson
John M.J. Madey
Luis R. Elias
Gary S. Varner
Ralf I. Kaiser

To my daughter Adella.
May this work serve as an inspiration
to live a life full of curiosity and wonder of the unexplored.

Acknowledgments

Throughout my years at the University of Hawai‘i I have had the help and support of many people in my Ph.D. work. I would like to express my sincere gratitude by acknowledging them here. This dissertation could not have been written without all of you. In particular, I would like to thank the following:

My advisor and committee chair Professor Eric Szarmes, for providing me with these research opportunities. It was Eric's course in optics that inspired me to pursue a career in free electron laser technology. Thank you for sharing your optics expertise and novel ideas on optical storage cavities with me, and for your constant encouragement. Without your support and mentoring this manuscript would not exist.

Professor John Madey, for his technical expertise and advice in electronics, microwave, and accelerator systems. John's decades of practical experience in a multitude of fields have made him an invaluable resource throughout my studies. Thanks for the many hours of discussion while sitting in the FEL control room, which have led to many of the developments described in this dissertation, particularly the e-Beam Phase Stabilization System.

Professor Gary Varner, for his expertise in electronics and detector technologies, and for his extensive and helpful comments on this manuscript. Gary's "Electronics for Physicists" course is responsible for bringing my electronics skills from the level of a hobbyist to those of a professional, and I am very grateful for what this has brought to my career. I also appreciate the valuable insights that Gary's 'outsider' perspective and high energy physics experience brings to our weekly investigator's meetings.

Thank you to Professors Luis Elias and Ralf Kaiser for taking the time out of your busy schedules to serve on my Ph.D. committee and for reviewing this manuscript.

In addition, I would like to thank Dr. Barry Lienert for his work on the design of the e-Beam Phase Stabilization Sysetm and for performing Zemax simulations for the Optical Storage Cavity. Many past graduate students have provided valuable insight into

the arduous Ph.D. process. In particular, I have benefitted from long conversations with Bryce Jacobson, Jeremy Kowalczyk, Shidong Kan, Huan Ma, and Troy Hix. I appreciate all of the support and encouragement Bryce and Jeremy have given me over the years and the many hours they have given supporting me in experimental operations and troubleshooting, as well as being good friends.

This research could not have been completed without funding from our sponsors, the Department of Defense (contract DASG60-02- C-0048) and the Department of Homeland Security (agreement 20120-DN-077-AR1045-02). I am also grateful to the ARCS Foundation of Honolulu for their generous Doris and Robert Pulley Award.

Thank you to the staff of the UH Physics Department machine shop. Over the years, Roy Tom, Germano Zerbini, and Curtis McLennan have uncomplainingly put up with my illegibly scribbled drawings for impossible to make parts and constant change requests. Without you guys I never would have been able to design and build any of the custom hardware discussed throughout this dissertation, and more. Working closely with the machinists has greatly improved my skills in mechanical design, enabling me to go to them with proper CAD drawings for parts that are actually possible to fabricate. Similarly, thanks again to Bryce for teaching me to TIG weld, a skill that has been invaluable in designing vacuum systems that don't leak.

Thank you to Susan Madey, Margie Kidani and the rest of the UH Physics Department staff for their for assistance in navigating the UH bureaucracy and making sure that I always received a pay check.

I also owe my gratitude to the vast open source software community. In particular, the late John D. Hunter, author of the matplotlib[1] toolkit used to produce nearly every graphic in this dissertation. Also, thanks to Fernando Perez and the iPython[2] team for the iPython Notebook, which has revolutionized and streamlined my data analysis workflow.

Finally, thank you to my family. My wonderful wife Sarah has tirelessly supported me through the seemingly never ending Ph.D. process. I cannot thank her enough for constantly encouraging me to continue through even the roughest patches of my graduate career, even while confronted with the challenges of her own career and new motherhood. Without her editing skills, this dissertation would probably make me look embarrassingly illiterate. To my beautiful daughter Adella, my Mom and Stan, and Don and Diane, thank you for your limitless love and support.

Abstract

A compact, high-brightness x-ray source is presently under development at the University of Hawai'i Free Electron Laser Laboratory. This source utilizes Compton backscattering of an infrared laser from a relativistic electron beam to produce a narrow beam of monochromatic x-rays. The scattering efficiency is greatly increased by tightly focusing the two beams at an interaction point within a near-concentric optical storage cavity, designed with high finesse to coherently stack the incident laser pulses and greatly enhance the number of photons available for scattering with the electron beam.

This dissertation describes the effort and progress to integrate and characterize the most important and challenging aspects of the design of this system. A low-power, near-concentric, visible-light storage cavity has been constructed as a tool for the exploration of the performance, alignment procedures, and diagnostics required for the operation of a high power infrared storage cavity. The use of off-axis reflective focussing elements is essential to the design of the optical storage cavity, but requires exquisite alignment to minimize astigmatism and other optical aberrations. Experiments using a stabilized HeNe laser have revealed important performance characteristics, and allowed the development of critical alignment and calibration procedures, which can be directly applied to the high power infrared storage cavity. Integration of the optical and electron beams is similarly challenging. A scanning-wire beam profiler has been constructed and tested, which allows for high resolution measurement of the size and position of the laser and electron beams at the interaction point. This apparatus has demonstrated that the electron and laser beams can be co-aligned with a precision of less than 10 µm, as required to maximize the x-ray production rate. Equally important is the stabilization of the phase of the GHz repetition rate electron pulses arriving at the interaction point and driving the FEL. A feed-forward amplitude and phase compensation system has been built and demonstrated to substantially improve the uniformity of the electron bunch phase, thus enhancing both

the laser performance and the beam stability required for efficient x-ray production. Results of all of these efforts are presented, together with a summary of future work.

Table of Contents

List of Tables

List of Figures

List of Acronyms

ADC Analog–to–Digital Converter

DAC Digital–to–Analog Converter

CW Continuous Wave

FEL Free Electron Laser

FSR Free Spectral Range

FWHM Full Width Half Maximum

HeNe Helium-Neon Laser

IP Interaction Point

RF Radio Frequency

LO Local Oscillator

TDL Tunable Diode Laser

FPGA Field Programmable Gate Array

STRL Stabilized Tunable Reference Laser

BPM Beam Position Monitor

SWBPM Scanning Wire Beam Position Monitor

RAM Residual Amplitude Modulation

TEM Transverse Electromagnetic (mode)

FIR Finite Impulse Response

LVDT Linear Variable Differential Transformer

Chapter 1

Introduction

1.1 Background and Motivation

The growing demand for intense sources of narrow bandwidth x-rays and gamma rays has led to a proliferation of synchrotron facilities around the world in recent decades. Research in diverse fields are driven by requirements for highly coherent x-ray sources for x-ray holography. In particular, the fields of genomics, proteiomics, and pharmacology, are now demanding even higher brightness photons with shorter pulse durations than are possible with existing storage ring type machines. To meet these needs, a first generation of x-ray free electron lasers is being commissioned by the Linac Coherent Light Source (LCLS) at SLAC and by XFEL at DESY. The XFEL, while still under construction, is truly a next generation accelerator light source employing state of the art accelerator technology. The LCLS relies on the proven, but, half-century old accelerator technology present at SLAC and has already revolutionized research using x-rays. These large, costly machines are typically only available to users at national labs and resources are limited not only in scheduling, but also they also have such high peak photon fluxes at low repetition rates that sample survival and photon detection are real problems. To fill the demand for high-brightness photons for all fields of research there is interest in low cost compact light sources. The MkV Free Electron Laser Laboratory at the University of Hawai‘i is presently developing a compact x-ray source utilizing Compton backscattering that meets these demands *and* produces high brightness photons with reduced *peak* power by operating at GHz pulse repetition rates[4].

This dissertation examines several aspects of the development of a compact, monochromatic, high-energy photon source based on the Compton backscattering of high energy electrons from a GHz train of picosecond laser and electron pulses, also known as Laser

Compton Scattering (LCS). Compton backscattering of electrons from a laser was first proposed shortly after the invention of the laser by Arutyunian[5] and Milburn[6]. In 1965 the effect was first demonstrated using a ruby laser[7], but due to the low power lasers and extraordinarily low scattering cross section, no practical applications had been developed until recently. Today LCS has been used in a variety of applications such as particle beam cooling and emittance measurements in addition to serving as a source of photons for other research. Fast, bright sources of x-rays are particularly valued for time-resolved, high-resolution, high-contrast crystallography and proteinography.

The principle limitation of LCS sources is the required intensity of laser pulses to generate useful photon fluxes. High-power, chirped-pulse amplification, solid-state lasers are capable of producing multi-terrawatt femtosecond pulses, but only at very low repetition rates and with exceedingly complex and costly laser systems. The high *peak* photon fluxes generated by TW laser-based sources are problematic in applications due to their high peak power and broad energy spectrum. High peak power leads to nonlinear harmonic generation effects, sample damage and detector pulse pile-up which are undesirable for most applications. Since high average brightness is the most important characteristic in most applications this is a compromise inherent to TW laser scattering. An optical storage cavity takes advantage of the great enhancement of optical power possible when many coherent optical pulses with high repetition rate interfere constructively in a Fabry-Perot resonant cavity (see Figure 1.1). Optical storage cavity based systems can be optimized for use with GHz repetition rates lasers and accelerators, thus achieving high *average* brightness with reduced *peak* power. These same techniques and storage cavity technologies can be readily extending to the gamma-ray regime by only increasing the energy of the electron beam used. This brings the benefits of GHz repetition rate and high average brightness photons to interesting problems in the field of nuclear spectroscopy.

This dissertation is the culmination of a six year effort to examine the challenges involved in the development and operation of an optical storage cavity-based light source. While the entirety of the research performed cannot be described here, the following chapters will address several key system developments in detail.

The outline of this dissertation is as follows. The remainder of this chapter provides an introduction to Compton-backscatter light sources and demonstrates that the MkV FEL accelerator facility provides a unique and ideal test-bench for this technology. Chapter 2 describes the development of technologies required for the practical realization of a

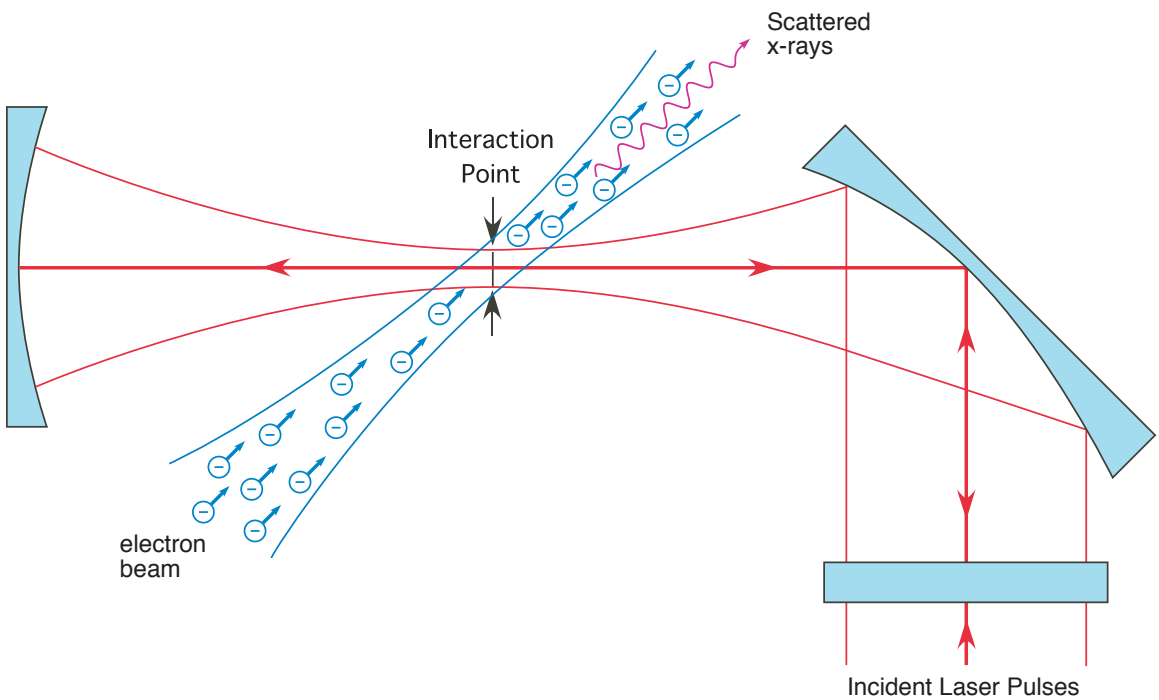

Figure 1.1: Laser pulses stored within an high finesse (i.e. low loss) optical resonator (storage cavity) are collided with a relativistic electron beam to produce x-rays via Compton backscattering.

Compton-backscatter light source using an optical storage cavity. The design of a suitable high power storage cavity is presented followed by a review of experiments testing the performance of a low-power test cavity. Chapter 3 covers the design and implementation of a stabilized tunable reference laser (STRL). This system serves an important role in synchronizing and stabilizing the storage cavity and its pump laser. Chapter 4 presents a system to stabilize the electron beam current and bunch phase. This is accomplished using a feed-forward stabilization loop that corrects ripples on the high power RF drive used to accelerate the electron beam. The bunch phase stability is of particular importance for both the efficiency of the free electron laser and synchronization with the optical storage cavity. Finally, Chapter 5 reviews the design and commissioning experiments for a scanning wire beam profiler (SWBPM). This device is used to coordinate the alignment and focusing for the electron and laser beams at the x-ray interaction point with a degree of precision sufficient to optimize the x-ray flux produced.

1.2 High Brightness X-ray Sources

The most commonly used figure of merit for advanced light sources is the *spectral brightness* defined as photon flux per unit source area per unit solid angle with a given spectral bandwidth. The standard units given are:

$$\text{photons/sec/mm}^2\text{/mrad}^2\text{/0.1\%BW}$$

There are around 70 synchrotron light sources operating around the world today providing spectral coverage from the infrared to gamma-rays including 16 facilities in the United States[8]. Most of these facilities are storage rings with numerous undulator insertion devices designed to produced radiation with the desired characteristics.

Despite the large number of simultaneously operating beamlines and high uptime of these facilities, demand is high and scheduling for beam time is competitive. Additionally, most of these facilities are government operated, making proprietary research difficult.

The most advanced light sources available today are the Linac Coherent Light Source (LCLS) at SLAC in California and the European XFEL at DESY in Germany. The LCLS, commissioned in 2009, has turned the SLAC National Accelerator Facility into a free electron laser. These machines differ from conventional FELs by using the Self Amplification of Stimulated Emission (SASE) process of single pass laser gain rather than using an optical

resonator. Photons are produced in the energy range 0.48 keV to 9.5 keV with pulse lengths less than 200 fs[9]. The XFEL is a 1.7 km long, 17.5 GeV superconducting linear accelerator driving a 100 m undulator SASE FEL. It will produce radiation in the range 0.05 nm to 6 nm with pulses shorter than 100 fs. The XFEL will be commissioned in 2015 at a cost of over a billion euro[10].

There is demand within private industry for compact, inexpensive sources of high-brightness photons which could be independently owned and operated. Since research performed at national labs must by law be in the public domain, proprietary research is impractical; the pharmaceutical industry, for example, would prefer to have the capabilities to study proprietary samples away from the eyes of their competitors. New opportunities are also possible in the field of medical imaging, especially since the patient would not need to be taken to a national lab for study.

This desire for numerous compact high-brightness light sources has fueled the development of many laser Compton scattering devices. By reducing the period of the undulators used in synchrotron sources to that of an optical undulator with periods on the order of 1 µm, the particle beam energy required to generate high energy photons is reduced from the GeV range to MeV's. The cost and complexity of the accelerator facilities are reduced by orders of magnitude. With most of these initiatives focused on the use of TW lasers, the problems of low repetition rates and excessive peak power discussed above will likely prevent them from becoming the practical research tools that are demanded.

The COBALD LCS source at Daresbury will use an electron beam comparable to that of the MkV FEL and is expected to produce 10^{21} photons/sec/mm^2/mrad^2/0.1%BW peak brightness x-rays. However, this system relies on a 10 TW laser system with a pulse repetition rate of only 1 kHz. Even with its high peak brightness the very low average brightness of 10^{10} photons/sec/mm^2/mrad^2/0.1%BW is not useful for many applications[11]. Other LCS sources based on multi-terawatt lasers have similar characteristics, often with repetition rates as low as 0.1 Hz. The x-ray source under development at the University of Hawai‘i has the same projected peak brightness of 10^{21}, with an average brightness of 10^{14} photons/sec/mm^2/mrad^2/0.1%BW with GHz repetition rate pulses.

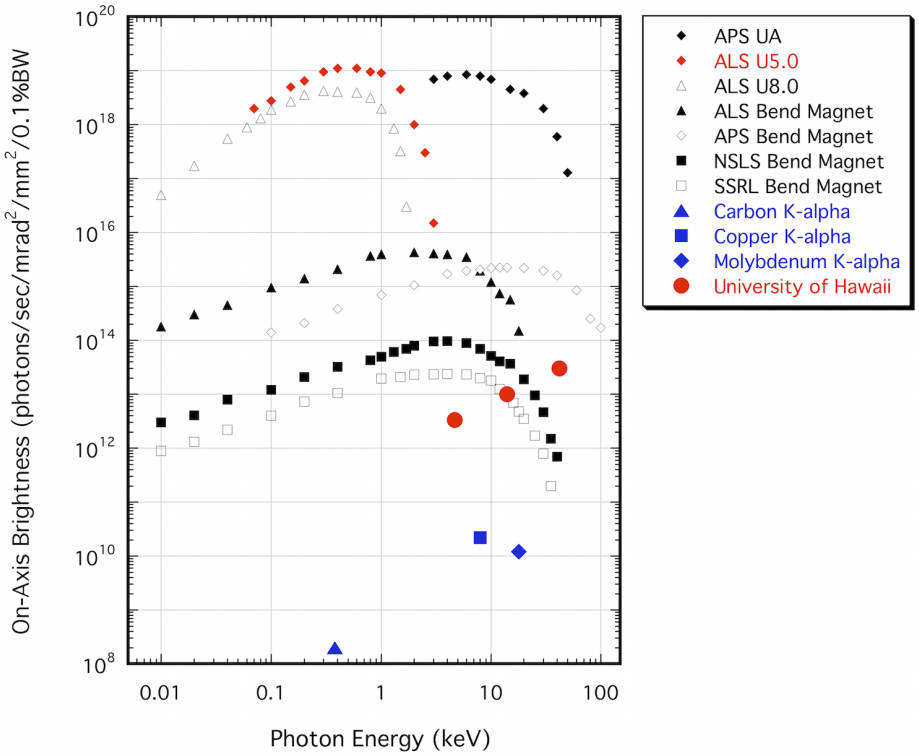

Figure 1.2: Comparison of the UH x-ray source brightness with various synchrotron beamlines and conventional x-ray source [Courtesy of E. Szarmes].

1.3 Optical Storage Cavities

The brightness of a laser Compton source can be substantially enhanced through the use of an optical storage cavity. Various proposed and realized projects have used optical storage cavities to enhance laser intensity for Compton backscatter applications using electron storage rings. These systems rely on long bow-tie cavities due to the MHz repetition rates of storage rings, but cannot focus tightly.

While there has been some interest in extracting the enhanced stored energy in a storage cavity, optical storage cavities are ideal for applications such as laser Compton scattering where low interaction cross sections enable utilization of the stored beam without perturbing it. Cavity based laser Compton sources have been discussed as the means of generating the two opposing beams for a future γ-γ photon collider at the ILC[12].

Optical storage cavities also have promising applications in the high-field quantum electrodynamics (QED). The PVLAS experiment[13], for example, set out to measure the magnetic birefringence of the vacuum using an optical cavity in a strong magnetic field. Strong-field QED effects, such as vacuum birefringence and vacuum pair production, require laser intensities in excess of $10^{29}\,\mathrm{W\,cm^{-2}}$, and are beyond the reach of today's petawatt lasers[14]. Optical storage cavity technology has the potential to provide the highly focused, stored laser power necessary to observe these effects.

The novel optical storage cavity design discussed in Chapter 2 is based on a UH invention by Professor Eric Szarmes[15] and is unique in its ability to simultaneously control the synchronism of the optical pulses in the cavity with the pump laser and maintain a tight focus at the cavity waist. The use of the free electron laser as a pump also guarantees that the laser and electron pulses are synchronous at 3 GHz repetition rates.

Little attention has been paid to the development of optical storage cavities optimized for use with high repetition rate lasers and electron beams. Most work has focused on long cavities matched to MHz storage ring repetition rates. The TW lasers and photocathode-driven accelerators at the heart of most Compton backscatter sources have repetition rates of no more than tens of kHz. These repetition rates are unsuitable for storage cavities of practical size and these systems must rely on single pass interactions only with the associated problems due to peak power and spectral broadening of the radiation.

Experiments performed at Stanford have demonstrated the feasibility of achieving an energy enhancement of FEL micro-pulses using an external storage cavity[16]. These

experiments were focused on Q switching applications where stored pulse energy must be extracted from the cavity. For LCS applications energy extraction from the cavity is not a problem since the interaction is too weak to disturb the Q of the optical cavity.

1.4 Compton Backscattering

The Compton Backscattering interaction (alternatively known as Inverse Compton Scattering, Laser Compton Scattering, Relativistic Thomson Scattering, etc.) can be understood as Thomson Scattering in the electron rest frame which is upshifted into the lab frame. In the rest frame of a relativistic electron incident electromagnetic radiation with wavelength λ_0 has its energy Lorentz-boosted by a factor of 2γ corresponding to a wavelength $\lambda_0/2\gamma$. This wave then induces a dipole oscillation as it travels past the electron, which in turn generates electric dipole radiation transverse to the polarization of the incident wave. Another Lorentz transformation into the lab frame collapses the dipole field into a narrow cone of width $1/\gamma$ and upshifts the frequency by another factor of 2γ. For a head-on collision the scattered pump laser photons experience a peak energy upshift factor of $4\gamma^2$ when backscattered at 180° (peak of the radiation cone)[6].

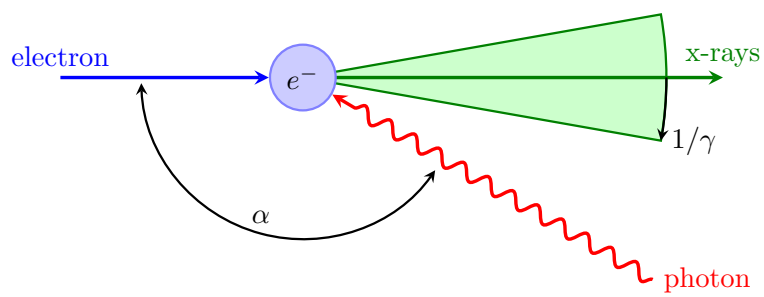

Figure 1.3: An incident photon scatters off of an electron in to a cone of half-angle $1/\gamma$ with an energy upshift $4\gamma^2$

Assuming laser and electron pulses of duration τ with well matched gaussian transverse profiles of radius w_0, the probability of a single photon Thomson scattering into the forward direction from a single electron in its rest frame is given by

$$\mathcal{P} = \frac{\frac{1}{2}\sigma_T}{\frac{1}{2}\pi w_0^2} \tag{1.1}$$

where σ_T is the Thomson cross section for an electron and πw_0^2 is the effective area of the gaussian profile beam profile over the interaction length. The number of photons in a pump

laser pulse with peak power P_0 and wavelength λ_0 is

$$N_0 = \frac{P_0 \tau \lambda_0}{hc} \tag{1.2}$$

where λ_0/hc is the photon energy. We can then apply the probably $\mathcal{P}$ to find the number of scattering events per electron passing through the laser pulse volume.

$$n = \mathcal{P} N_0 \tag{1.3}$$

Since the resulting upshifted x-rays have energy $4\gamma^2 hc/\lambda_0$, the total energy radiated per electron is

$$E_x = \frac{4\gamma^2 \tau_0 \sigma_T P_0}{\pi w_0^2} \tag{1.4}$$

Electrons arrive at the rate $dN_e/dt = I_e/e$ where the peak pulse current I_e is in amperes so the radiated x-ray power is

$$P_x = E_x \frac{dN_e}{dt} = \frac{4\gamma^2 \tau_0 \sigma_T P_0 I_e}{e\pi w_0^2} \tag{1.5}$$

It is also convenient to express the power in terms of the number of pump radiation cycles N_w and pump laser peak intensity I_0 as

$$P_x = \frac{2\gamma^2 \sigma_T \lambda_0 N_w I_0 I_e}{ec} \tag{1.6}$$

Application of this theory to a strong laser pulse and optimized interaction region yields an estimate of the radiated x-ray photon flux and spectrum but neglects coherent effects as the number of photons becomes large. A strong coherent laser pulse can be viewed as an optical undulator, in which case, electron beam micro-bunching can result in coherent emission. X-ray brightness may be enhanced by several orders of magnitude[17].

1.5 The MkV Free Electron Laser Laboratory

The MkV Free Electron Laser Laboratory at the University of Hawai‘i provides an ideal environment for the investigation and development of technologies for use with next-generation light sources. A 40 MeV S-band RF linear accelerator is used to accelerate electrons from a thermionic microwave gun. The resulting low emittance micro-bunched electron pulses drive an infrared FEL. The electron beamline was constructed with a 10 m long drift space between the linac and FEL. This so-called ‘diagnostic chicane’ provides

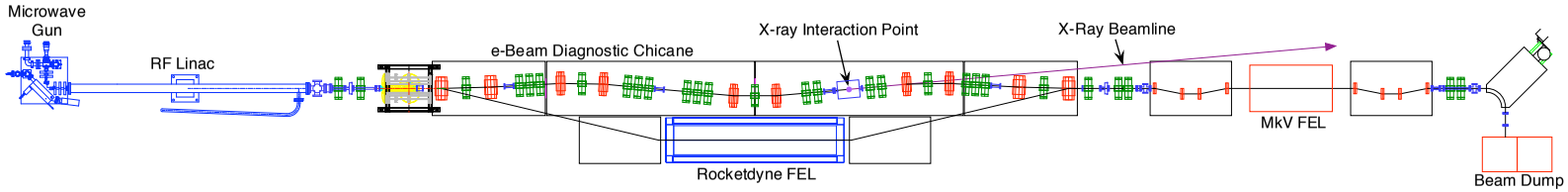

Figure 1.4: Scale drawing of the MkV FEL beamline with dipole steering magnets indicated in red and focusing quadrupoles in green. The x-ray beam is drawn in purple and extends to the x-ray detectors located outside the shielding walls.

several locations for the installation of insertion devices along with appropriate focusing magnets and diagnostic instrumentation. The diagnostic chicane serves two main purposes: 1) it provides non-intercepting, real-time electron beam diagnostics and 2) provides the bend in the beamline required for x-ray extraction[18]. The Compton-backscatter x-ray source is housed in a custom vacuum chamber installed at an insertion point aligned to the x-ray extraction beamline and is described in detail in Appendix B.

The MkV FEL is ideally suited for use as a Compton backscatter x-ray source. The high peak power picosecond pulses from the phase-locked FEL provide a number of benefits over the solid state lasers used in other LCS systems. Without a material gain medium (i.e. only vacuum), the free electron laser is able to produce a very high spatial quality TEM_{00} beam, a quality almost unheard of in solid state lasers, but essential for coupling to a high finesse storage cavity. Additionally, the high GHz range repetition rate of the FEL micro-pulses allows for pulse stacking in a relatively short storage cavity. Experiments using GHz rep rate x-ray bunches will also benefit from the possibility of RF heterodyne detection and lock in amplification, both significantly reducing the effects of background and $1/f$ noise. Because the GHz pulse trains are limited to macro-pulse lengths less than 10 µs, the finesse of the storage cavity does not need to be greater than about 2000. Table 1.1 lists the parameters for the fully optimized Compton backscatter x-ray source using an optical storage cavity.

Figure 1.5: The accelerator vault contains the MkV FEL systems. The SLAC-type linac is shown in the foreground followed by the electron spectrometer and diagnostic chicane.

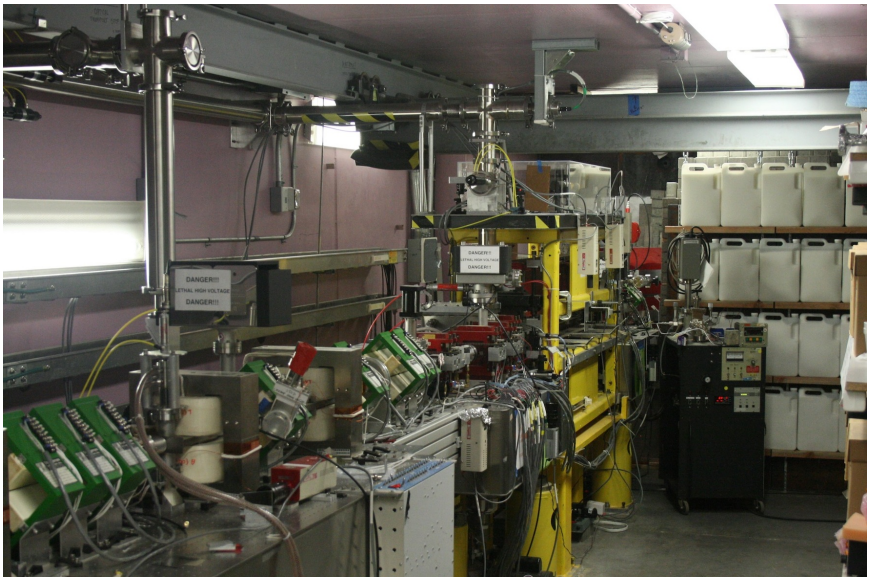

Figure 1.6: The MkV free electron laser is located at the far end of the vault following the diagnostic chicane. The yellow frame is the support structure for the undulator magnet. The steel pipes in the upper left are part of the laser optical transport system. The white jugs at the back are supplemental boron impregnated neutron shielding for the beam dump.

Table 1.1: MkV FEL X-ray Source Parameters

Parameter	Symbol	Value	Unit
Electron Energy	E_e	40	MeV
Relativistic Mass Factor	γ	78	
Peak Laser Power	P_0	8	MW
Beam Radius	w_0	30	µm
μ-Pulse Rep Rate	f_{RF}	2856	MHz
μ-Pulse Duration	τ_0	1	ps
Ω-Pulse Rep Rate	f_Ω	10	Hz
Ω-Pulse Duration	τ_Ω	4	µs
Pump Laser Wavelength	λ_0	3	µm
Storage Cavity Finesse	$\mathcal{F}$	2000	
Stored Optical Power	P_s	16	GW
Peak X-ray Energy	E_x	10.1	keV
X-ray Wavelength	λ_x	0.117	nm
X-ray Average Power	P_x	1	W
Average X-ray Brightness	$\mathcal{B}$	10^{14}	photons/sec/mm^2/mrad^2/0.1%BW

Chapter 2

Optical Storage Cavity

2.1 Introduction

It is evident from the earlier discussion of Compton backscatter x-ray production rates that interaction efficiency is intrinsically low and that very high laser pump powers and electron beam currents are necessary to achieve useful x-ray fluxes. The laser power, electron beam current, and focal parameters can be chosen to optimize the x-ray flux, but with limitations. First, by tightly focusing a high current electron beam, space charge forces will significantly reduce the emittance of the electron beam resulting in a spectral broadening of the x-rays. Second, for pump laser normalized vector potentials greater than unity, the longitudinal velocity of the electron bunches will become sufficiently modulated that a significant amount of radiated power will appear in harmonics rather than at the desired fundamental wavelength. These effects put a fundamental limit on the peak power radiated from such an x-ray source while maintaining the desired high spectral brightness. Attempting to achieve higher peak powers will increasingly diminish the purity and utility of the source. The only solution to this limitation is to focus on the development a high *average* power source[4].

Most laser Compton scattering x-ray sources developed to date have relied on ultra-high peak-power, chirped-pulse amplification, terawatt lasers. Such systems are indeed capable of reaching and exceeding the peak power limit discussed above. However, repetition rates of terawatt laser systems, and thus, their average powers, are far too low while the peak x-ray fluxes are often too high to be useful in applications. The HERCULES terawatt laser as a Compton backscatter source will have a normalized vector potential of 50 which will result in significant higher harmonic generation reducing the spectral purity of the

x-ray photons[19, 20]. While the peak power will be impressive, the average brightness, considering the rep-rate of 0.1 Hz, will be rather low.

An alternative approach, which appears to offer an optimal compromise between peak and average power to yield optimal brightness, is the use of a high repetition rate laser such as a mode-locked free electron laser[4]. The MkV FEL at the University of Hawai‘i is a quasi-CW mode-locked laser producing $> 100\,\mathrm{mJ}$, $4\,\mu\mathrm{s}$ macro-pulses at 10 Hz with each macro-pulse composed of 1 ps micro-pulses mode-locked at 2.856 GHz for a peak power of 8.8 MW. While 100 mJ at 10 Hz is a lower average power than the single shot TW laser, it is the 3 GHz micro-pulse repetition rate of coherent micro-pulses of the mode-locked FEL that enables the use of an optical resonator or "storage cavity" to further enhance the peak power available for x-ray generation.

Coherent FEL micro-pulses injected into an optical resonator consisting of a pair of high reflecting mirrors are allowed to circulate and interfere constructively with subsequently injected micro-pulses. The long photon lifetimes in a high finesse cavity allow for a buildup of power proportional to the finesse. For a resonator of finesse $\mathcal{F}$, laser pulses are stored for $n_{1/e^2} = \mathcal{F}/\pi$ passes. Due to the low Compton backscatter cross-section, the electron beam does not appreciably deplete the field in an optical cavity, and thus, does not add any appreciable cavity loss. This allows efficient "pulse stacking" to occur inside the cavity. From Section 1.4, the single pass energy loss of the pulses circulating in the storage cavity is equal to the scattering probability P_x. For the reference systems parameters this is a loss of $\delta = 4 \times 10^{-12}$ which is negligible compared with the mirror losses of the order 1×10^{-3}. This technique does, however, require laser pulse coherence over a number of pulses comparable with the finesse, thus making the mode-locked free electron laser the ideal pump[21].

This chapter describes the development of technologies required for the practical realization of an optical undulator based light source using an optical storage cavity. First, in Section 2.2, the conceptual design of a three-mirror optical storage cavity, which is suitable for x-ray generation, is described along with a four-mirror variant. Next, a visible light, low-power, storage cavity test-bench is presented in Section 2.3. A detailed account is given of the assembly and alignment of this cavity with observations and analysis of the performance. Finally, the goals for a high power storage cavity test-bench are outlined in Section 2.4. Appendix A discusses the strategies for stabilization of the high power storage cavity and presents the planned stabilization system design. Appendix B describes the

development and operation of a vacuum chamber used as a test-bed for ongoing studies of techniques used for the alignment of the electron and pump laser beams and the testing of emerging detector technologies.

2.2 High Power Optical Storage Cavity

2.2.1 Three-Mirror Storage Cavity

In order to maximize the brightness of the x-ray source, a storage cavity must simultaneously be resonant with the laser source, be focussed very tightly, and have a length synchronized to the pump laser repetition rate. In a two mirror Fabrey-Perot cavity these goals are essentially impossible to satisfy simultaneously since the cavity length defines both the resonant frequencies of the cavity and transverse focal properties of the cavity mode. Additionally, for pulsed lasers, the round trip transit time for optical pulses in the cavity ($\tau = \frac{2L}{c}$) must match precisely to the pulse repetition interval ($\tau = 1/f_{\text{rep}}$) which is difficult to achieve simultaneously with a tight focus. Figure 2.1 illustrates pulse stacking in both the time and frequency domains. The cavity spectrum is an infinite comb (modulated by the transmittance and reflectances of the optics) of resonances separated by the free spectral range ($\nu_{\text{ax}} = c/2L$). Varying the cavity length L causes the entire comb of modes to expand, increasing ν_{ax} and the offset of a given mode. A mode-locked laser also has a comb of frequencies in its spectrum with the separation given by the repetition rate and had an envelope determined by the pulse duration. Efficient pulse stacking requires that the spacing and relative phase of these two frequency combs overlap. A three-mirror cavity provides the necessary extra degree of freedom to meet these requirements[15].

In the three-mirror storage cavity shown in Figure 2.2, one of the spherical mirrors is replaced with an off-axis paraboloid. The paraboloid focusing geometry is constructed such that the diverging beam from the cavity waist is collimated and deflected off-axis. The effect achieved is equivalent to the replacement of one spherical cavity mirror with a lens and a flat mirror, but without the loss and dispersion associated with an intra-cavity refractive element. A flat third mirror completes the cavity and also serves as the input coupler. Since the beam is large and collimated by the paraboloid, the flat mirror is able to translate longitudinally, changing the overall cavity length, thus tuning the cavity resonances and synchronous length without altering the transverse focusing at the interaction point. The

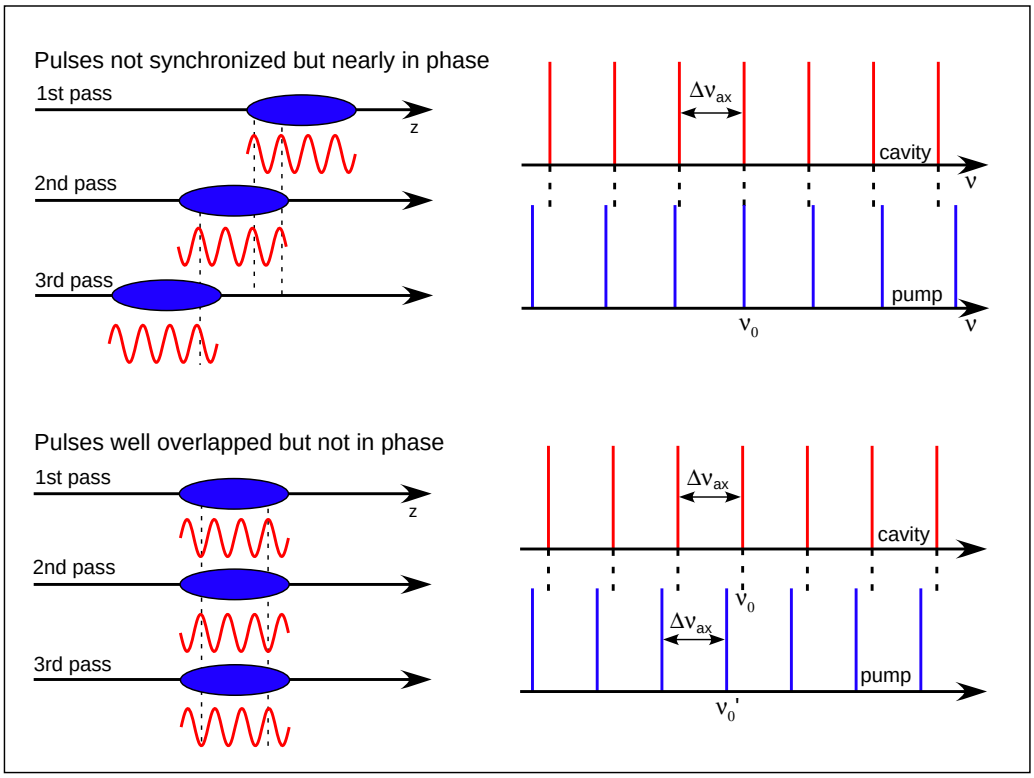

Figure 2.1: Phase-locked laser pulses injected into a resonator must stack coherently after many passes to achieve an intensity enhancement. In the frequency domain this is equivalent to ensuring that the cavity mode spectrum perfectly overlaps the frequency comb of the pump laser.

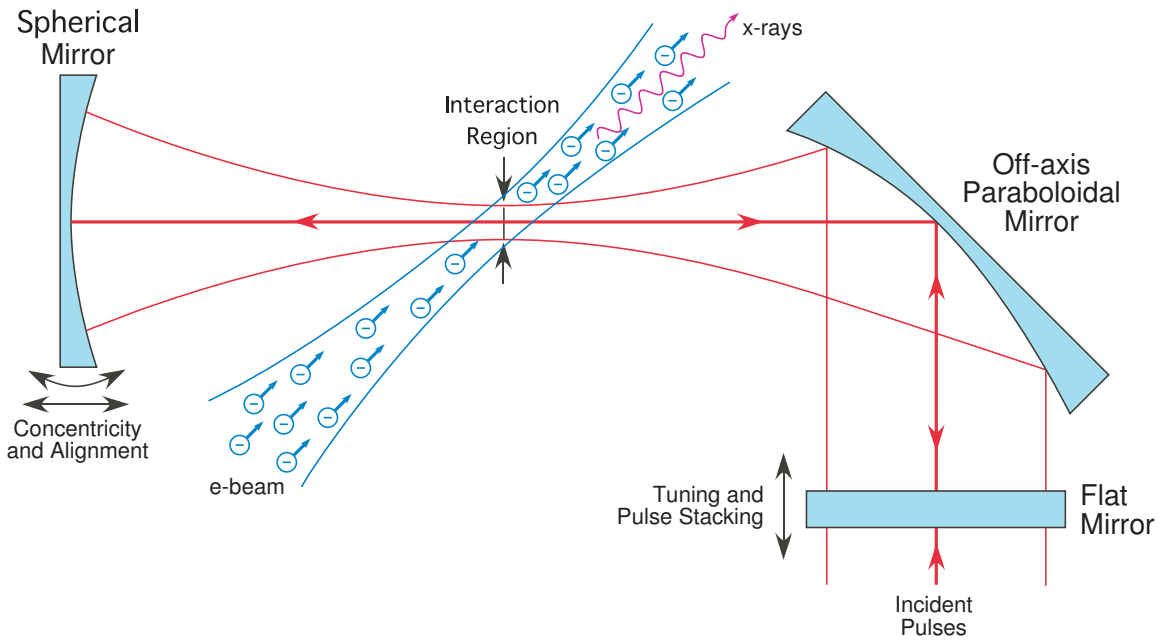

Figure 2.2: The three-mirror optical storage cavity provides simultaneous and independent means of adjusting the cavity length and concentricity. The cavity can be precisely tuned and stabilized while retaining the ability to adjust and maintain the size of the focus at the interaction point.

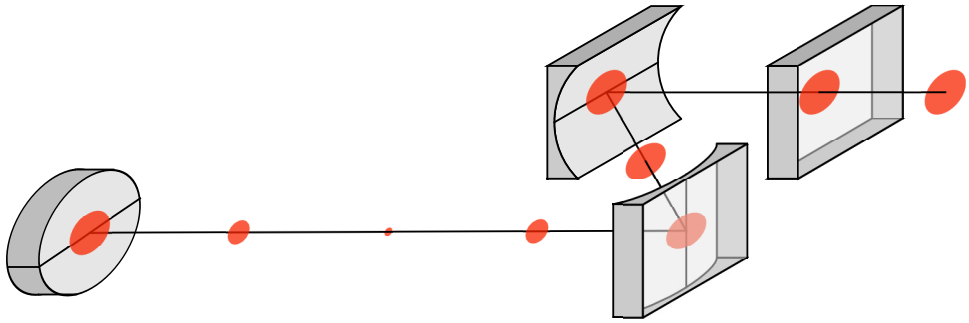

Figure 2.3: The four-mirror optical storage utilizes a pair of cylindrical mirrors as a focussing element. This allows one of the cavity end mirrors to be planar rather than spherical.

focus can be optimized through steering and translation of the spherical mirror relative to the paraboloid while compensating for changes in cavity tuning with the flat mirror.

2.2.2 Four-Mirror Storage Cavity

While a three-mirror design is preferred in order to limit the mirror losses in the storage cavity, an off-axis paraboloidal mirror with sufficient surface quality for intra-cavity use turned out to be too expensive to employ in the cavity prototype. An alternative (lower cost) solution shown in Figure 2.3, which we employed in the prototype, replaced the paraboloidal mirror with a pair of cylindrical mirrors. In addition to the significantly lower cost of precision cylindrical optics over a precision asphere, the four-mirror system offers other advantages over the three-mirror cavity. At the expense of a 50 % increase in cavity losses, due to the extra mirror, we gain several additional degrees of freedom in alignment as well as decoupling of the focusing into two orthogonal transverse components. Although the three-mirror cavity is preferred for a production storage cavity, the four-mirror cavity allows for lower risk experimentation (and a less costly commitment) in the development phase of the project.

The storage cavity designs discussed in this chapter are intended to be pumped by the MkV free electron laser at the University of Hawai‘i. The length of the storage cavity must be matched such that the round trip circulation time is an integer multiple of the laser micro-pulse repetition rate. This chapter analyzes a storage cavity designed to hold nine optical pulses (i.e. the tenth pulse entering the cavity will overlap with the first pulse). For a repetition rate of 2856 MHz this yields an $L = c_0/(2 \cdot (2856\,\mathrm{MHz}/9)) = 472.3\,\mathrm{mm}$ cavity length. This length was chosen for compatibility with the electron beam-line vacuum

chambers (see Appendix B) and to achieve a tight focus at the interaction point while keeping the beam large enough at the mirrors to avoid damage.

2.3 Low Power Storage Cavity Test-Bench

Many of the key development challenges for the three- and four-mirror storage cavities can be addressed using a low-cost cavity designed for use with a low power, visible HeNe laser. The test cavity allows us to develop the cavity alignment procedures and diagnostics which will be required for the operation of the high-power, high finesse, infrared cavity. It will also be convenient to have a visible light analogue cavity available to diagnose problems which occur during the commissioning of the infrared cavity where all alignment with a 3 µm wavelength beam must be done essentially 'blind'.

In the case of either the three-mirror or four-mirror storage cavities, the misalignment of the oblique incidence collimating optics results in complex aberrations which must be carefully compensated or eliminated. Only a precisely aligned cavity will maximize the power coupled to the TEM_{00} mode resulting in the extremely tight cavity waist required for efficient inverse Compton x-ray production.

This section describes the use of the four-mirror test cavity to explore several issues essential to the development of a high-power IR cavity:

- Achieving a diffraction limited focus using anamorphic (i.e. non-spherically focusing, non-orthogonal) optics by carefully balancing astigmatism and other optical aberrations.
- Precisely setting the synchronous length of the cavity to match the repetition rate of pulses from the FEL pump laser that will be used with the IR cavity.
- Locking the cavity to a single longitudinal mode using Pound-Drever-Hall stabilization.
- Adjusting the concentricity of the cavity to obtain the required focal spot at the interaction point.

2.3.1 Design

For the prototype system we have chosen a spherical cavity mirror with a radius of 200 mm and two cylindrical mirrors with radius 380 mm. The axis of curvature of the two mirrors are orthogonal with one mirror focusing horizontally and one vertically.

A spherical mirror aligned at oblique incidence is anamorphic, resulting in an astigmatic beam since the mirror has a different effective focal length for its tangential and sagittal transverse extents[22, pg.585].

$$f_t = \frac{R}{2}\cos\theta \tag{2.1}$$

$$f_s = \frac{R}{2}\frac{1}{\cos\theta} \tag{2.2}$$

A collimated beam incident on such a spherical mirror with an angle of incidence (at the beam center) of θ will focus at the distance f_t in the plane of the beam (tangential) and a distance f_s in the perpendicular direction (sagittal). One way to overcome this astigmatism is to use an optic with different radii of curvature in the tangential and sagittal planes such as an ellipsoidal or paraboloidal mirror. For the three-mirror storage cavity, an off-axis paraboloid satisfies this purpose. The alternative approach explored in this section is the use of a pair of cylindrical mirrors to compensate for the astigmatism in the spherical reflector.

Using cylindrical mirrors it is possible to decouple the tangential and sagittal focusing properties of the sphere into two independent optics. For the sake of symmetry the nominal angle of incidence and curvature are the same for both mirrors with the mirror spacing d chosen such that focii of the tangential and sagittally focusing mirrors converge to a single plane on the optical axis.

$$f_2 = \frac{R}{2}\cos\theta \qquad \text{(tangential)} \tag{2.3}$$

$$f_3 = f_2 + d = \frac{R}{2}\frac{1}{\cos\theta} \qquad \text{(sagittal)} \tag{2.4}$$

This gives the relation between the mirror separation d and the angle of incidence:

$$\frac{2d}{R} = \frac{1}{\cos\theta} - \cos\theta \tag{2.5}$$

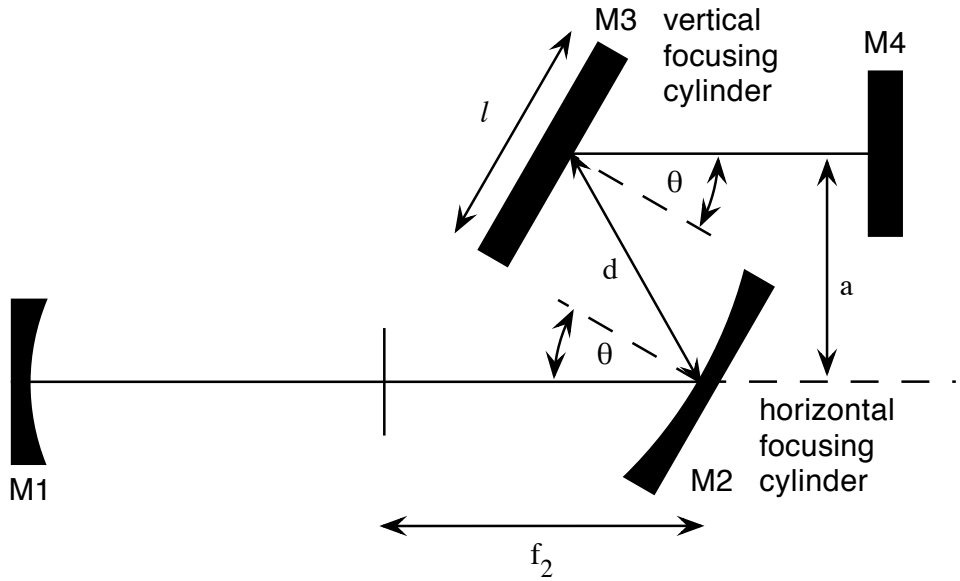

Figure 2.4: 4-mirror cavity geometry

At 45° incidence, for example, $f_2 = d = f_3/2 = \sqrt{2}R/4$. An additional design constraint, however, is that for a low angle of incidence the two mirrors will obstruct each other. With the angles of incidence equal for both mirrors, the input and output beams are parallel with a separation $a = d \sin 2\theta$ (see Figure 2.4). The apertures of the two mirrors do not overlap if the restriction $a > l \cos\theta$ is imposed, where l is the mirror width in the plane of the beam (assuming square mirrors). The design is optimized with software to minimize the mirror separation d while maintaining the full beam aperture and a value of f_3 less than half the length of a 9-pulse storage cavity.

The design solution chosen for the four-mirror cavity has $R = 380\,\text{mm}$, $\theta = 30°$ and $l = 38.2\,\text{mm}$ with the following parameters:

$$\begin{aligned} f_3 &= 219.4\,\text{mm} \\ f_2 &= 164.5\,\text{mm} \\ d &= 54.8\,\text{mm} \\ a &= 47.5\,\text{mm} > l\cos\theta\,(= 33.1\,\text{mm}) \end{aligned} \tag{2.6}$$

The focusing assembly in Figure 2.5 is constructed from custom square mirror holders attached to stock Thorlabs KM100 kinematic mirror mounts. The two mirror

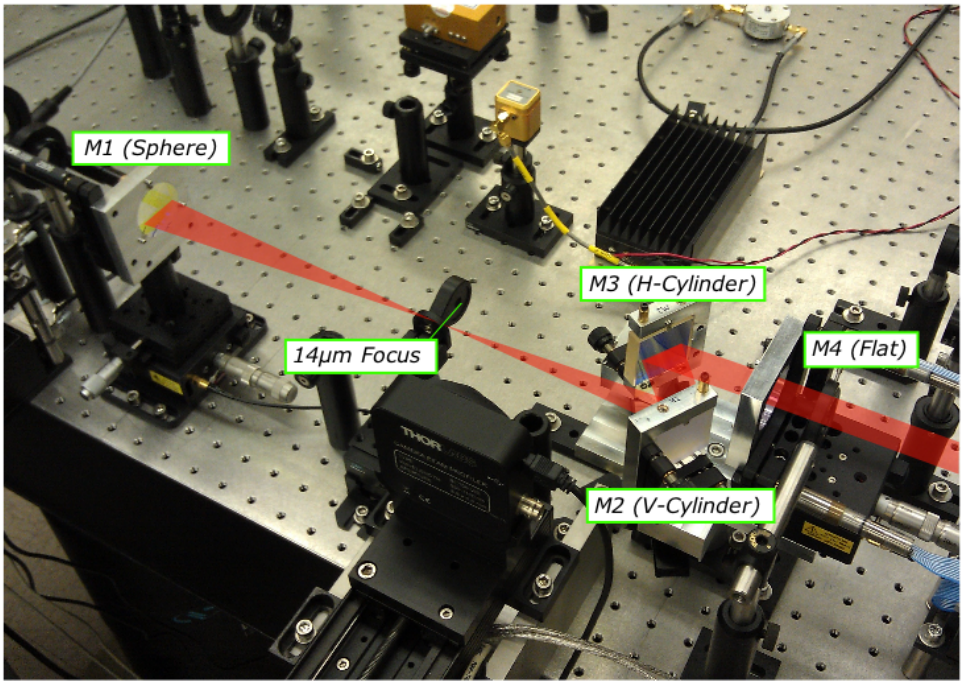

Figure 2.5: Fully assembled four-mirror test cavity

mounts are maintained at a nominal 30° angle of incidence by mounting the mirrors on a rail oriented at 60° to the cavity axis (and normal to the mirrors' surface centers). Translation of the mirrors along the rail maintains the angle of incidence and may be used to vary d independently from θ. If the focal lengths are found to differ from the specifications above, due to manufacturing error in the mirror curvature or the mounting hardware, the angle of incidence can easily be tuned according to (2.3) and (2.4) to compensate.

During initial testing it was discovered that the astigmatism present in the focus was particularly sensitive to rotation of the mirrors about their substrate normals. To correct for any error in fabrication of the mirrors or mounts, the mirror holder shown in Figure 2.6 was designed with the ability to rotate a mirror about its center and normal to the surface.

2.3.2 Optimization of the Cavity Focusing Assembly

The first step in the alignment of the storage cavity is the configuration of the two cylindrical mirrors (M2 and M3) to remove all astigmatism from a properly aligned input beam. The full system layout is shown in Figure 2.7. For this stage of alignment

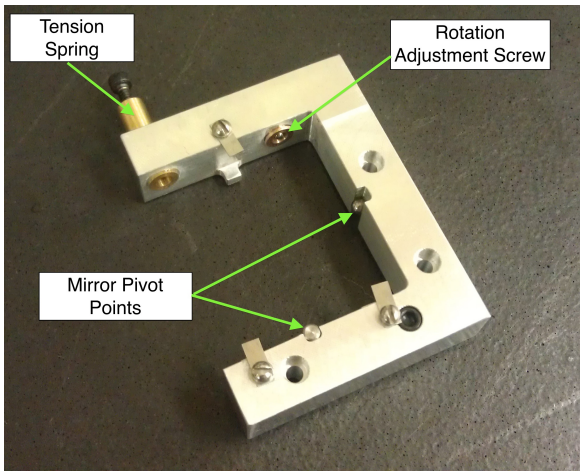

Figure 2.6: Specially designed mirror holders allow a square mirror to rotate about its center on an axis normal to its surface. The mirror motion is constrained to a single rotation axis by the ball and pin contact points shown. Longitudinal motion is constrained by three tabs machined into the mount body with the mirror retained with spring clips. A tensioning spring applies a counter-clockwise torque to the mirror while the rotation angle is set by an adjustment screw serving as a rotation stop.

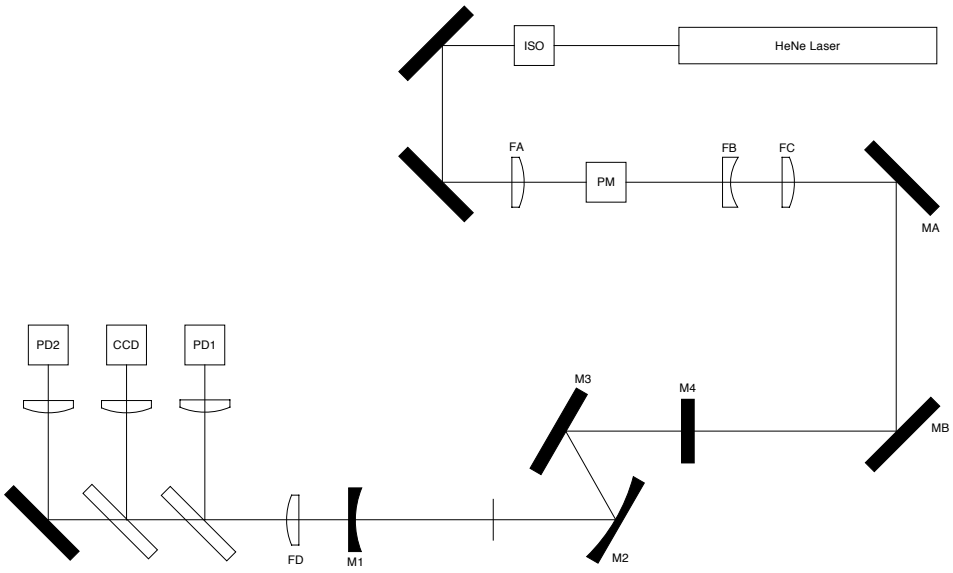

Figure 2.7: The optical storage cavity test-bench apparatus includes the optics necessary to focus, align and modulate the HeNe laser beam used for cavity experiments. Beamsplitters allow several diagnostics to simultaneously analyze light transmitted through the cavity.

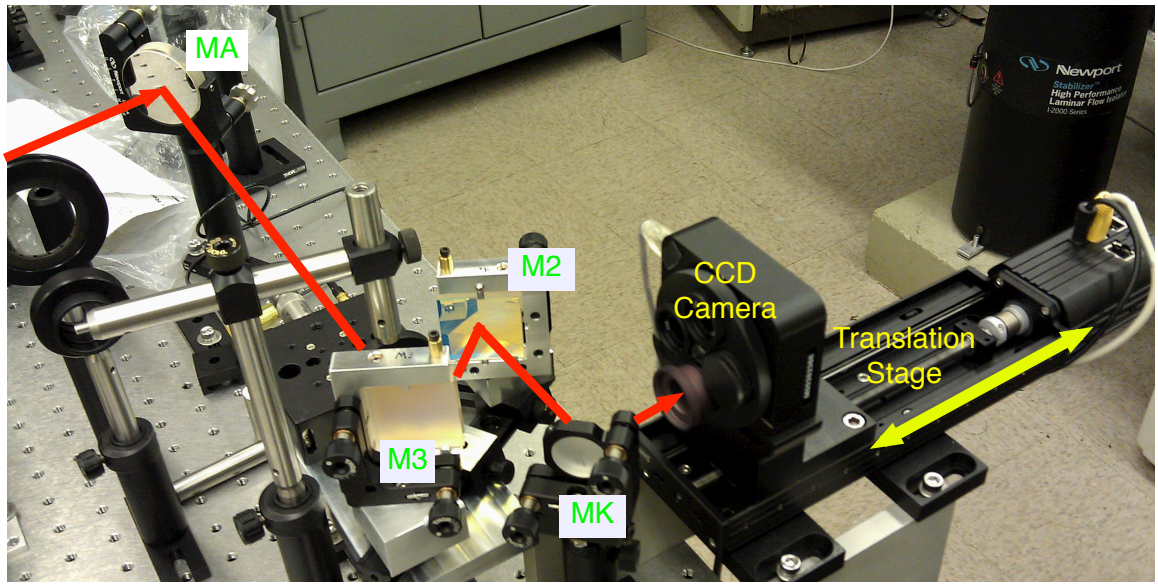

Figure 2.8: A Thorlabs CCD beam profiler and M^2 measurement system allows for analysis of the focal characteristics of cylindrical focusing mirrors M2 and M3.

the cavity input coupling mirror (M4) is removed to eliminate etalon interference fringes resulting from multiple reflections M4 and the CCD camera. The cavity axis (M1-IP-M3) is nominally aligned with a row of holes on the optical bench at 6.5" height. The input beamline (MB-M4-M3) is then carefully established parallel to the cavity axis with an offset of $a = 47.5\,\mathrm{mm}$. Cylindrical mirror M3 is installed on its rail in the sagittal focusing orientation; the mirror is positioned and aligned such that the beam is centered over the 60° mounting rail. By design the beam is now centered in the mirror and at 30° incidence. Next, a flat mirror is installed at the M2 position and the beam is directed into a CCD beam profiler via a turning flat (see Figure 2.8). With the camera positioned 219.4 mm from M3 the input beam focusses to a horizontal line. The orientation of this line focus must be parallel to the table, so M3 is roll-rotated about its surface by θ_{M3} to compensate. It is critical to ensure the the beam height is 6.5" at all points on the beamline to avoid an unintentional rotation of the image. After each adjustment of the mirror rotation θ_{M3}, the previous alignment of M3 must be restored.

Cylindrical mirror M2 is next installed in place of the flat mirror in its tangential focusing orientation, and mirror M3 is replaced with the flat mirror. With the alignment restored, M2 is rotated to orient the focal line perpendicular to the table. With the coarse

mirror rotation complete the installation procedure for M3 and M2 is repeated. The beam should now be nearly stigmatic at the focus.

With a carefully aligned system and only a slight astigmatism present (due to an error in the mirror spacing d) we were surprised to observe that the two focii take the form of ellipses rotated at nearly $\phi = \pm 45°$ relative to the beam plane. Further experimentation has showed that the spacing between the focii (astigmatism) is not affected by changes in the spacing d but rather in the roll of mirrors M2 and M3 (θ_{M2} and θ_{M3}). It is also interesting to note that the rotation angle of the ellipse is related to d and not to θ (see Figure 2.9). To aid in understanding the phenomena, two experiments were performed to find the optimal φ and d needed to achieve a stigmatic diffraction-limited focus.

First, the dependence of the ellipse rotation angles φ_a and φ_b at the astigmatic focii, and their positions z_a and z_b on the θ_{M2} roll angle of mirror M2 were measured. Rotation angles were determined by measuring the mirror tilt relative to the mount using digital calipers. This experiment was repeated for three different mirror spacings, d. A graph of the $\alpha(= z_b - z_a)$ vs θ_{M2} appears hyperbolic so a quadratic is fit to α^2 vs θ_{M2} as shown in Figure 2.10. The optimal mirror rotation angle is the point where $\alpha \to 0$. These three data sets yield an optimal $\theta_{\mathrm{M2}} = (1.037 \pm 0.003)°$ clockwise looking at the mirror surface. This definitively shows that this is not a simple astigmatism since there is no dependence on the change in mirror separation. It is also noted that while $\varphi_{a,b}$ depends on d it does not depend strongly on θ_{M2}.

Second, the dependence of focal spot rotation on mirror separation is measured. The orientations of the focal ellipses, φ_a and φ_b, are measured at the focii for eight different values of d. A line is fit to φ_b vs d as shown in Figure 2.11. Since the ellipse angles are distributed about $\varphi = 45°$ in all experiments performed, it was assumed that the ellipse should be oriented at 45° when the astigmatism is completely removed. Therefore, the optimal mirror spacing is the point at which $\varphi_b = 45°$. The fit parameters give an optimal mirror M2 position of 18.86 mm. Note that the position in these experiments is not the actual mirror separation but the position of mirror M2 relative to a convenient reference point on the apparatus (this result likely corresponds to the nominal mirror separation $d = 54.8$ mm). These data also show a focal separation of $\alpha = 10.4\,\mathrm{mm} \pm 0.2\,\mathrm{mm}$ over 8 mm of mirror travel, again confirming the independence of α on d.

These data indicate that the beam rotation aberration observed is not a simple astigmatism due to mirror misalignment and that a 45° beam rotation is intrinsic to this

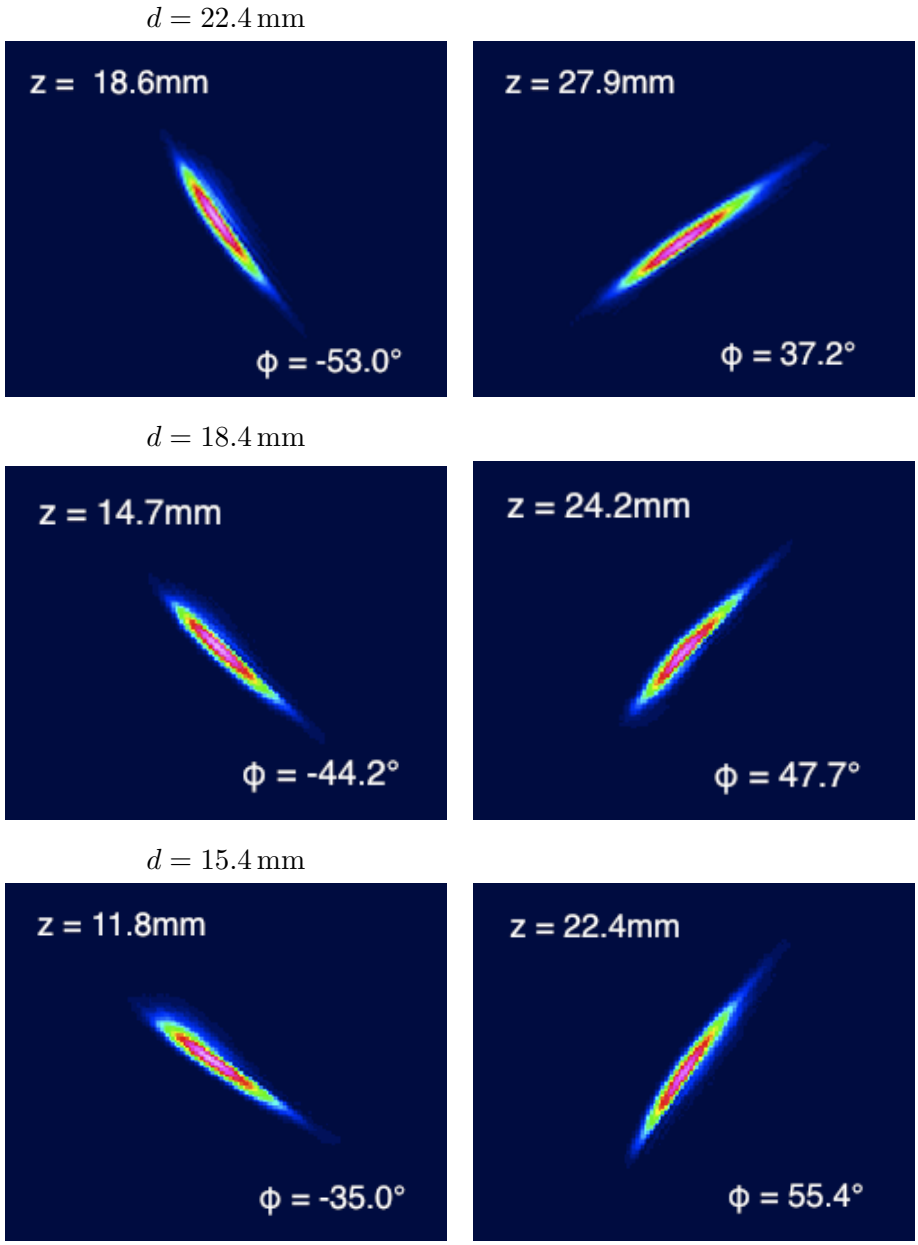

Figure 2.9: The two elliptical focal spots are shown for various mirror spacings with a fixed mirror rotation of $\theta_{\mathrm{M2}} = -0.92°$. The ellipse rotation is $\pm 45°$ for the optimal astigmatism compensating mirror spacing.

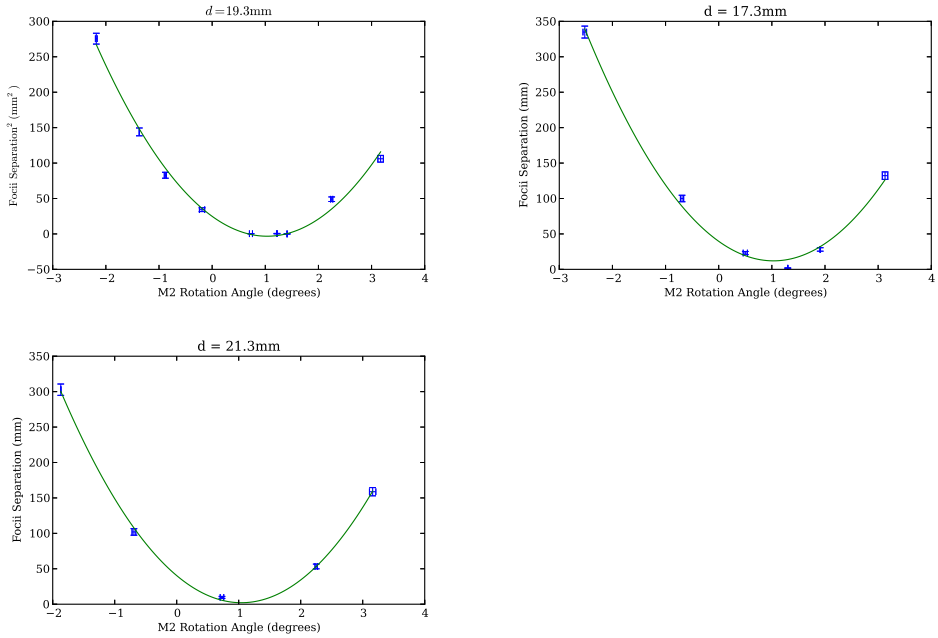

Figure 2.10: The separation between the two elliptical focal spots shows a hyperbolic dependance on the mirror rotation angle θ_{M2}, independent of the mirror spacing d. The minimum separation indicates the mirror rotation required to achieve the smallest possible focal spot.

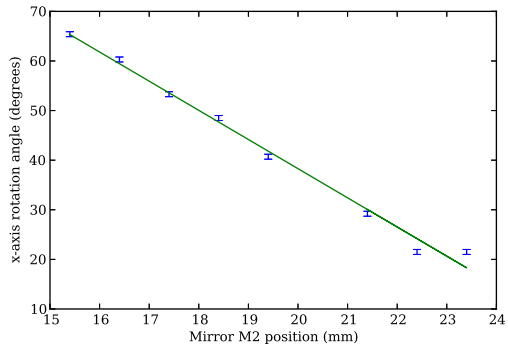

Figure 2.11: The focal ellipse rotation angle depends on mirror spacing d for a fixed mirror rotation angle $\theta_{\mathrm{M2}} = -0.92°$. The position 18.86 mm corresponds to the optimal mirror spacing from the design of $d_0 = 54.8$ mm. At this spacing the ellipse rotation angle is 45°.

focusing geometry. The physical explanation of this phenomenon is not completely understood. However, it has been well characterized empirically for the purpose of precision alignment of the system.

In the case where the M2 and M3 curvatures are perfectly orthogonal, and the two mirrors are exactly aligned to the tangential and sagittal planes respectively, it is expected that the focusing properties in these coordinates are fully separable. Such an analysis yields simple-astigmatic, elliptical focii aligned to the horizontal and vertical planes at each mirror's respective focal plane. This is not what was observed and clearly there is a higher order effect in play beyond paraxial beam optics. The fact that the optimized optical system gives a rotation angle of exactly $\pi/4$ is unlikely to be coincidence.

An early Zemax ray-tracing simulation of this cavity geometry with nominally aligned beams and optics did not show the observed image rotation nor any noticeable beam aberrations. Tilting both cylindrical mirrors downward by 1.5° did result in a beam rotation similar to that observed with the actual cavity[23]. However, 1.5° on both mirrors is a significant perturbation and we do not believe that an error of this magnitude exists in the fully aligned cavity apparatus. Every effort was made to optimize the cylindrical cavity mirror alignment to minimize astigmatism while keeping the beam in-plane. A custom ray-tracing code was later developed specifically to study this problem and did reproduce the observed beam aberrations. These simulation results will be discussed in Section 2.3.3.

In addition to the higher order effects of the cavity focusing mirrors, the system has also proven to be quite sensitive to other sources of distortion in the input beam. Initially a telescope consisting of two cylindrical lenses was installed on the input beamline to shape the beam into an ellipse matching the cavity geometry's divergence asymmetry of 0.75. Despite our best efforts to align this telescope to match the cavity, its presence increased the astigmatism within the cavity by an order of magnitude. The telescope was removed from the system resulting in an improved cavity focus at the expense of a small reduction in mode coupling efficiency. The input beamline also originally contained an additional 20 MHz phase modulator for use with the cavity stabilization system discussed in Appendix A. This modulator showed visible amounts of anamorphic focusing and was found to increase the beam astigmatism; it has been removed for this phase of the project. For similar reasons a Faraday isolator was also replaced with a different model to eliminate unwanted astigmatism. This original isolator added significant astigmatism to the beam

due to anamorphic focussing in one of its polarizers. When replaced by a Faraday isolator with polarizing beamsplitter cubes no aberration is seen.

To rule out the possibility of a polarization dependance, the input polarization was rotated from 0° to 90°. No perceptible difference in the shape or rotation of the focii effectively ruled out any effects due to the cavity mirror coatings. The quality of the final optimized input beam is quite high ($M^2 = 1.04$) and its effect on the cavity mode is likely negligible. However, great care must be taken to avoid disturbing the alignment of the coupling optics and to monitor the system for drift over time which may reduce beam quality. Careful attention must also be paid to thermal effects in the active components of the system. HeNe lasers can experience large beam deflections during their warm up period. The 2.856 GHz phase modulator also appears to exhibit RF power dependent focussing. Considering that 2 W of RF power is delivered to this resonant device, a temperature gradient can exist within the crystal since power will be deposited in the form of the resonant cavity standing wave field. This temperature gradient will cause anisotropy in the refractive index of the crystal and thus focus the beam. The modulator is allowed to reach thermal equilibrium before the cavity is optimized but additional higher order aberrations could also be present.

The overall focal properties of the system are analyzed using the Thorlabs BC106 CCD camera M^2 measurement system. Figure 2.8 shows the analysis apparatus consisting of a CCD camera mounted on a translation stage and positioned with the cavity waist midway through the range of motion. Under computer control, images of the beam are taken at many points within a range $\pm 2z_R$ about the beam waist. The beam propagation ratio M^2 and other gaussian beam parameters are found by fitting these data in accordance with the industry standard technique defined in ISO 11146-1. The beam propagation ratio M^2 is defined as the "the ratio of the beam parameter product of the beam of interest to the beam parameter product of a diffraction-limited, perfect Gaussian beam (TEM_{00}) of the same wavelength λ."[24]. M^2 is thus a measure of the transverse phase space occupied by the laser beam.

Figure 2.12 shows a sample of the data captured by the M^2 measurement system and the resulting beam parameters tabulated from five such scans. The Rayleigh range of the beam, z_R, is defined as the distance from the waist over which the beam size increases by a factor of $\sqrt{2}$ and is thus invariant to differences in M^2 beam quality factor. The beam analysis software performs a hyperbolic fit to the beam diameters measured during a scan

resulting in z_R and M^2 for the beam along two orthogonal principal axes. Note that the beam diameters reported by the software are observed diameters and are larger than those of a pure TEM_{00} beam by a factor of M for the same z_R. The values of $w_{0x/y}$ are are the TEM_{00} waist radii and are calculated, for a beam with wavelength λ, from the relation

$$w_0 = \sqrt{\frac{\lambda z_R}{\pi}} \tag{2.7}$$

These radii represent the size of the beam that will couple to the TEM_{00} mode of a nominally aligned resonator. The larger observed beam diameters have an effectively increased diffraction limit due to the presence of higher order transverse modes.

The TEM_{00} mean waist size, inferred from the measured z_R as $w_0 = 17.3\,\mu\mathrm{m}$, differs from the cavity design specification of $w_0 = 14.2\,\mu\mathrm{m}$. This difference is likely due to a smaller than intended input beam and could be corrected by further optimization of the collimating telescope. Due to the M^2 of 1.5, significant energy is lost into higher order transverse cavity modes; it is, however, possible to construct a four-mirror optical storage cavity with a sufficiently small waist size for use in x-ray scattering experiments. Optimization of the cavity mechanical design will further reduce the limiting aberrations, thus improving M^2. For example, the angular steering resolution of the mirror mounts can be increased.

The coupling efficiency of a beam with a given M^2 value can be computed through the overlap integral of two gaussian beams with differing radii. The resulting intensity coupling coefficient is[4]

$$\eta = \frac{4}{\left(\frac{w_b}{w_0} + \frac{w_0}{w_b}\right)^2} \tag{2.8}$$

The beam waist w_b is larger than its corresponding TEM_{00} waist by a factor of M resulting in

$$\eta = \frac{4M^2}{(1+M^2)^2} \tag{2.9}$$

Thus, the beam with $M^2 = 1.5$ couples to a TEM_{00} cavity mode with 96 % efficiency. The remaining 4 % of the power is distributed amongst the higher order transverse modes and is reflected from the cavity.

The beam parameters in Figure 2.12 also indicate a divergence asymmetry $z_{\mathrm{R}x}/z_{\mathrm{R}y}$ of 71 %. This reasonably agrees with the asymmetry inherent to this cavity geometry since

the ratio of the focal lengths of M2 and M3 is 0.75. Since the focusing mirrors M2 and M3 are located at different distances from the cavity waist, a circularly symmetric beam diverging from the waist will be collimated by this pair of mirrors. However, because of the unequal mirror distances, different beam sizes will result in the x and y axes. To achieve a circular spot at the cavity waist an elliptical beam with 75 % ellipticity must be injected into the cavity. In this case a circular beam is injected and the resulting cavity mode has an elliptical profile. The measured cavity waist, however, is circular since it is diffraction limited in both axes for the measured M^2.

To provide a useful focus for x-ray scattering any astigmatism in the focus must be minimized. As long as the astigmatism is reduced to less than the Rayleigh range the waists in the two principal axes essentially overlap. The best possible alignment of the cylindrical focusing optics resulted in an astigmatism of 0.5 mm and meets this criteria for $z_R = 1\,\mathrm{mm}$ for this design. This beam is as tightly focussed as possible throughout the entire interaction length of interest for x-ray production.

The beam rotation effect was an entirely unexpected, but important, discovery with implications for the three-mirror storage cavity. It is entirely possible that an infrared cavity using an off-axis paraboloid or other focusing system will exhibit these types of aberrations if not perfectly aligned. Clearly, small irregularities in the injected beam, and minor alignment perturbations, can result in significant aberrations that may limit our ability to achieve the desired focal spot within the cavity. This will make alignment in the infrared even more challenging due to the increased complexity of aligning and profiling an invisible pulsed beam. If the principal axes of the elliptical focii were naively assumed to be oriented horizontally and vertically in the lab, then any measurements of the beam size and quality using these incorrect principal axes will be overestimated and conceal the actual astigmatism present in the beam. In an infrared cavity it is likely that a scanning slit profiler will be used rather than a CCD camera so it is important to know a priori the principal axes of the beam within the cavity. Additional simulations can also assist in the development of alignment procedures for the infrared cavity.

With the cylindrical mirror assembly alignment complete, the input coupling mirror M4 is then installed. Mirror M4 is a flat wedged optic with a high reflectance coating on one side and an anti-reflective coating on the other side. The input beam used in the alignment of the focusing mirrors must now be realigned to account for the wedge deflection. The position of mirror M3 on its mounting rail is marked and the mirror is removed. With

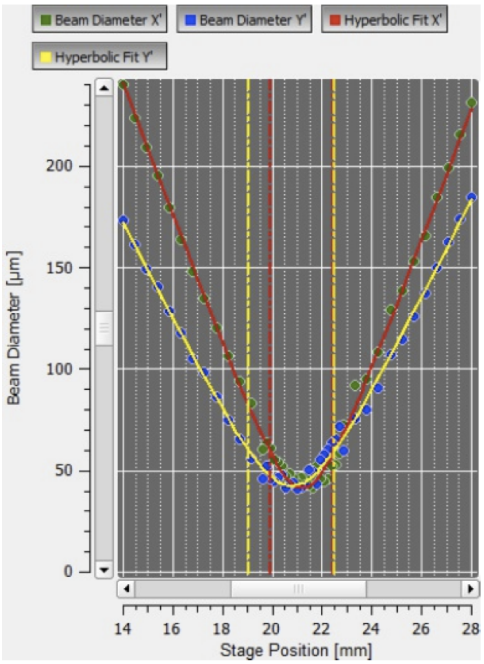

M^2 Scan Results Summary		
M_x^2	1.69 ± 0.01	
M_y^2	1.30 ± 0.01	
d_{0x}	41.5 ± 0.3	µm
d_{0y}	42.8 ± 0.3	µm
z_{Rx}	1.260 ± 0.007	mm
z_{Ry}	1.742 ± 0.013	mm
α	0.5 ± 0.1	mm
w_{0x}	16.0 ± 0.2	µm
w_{0y}	18.8 ± 0.2	µm

Figure 2.12: The beam profiler collects beam size measurements at several positions on either side of the focus. A hyperbolic fit reduces the data to the Rayleigh range z_R and beam propagation factor M^2. The table shows the averaged results of five scans of the beam focus. Note that the beam diameters shown are for the observed beam spots, not the TEM_{00} mode, and are related to the TEM_{00} waist radius through $d = 2Mw_0$.

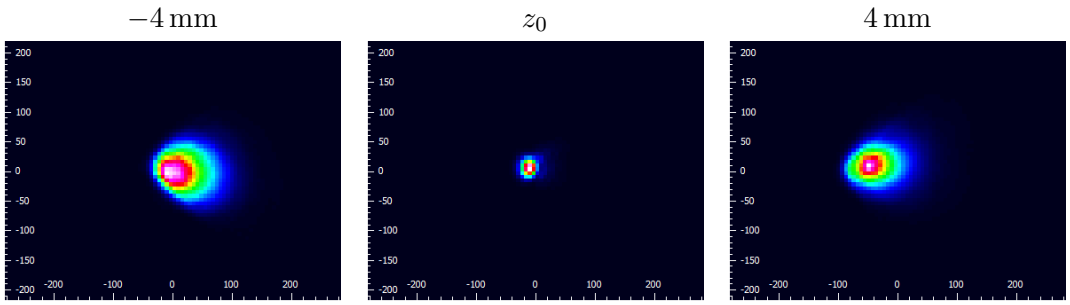

Figure 2.13: The optimized diffraction limited cavity focus shown at the waist ($z = 0$) and at $z = \pm 4\,\mathrm{mm}$

M4 installed the transmitted beam is aligned using the input alignment mirrors MA and MB to the same offset cavity beam line marked earlier, but this time transmitted through M4. M4 is then steered so that the reflected beam is precisely aligned back to the laser, indicating that the reflective surface is at normal incidence to the beam within the cavity. With M3 reinstalled the focal spot is then re-examined for errors using the beam profiler. To avoid etalon interference effects between the CCD and mirror M4, the CCD kicker mirror is replaced with a pellicle beam splitter to provide additional loss. Input end optics for the cavity now form a fully aligned unit. Careful centering of the input beam into M4 at normal incidence should repeatably reproduce the desired focal spot.

2.3.3 Cylindrical Focusing Simulation

A ray tracing code was developed to better understand the focusing properties of the cylindrical mirror pair. Appendix C contains the vector analysis used to trace the trajectory of arbitrary rays incident on cylindrical and paraboloidal surfaces. It was initially assumed that the pair of cylindrical mirrors used in the four-mirror cavity design could compensate for the astigmatism associated with oblique incidence on a spherical mirror. Given that the curvatures of both mirrors are orthogonal it seemed reasonable to treat the two focusing axes independently. Applying paraxial beam propagation theory, such a system appears to produce a so-called 'simple astigmatic beam' in which all parallel rays converge to the optical axis, but not necessarily at the same longitudinal position. Tracing a bundle of parallel rays through the focusing system confirms our observation that this beam has a 'general astigmatism' with the presence of 'skew' rays that never cross the optical axis.

For properly aligned mirrors the effect only seems significant at the beam waist, where the spot has a diffuse tail. In the far field the beam appears relatively unperturbed in shape and closely resembles the input beam with the expected size asymmetry. Even with the tail, the ray bundle converges to below the diffraction limit, thus, this spot should still couple reasonably well to a circularly symmetric cavity mode. The difference will result in coupling to higher order cavity modes and an overall increase in cavity loss that is reflected in the measurements described in Section 2.3.6.

Figure 2.14 shows the irradiance pattern resulting from tracing a normally distributed bundle of rays through the pair of cylindrical mirrors. The input 'beam' consists of 5000 parallel rays, with equal phase, normally distributed about the optical axis with a radius of 2.7 mm, matching the actual beam used for the experiments described in the previous section. The focussed rays do not converge to an elliptical spot, but rather to a 'fan' pattern. This distorted beam shape is precisely the shape of beam observed with the CCD camera for optimal focusing of the beam using the cylindrical mirrors (see Figure 2.13). Despite the presence of the 'fan', the 4σ (second moment) diameter of the beam is 8.4 µm by 6.1 µm with a 6.5 µm horizontal offset. This beam size is well below the 28 µm diffraction limit for the given gaussian beam using these optics and appears to have nearly spherical wavefronts. Therefore, this distorted focus should still couple very efficiently to the cavity TEM_{00} mode despite the presence of aberrations.

The simulation also allows us to explore the effects of rotating the mirrors. For comparison with the physical cavity experiments, mirror M3 is rotated about its center, normal to the surface. For $\theta_{\mathrm{M3}} = 1°$, Figure 2.15 shows that the focus becomes astigmatic exhibiting the same $\pm 45°$ focal ellipses that we observed with the real cavity for a similar mirror perturbation (see Figure 2.9). An animated version of the beam transformation shown in Figure 2.15 was generated by simulating the ray distribution at many more points in the focal region and behavior that is consistent with observations of the physical beam focus as the CCD camera was scanned through this region.

This ray-tracing model has demonstrated that the cylindrical focusing geometry of the four-mirror storage cavity is not capable of fully eliminating the cavity astigmatism without introducing higher order distortion to the beam. Future development of the ray tracing code is necessary in order to analyze the wavefronts associated with ray distributions in Figures 2.14 and 2.15. For intense, coherent beams of light, the trajectories of discrete photons can not generally be treated as rays and interference must be accounted for. How-

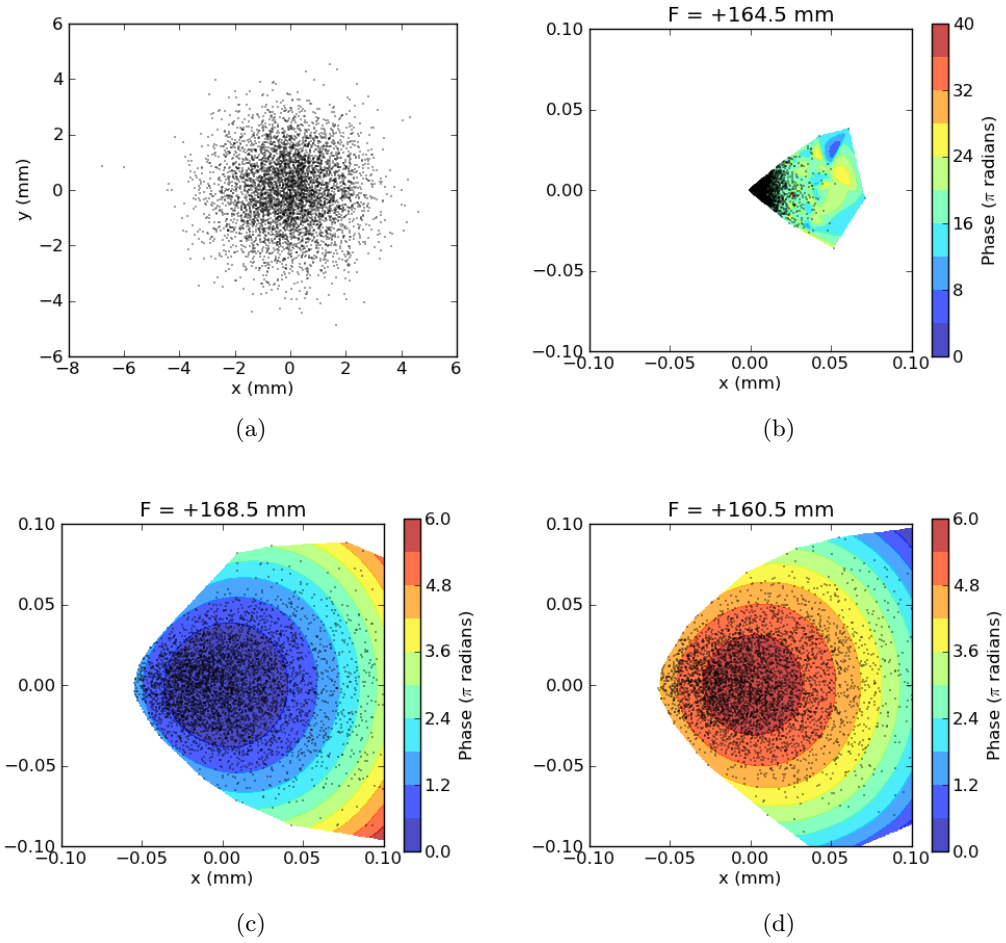

Figure 2.14: (color) A normally distributed bundle of 5000 parallel rays (a) simulates a gaussian beam. The cylindrical mirror pair focusses the bundle to definite 'fan' pattern (b). This simulated irradiance pattern at the cavity focus exactly matches the observed laser focus in the storage cavity. The pattern viewed at ± 4 mm offsets (c, d) are also in close agreement with the observed intensities shown in Figure 2.13. The colored background represents contours of constant phase.

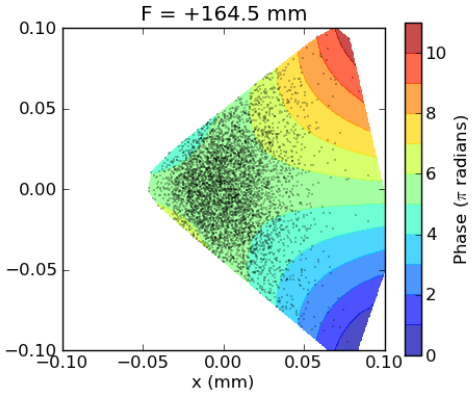

(a)

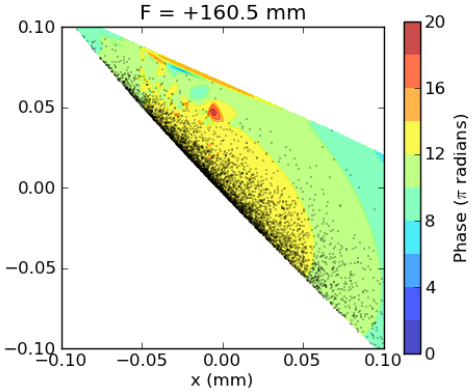

(b)

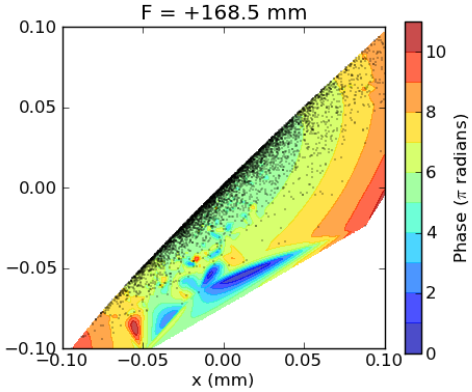

(c)

Figure 2.15: (color) The ray bundle from Figure 2.14a is now focused by the cylindrical mirror pair with mirror M3 rotated by 1° about the x-axis (normal to the mirror surface at its center). The focus in (a) is considerably larger than the focus in Figure 2.14b and for planes ±4 mm from the focus the fan is transformed into a narrow rotated ellipse. These simulated results agree well with the behavior of the beam due to mirror rotation as shown in Figure 2.9.

ever, the simulation results presented above are sufficient to explain the observed cavity focusing distortions. The inclusion of random angles as well as random starting positions for the Gaussian ray bundle will reproduce the diffraction characteristics of a real Gaussian beam[25]. This is the equivalent of generating a bundle of rays with a normal distribution in *phase space* not just irradiance. It should be possible to simulate the propagation of a beam of 'Gaussian rays' through the full storage cavity for a large number of passes to determine the diffractive losses and shape of the stable cavity mode.

The ray tracing code also confirms that the paraboloidal focusing mirror used in the three-mirror cavity design is truly immune to the cylindrical mirror aberrations shown in Figure 2.14. Figure 2.16 shows the ray bundle from Figure 2.14a focussed by a paraboloidal mirror with an effective focal length of 200 mm in three planes. Note that while the rays converge to a singular point with no aberration, a real gaussian beam will diffract and have a finite waist radius.

2.3.4 Cavity Alignment and Optimization

The storage cavity is completed with the installation of spherical high reflectivity mirror M1. The steering and longitudinal translation of M1 provide full control over the optimization of the cavity mode. The longitudinal position of M1 is initially chosen to be a few mm shorter than the nominal cavity length for the desired waist size. This relaxes the sensitivity of the cavity alignment to M1 steering during alignment so that the cavity length can gradually be drawn back to the near-concentric length during the alignment. Mirror M1 is aligned using motorized actuators such that the TEM_{00} mode intensity is maximized.

Visual inspection of the transmitted cavity modes also provides valuable insight into the alignment and focal properties of the cavity. Figure 2.17 shows a selection of cavity modes captured with the CCD camera. Without active cavity stabilization, drift and jitter result in mode excitations with random durations, which are difficult to image on the CCD camera. Dithering the cavity length over a full FSR at 50 Hz ensures that each mode is excited and for equal duration. The CCD camera is configured with a shutter speed fast enough to capture no more than one transverse mode at a time to avoid mixing of multiple mode images. The camera acquisition software has a software trigger mode allowing images to only be captured above a chosen intensity threshold. Since the camera shutter is free running, it is not guaranteed that a mode captured by the software was fully contained within a shutter window. Significant deviations are seen in the intensity

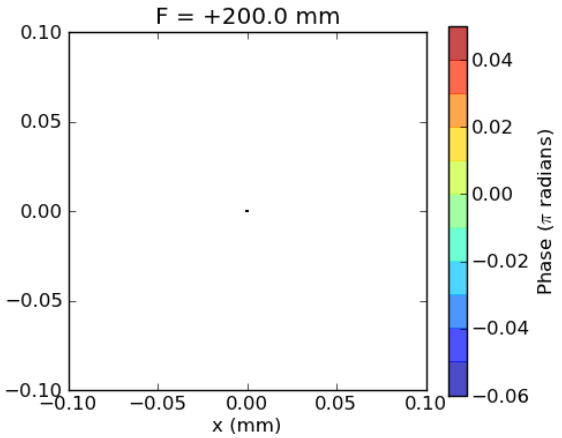

(a)

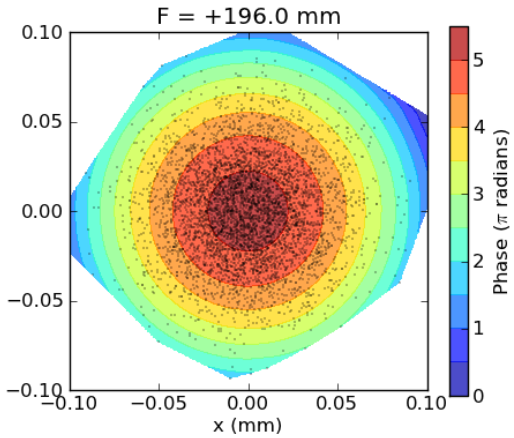

(b)

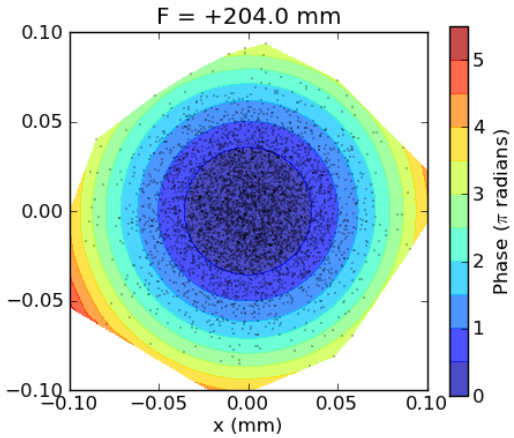

(c)

Figure 2.16: (color) Gaussian ray bundle focused by an off-axis paraboloidal mirror with a 200 mm effective focal length. Images (b) and (c) show that the beam is undistorted and symmetric about the focal plane at $F = 200$ mm with the rays converging to a singular point on the axis at the focus in image (a).

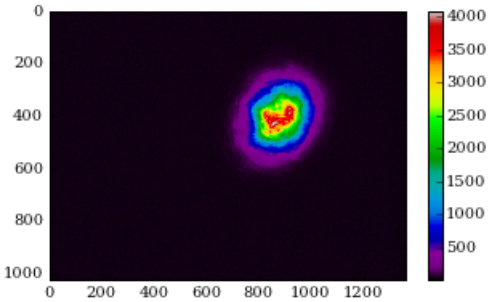

(a) TEM_{00}

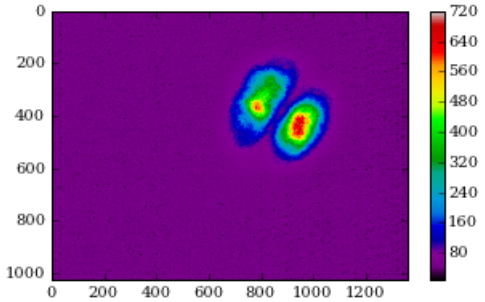

(b) TEM_{10}

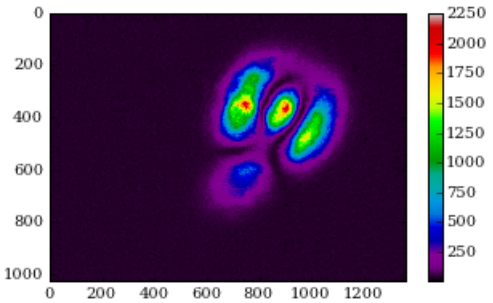

(c) TEM_{20}

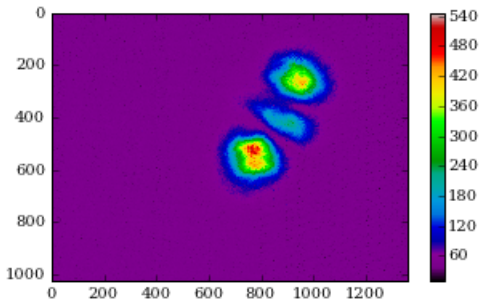

(d) TEM_{02}

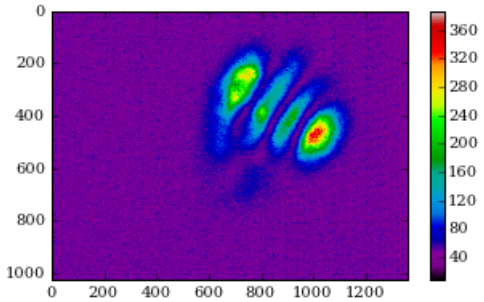

(e) TEM_{30}

Figure 2.17: (color) CCD camera images of modes transmitted by the cavity. The CCD pixel size is $6.45\,\mu m^2$, however the beam size is not significant since the Hermite-Gauss transverse modes propagate without changing shape only size. Note that the peak intensity of the TEM_{00} mode is much greater than the higher order modes.

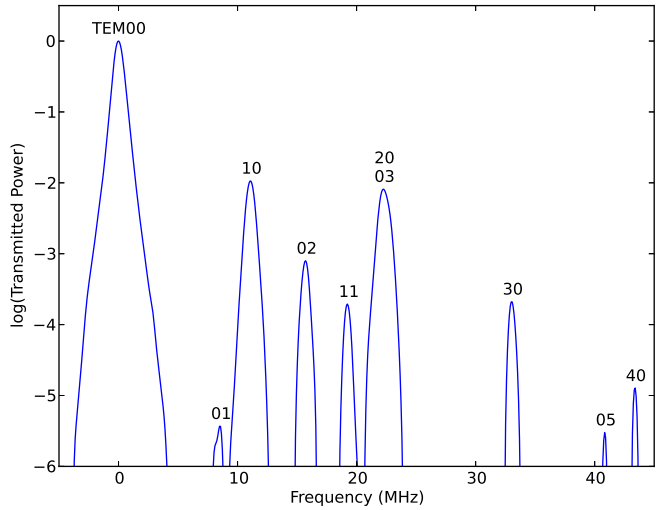

Figure 2.18: Cavity mode spectrum with tagged Hermite-Gauss transverse modes.

of otherwise identical mode images. The relative intensities of each mode image are not sufficient for identification of modes in the spectrum but together with the known order and orientation provide valuable clues. Figure 2.18 shows the mode spectrum corresponding to the mode images in Figure 2.17. The TEM_{i0} modes are dominant with equal spacing and the TEM_{0j} modes are found by looking for harmonic spacing in the remaining modes. The TEM_{11} mode is located as the sum of the 01 and 10 spacings. The degeneracy of the TEM_{20} and inferred TEM_{03} explains the distortion of the TEM_{20} mode image.

The asymmetry in the cavity modes in Figure 2.17 is due to the cavity focusing geometry. By design the cylindrical focusing mirrors impart a 75 % divergence asymmetry to the cavity mode which is reflected in the TEM_{00} ellipse. The principal axes for these modes are rotated on average 30° CW which likely indicates a small astigmatism as discussed in Section 2.3.2. This astigmatism is most likely the result of the TEM_{00} cavity not being perfectly aligned to the intended realigned axis. This further emphasizes the importance of a detailed precision alignment procedure to achieving a diffraction limited focus.

2.3.5 Infrared Cavity Diagnostics

For infrared wavelengths not served by practical CCD cameras, alternate methods must be used to 'view' the beam profile. Various photoelectric and pyroelectric focal plane

array technologies do exist in the infrared, but are extremely costly. A promising alternative is the use of a scanning slit beam profiler viewed by a single element infrared detector. Scanning a narrow slit across the beam in two orthogonal directions can map the overall intensity distribution of the beam but will in most cases miss the detailed structure of the higher order transverse modes. Additionally, if the scan axes are not oriented along the mode principal axes, a further overestimate will be made of the beam size. The solution is to use scans from many different slit orientation angles. A tomographic reconstruction can then be performed with improved resolution. Due to a rather long scan duration, such a system requires active cavity and laser stabilization to ensure that the cavity remains resonant from pulse to pulse, and that only the desired mode is detected over the scan duration.

The ideal method of capture (and most costly) is with a Shack-Hartmann type wavefront sensor. A two-dimensional pyroelectric detector array covered with a micro-lens array will be able to measure both the amplitude and phase of an incident wavefront allowing complete characterization of the cavity focal properties. Adaptive optics have proven essential to terawatt laser systems used in applications requiring a sharp focus, particularly in laser wake-field accelerators[26, 27, 20] with an emphasis on correcting distorted wavefronts from an imperfect paraboloidal reflector[28]. Mode-locked picosecond lasers are also benefiting from adaptive optics to increase mode quality and average power[29]. The photon collider community has also expressed interest in using deformable mirrors in high-power storage cavities for γ-ray production at the ILC interaction point[30, 31].

2.3.6 Cavity RF Diagnostics

This section describes a suite of storage cavity diagnostics that make use of RF modulation sidebands applied to the laser beam using an electro-optic phase modulator to measure the absolute cavity length, the cavity finesse, and the cavity concentricity. A fast photodiode is used to detect residual amplitude modulation created by transmission through the cavity. The Newfocus model #4431 MgO:$LiNbO_3$ resonant phase modulator is tuned for a center frequency of 2856 MHz and with a Q of 180 has a bandwidth of 16 MHz. The modulator is driven with 2 W (33 dBm) of microwave power resulting in first order sidebands having $\sim 25\,\%$ of the power in the fundamental mode. This corresponds to a phase modulation depth of ≈ 1.1.

The longitudinal position of the flat cavity mirror (M4) is dithered by a piezoelectric transducer driven with a 300 mV, 50 Hz sine wave. The drive amplitude was chosen such that the cavity length is dithered by just over 2λ so that two adjacent TEM_{00} modes appear in the mode spectrum on each cycle. The drive frequency is high enough to remove the effects of slow cavity drift from measurements but low enough to avoid significant phase lag in the mirror motion due to inertia of the mirror and mount. The oscilloscope used to capture data is configured with a sampling window consisting of only the center $\pm 60\,\%$ of the driving sinusoid. This effectively removes the distortion of the spectrum at the inflection points of the sine wave. The remaining non-linearity is assumed negligible, an assumption confirmed by the low variance in data collected at numerous random positions on the driving waveform.

Cavity Synchronous Length

When an optical storage cavity is pumped with a pulsed mode-locked laser it is necessary to choose a cavity length that enables successive injected pulses to stack synchronously with the circulating pulses as they enter the resonator. The length of the IR storage cavity (and also the visible test cavity) was chosen to correspond to exactly nine pulses at a repetition rate of 2.856 GHz, in order to match the pump laser. Pulses will circulate for many passes over which they must stack coherently to achieve the desired power enhancement. An IR optical storage cavity with a finesse of 2000 will have a $1/e^2$ photon lifetime of $n = \mathcal{F}/\pi = 637$ passes in the cavity. In order to keep phase walk-off to under $\pi/4$ over the lifetime, the cavity length must be held constant to within $\delta L = \lambda/n$. At $\lambda = 3\,\mu\mathrm{m}$, $\delta L = 5\,\mathrm{nm}$ over the $2\,\mu\mathrm{s}$ lifetime. While the stabilization system is responsible for maintaining the cavity length to this accuracy, it is also necessary to set the cavity length initially with an accuracy better than the target cavity concentricity of $s = 8\,\mu\mathrm{m}$. This section describes a novel RF sideband technique to accurately set and measure the absolute cavity length[32].

When a laser beam with RF phase modulation sidebands offset by 2856 MHz is injected into the nine pulse storage cavity with free spectral range of $\nu_{\mathrm{ax}} = 2856\,\mathrm{MHz}/9 = 317.3\,\mathrm{MHz}$, the sidebands will couple to every ninth longitudinal cavity mode. However, when the cavity length (and thus the FSR) varies from the synchronous length, the sidebands will not couple to a cavity mode and a residual amplitude modulation (RAM) will be observed in the light transmitted and reflected from the cavity. Figure 2.19 shows the simu-

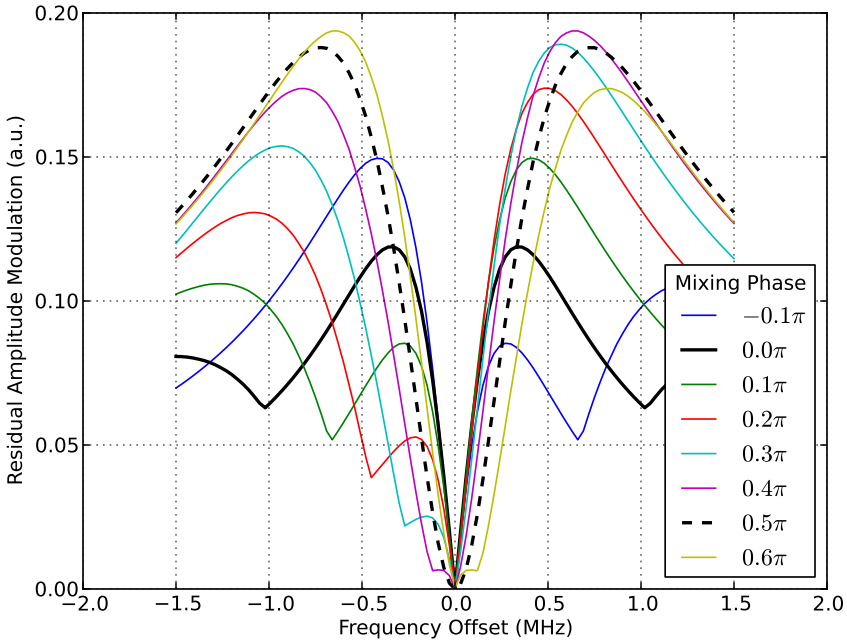

Figure 2.19: (color) Predicted RAM signal amplitude dependence on frequency offset from 2856 MHz and mixing phase (simulation data courtesy of Eric Szarmes). Note that only the 0.0π and 0.5π curves are symmetric while the 0.0π also has the sharpest minimum.

lated residual amplitude modulation as a function of FSR offset frequency from 2856 MHz. The RAM amplitude decreases nearly linearly as the cavity length is tuned towards the design FSR for nine pulses. This result can be used in two ways: coarse adjustment of the length by observation of the RAM amplitude, or a precision systematic measurement of the exact cavity length.

Laser light transmitted through the storage cavity is split by a CaF_2 wedge and focused onto the two photodetectors shown in Figure 2.8. The wedge coupled portion (10 %) of the beam is focused onto an amplified silicon photodiode and is used to measure the cavity mode transmission spectrum. The remaining 90 % of the beam is focussed onto a Hammamatsu G4176 GaAs MSM photodetector with a 30 ps rise time. This detector comes conveniently mounted in a standard TO-5 can with an SMA connector, allowing the diode to be directly mounted on connectorized, commercial RF components. The RF system shown in Figure 2.20 consists entirely of readily available and inexpensive RF components. The photodiode itself is mounted directly on a Mini-Circuits ZX85-12G 12 GHz bandwidth bias

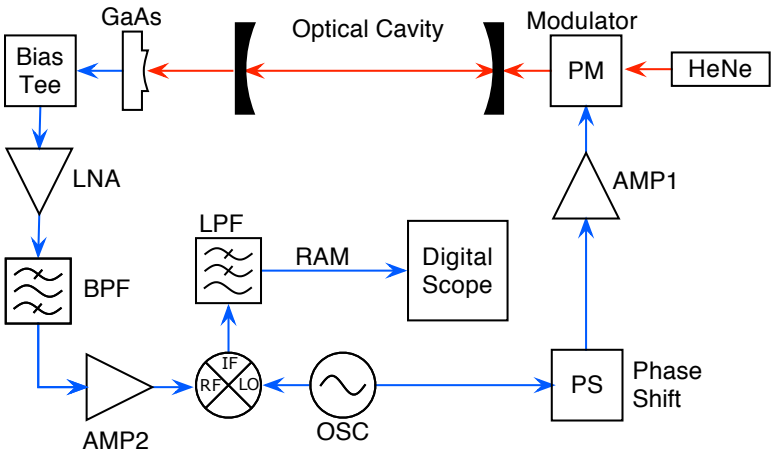

Figure 2.20: Injection of a phase-modulated HeNe laser beam into the optical cavity results in residual amplitude modulation (RAM) when the cavity free spectral range is not matched to the modulation frequency. The RAM is detected by a GaAs RF photodiode and mixed with the local oscillator phase reference. The resulting DC component of the signal is captured with a digital oscilloscope for analysis.

tee followed by a Mini-Circuits ZX60-33LN low-noise amplifier and a 2.8 GHz band-pass filter. This signal is further amplified by a Mini-Circuits ZHL-42 40 dB power amplifier and mixed with the modulation drive signal in a Mini-Circuits ZEM-4300 doubly balanced mixer. The result is a baseband (0 Hz carrier) signal proportional to the residual amplitude modulation induced in the beam by any mismatch of the cavity FSR and $1/9^{\text{th}}$ the phase modulation frequency.

Simulations show that the RAM signal has a significant dependence on the relative phase of the RF and LO signals at the mixer. Figure 2.19 shows how the shape of the RAM signal vs offset frequency depends on the mixing phase. Only in the cases of 0° and 90° phase is the curve symmetric about zero offset while only the 0° phase results in a sharp linearly sloped minimum. The phase may be adjusted over a 180° range with an Aeroflex-Weinschel 980 mechanical phase shifter. With the RF drive tuned to its nominal frequency of 2856 MHz, the position micrometer on the flat cavity tuning mirror (M4) is adjusted to minimize the RAM signal amplitude viewed on an oscilloscope. Manual adjustment of the micrometer to minimize this signal visually has a precision of about 10 µm corresponding to a frequency error of 60 kHz. Because of the asymmetry of the curves in Figure 2.19 we must carefully choose a phase at which the RAM signal is balanced. Beginning with a

0.5 MHz RF offset the phase is found that produces the lower of two maxima in the RAM amplitude. The frequency is then shifted to -0.5 MHz and the phase is adjusted to correct any imbalance. Iterating several times between ± 0.5 MHz assures that the $0°$ phase shift in the plot has been identified.

The RF frequency is manually tuned over the range 2854 MHz to 2858 MHz while the oscilloscope traces of the cavity mode spectrum and RAM signal are captured five times at each frequency step. A Python-based data analysis script is used to compute the normalized RAM amplitudes. The scope traces are low-pass filtered and used to find the peak-to-peak voltages of both the spectrum and RAM signals. The RAM signal amplitude is then normalized using the corresponding TEM_{00} mode amplitude to account for variations in laser power or drive signal amplitude at the time of acquisition. Figure 2.21 shows sample RAM waveforms captured at several frequency offsets. Due to frequency jitter, the location of the TEM_{00} modes in the spectrum trace can vary by several hundred microseconds between samples. However, five such traces captured at a given frequency step have normalized amplitudes consistent to within 1.3 %. The full data set plotted in Figure 2.22 shows excellent agreement with the simulation prediction for $0°$ plotted in Figure 2.19. The asymmetry is most likely due to a slight error in mixing phase and could be eliminated with more rigorous calibration. Optimization of the phase shift for ± 0.3 MHz offsets should improve the symmetry; however, the effect on the final result is likely negligible.

Two data sets are plotted in Figure 2.22. For the first data set, the phase shift was set by maximizing the RAM signal for a 0.1 MHz offset. These data agree quite well with the 0.3π curve in Figure 2.19; however, the minimum is ambiguous. The second data set used the phase shifter optimization technique discussed above. These data agree well with $\phi = 0°$ curve with a very sharp central peak. After experimenting with a variety of functions approximating these data, $y = A|\sin(B(x-C))|$ provides this most compelling fit to the central peak in data set 2. The least squares fit to the range -0.45 MHz to 0.45 MHz results in a peak centered at 8.3 kHz $\pm$ 1.7 kHz and is shown in Figure 2.23. This frequency offset corresponds to a cavity length deviation of 1.4 µm $\pm$ 0.3 µm. This measured offset is an error in the cavity length which may be corrected with a micrometer or piezo. But the real significance of this result is the uncertainty. This technique allows the initial cavity length to be set and measured with a precision of just 300 nm, a factor of 30 improvement over the manual micrometer adjustment described earlier.

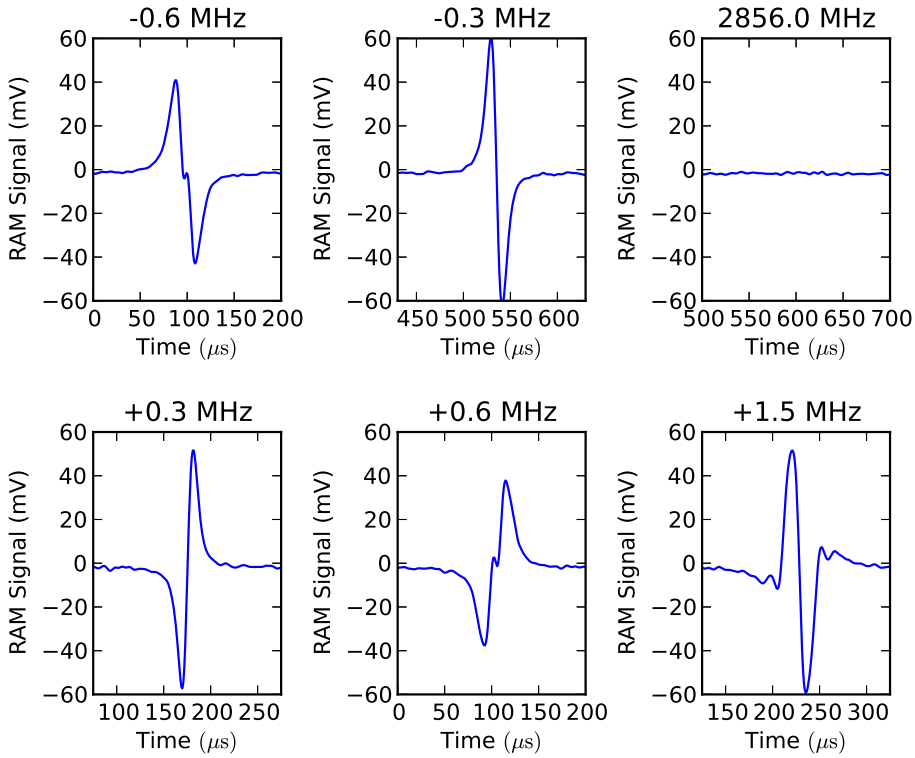

Figure 2.21: Measured, un-normalized residual amplitude modulation signal for various RF offset frequencies (The horizontal scale is the same for all plots but offset)

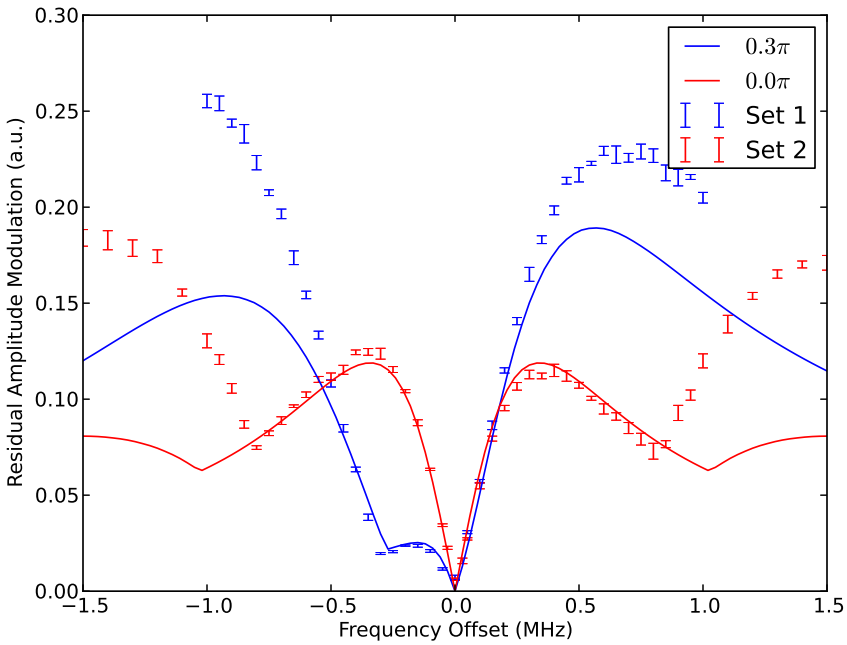

Figure 2.22: Cavity length measurement using the RAM technique. Experimental data are normalized against the apparent TEM_{00} amplitude whereas the simulated results are normalized against the actual TEM_{00} amplitude. This difference in normalization is the most likely reason that the curves diverge far from 0 MHz. The central minima of the two data sets however are in close agreement with the simulated results for each phase shift. The simulated results are only for a pure TEM_{00} cavity mode while in reality there are several nearby higher order modes whose own RAM effects will superpose with that of the TEM_{00}. This likely explains the difference between the position of the cusp in the 0.0π data and the simulation.

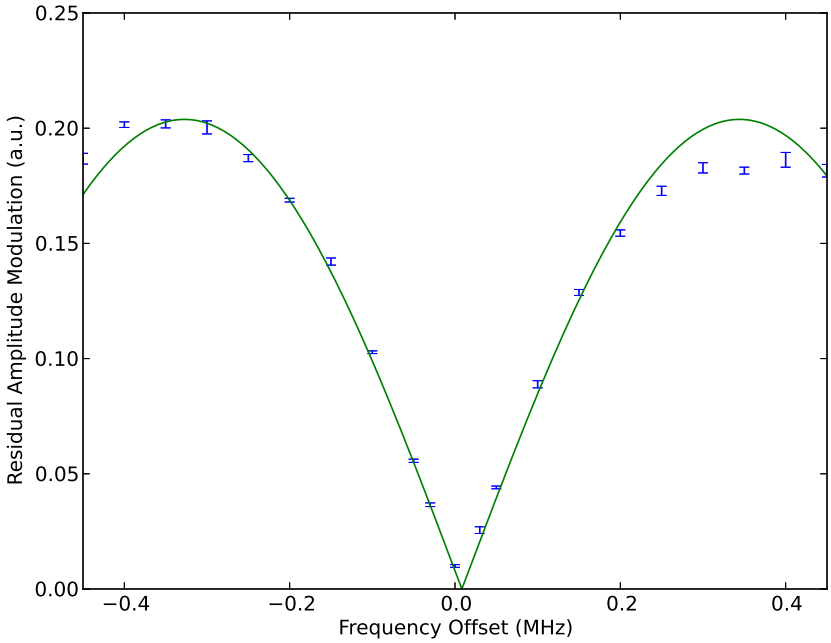

Figure 2.23: The central peak of data set 2 is fit by the function $y = A|\sin(B(x - C))|$.

Provided that care is taken in adjusting the mixing phase, the cavity length may be very precisely measured. An offset measured by this technique can then be converted to a cavity length error using the relationship:

$$\frac{\Delta L}{L} = \frac{\Delta f}{f} \tag{2.10}$$

Where L is the cavity length and $f = 2856\,\text{MHz}$ is the modulation frequency. The error may be corrected by adjusting the fine micrometer or piezo bias voltage to mirror M4, then repeating the RAM experiment to confirm the correction.

Finesse Measurement

The presence of the RF modulation sidebands used for the RAM measurements can also serve as a convenient tool for measuring the cavity finesse. An RF modulation frequency of 2861 MHz results in sidebands displaced 5 MHz from the nearest TEM_{00} mode in the spectrum. The finesse of a Fabrey-Perot resonator is defined as[22, pg.436]

$$\mathcal{F} = 2\pi/\delta_c \tag{2.11}$$

where $\delta_c \ll 1$ is the sum of all fractional losses within the cavity. The finesse is also defined in the frequency domain as the ratio

$$\mathcal{F} = \nu_{\text{ax}}/\Delta\nu_{\text{FWHM}} \tag{2.12}$$

for a cavity with free spectral range $\nu_{\text{ax}} = c/2L$ and resonance linewidth $\Delta\nu_{\text{FWHM}}$. Scanning the cavity length by one half wavelength will span one full free spectral range in frequency. By observing this scan on an oscilloscope the distance between two successive TEM_{00} modes can be used as a measure of ν_{ax} and the TEM_{00} linewidth can be measured. This method is problematic, particularly at slow scan rates, because of cavity drift, jitter, and non-linearity in the motion. As already discussed in Section 2.3.6, the piezo response will have some residual non-linearity and, due to low-frequency resonances, the motion may have harmonic content. The alternative technique developed here is to utilize the RF sidebands applied for the RAM technique as a spectral 'yardstick' to calibrate the frequency axis and to measure the absolute width of the TEM_{00} mode. While the cavity is still scanned at the low rate of 50 Hz, the region of interest now only needs to span the TEM_{00} mode and its sidebands (0.35 ms rather than 3.72 ms). Furthermore, the oscilloscope is configured to capture only the center $\pm\pi/3$ region of the stage motion in order to avoid nonlinear motion near the inflection points at $\pm\pi/2$. Figure 2.24 shows an example of data captured to measure the cavity finesse. The data analysis script (implemented in Python) first applies a low pass filter with a cutoff chosen to smooth the data yet not distort the peaks of interest. Next, a peak finding algorithm locates the largest peak in the data (assumed to be TEM_{00}) and the two adjacent peaks, which are assumed to be its sidebands. Large irregularities in the symmetry of the sidebands (or a missing sideband) result in the automatic rejection of the scope trace. The time axis is then calibrated to frequency by equating the measured sideband temporal spacing with the known frequency offset of 5 MHz. Linear interpolation of the filtered data is used to find the width of the TEM_{00} peak on the new frequency axis at half of the peak amplitude. Figure 2.25 shows the spectrum resulting from this analysis for the raw data in Figure 2.24.

Jitter and drift in the cavity length result in a fairly unstable cavity mode spectrum. This effect is alleviated by acquiring many oscilloscope traces in sequence. For each

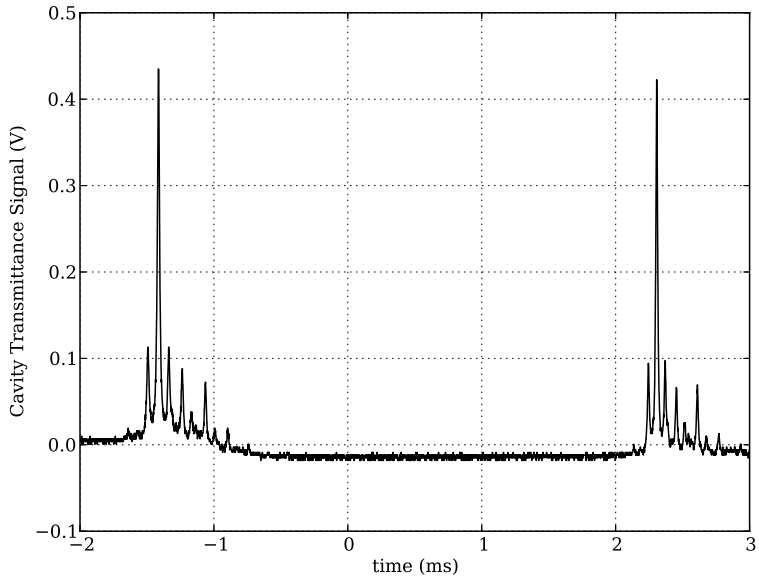

Figure 2.24: A raw oscilloscope trace for a cavity scan shows the transverse mode structure for two adjacent axial modes.

trace, the FWHM linewidth is computed using the sideband spacing technique. An average of 25 successive oscilloscope traces has proven to give a fractional uncertainty $< 1\,\%$, although usually at least twice this much data is taken.

Several experiments have shown that the measured TEM_{00} linewidth is invariant to the RF sideband offset frequency, provided that the sidebands are separated enough to not distort the TEM_{00} mode shape. A sideband offset of 5 MHz was chosen as the lowest frequency that provides good isolation from the $\sim 1\,\mathrm{MHz}$ wide TEM_{00} mode.

The statistical approach to this technique has been very effective in removing the effects of cavity drift and jitter, easily making cavity linewidth measurements with $0.1\,\%$ uncertainty. The use of these linewidths to estimate the cavity finesse have not been as reliable, however. Repeated measurements under the same cavity configuration give linewidths consistent to within only $2\,\%$. Varying the cavity length should not effect the finesse. However, measurements of the linewidth for five cavity mirror displacements over a $400\,\mu\mathrm{m}$ range result in a finesse of 240 ± 33. Earlier finesse measurements found a finesse as high as 330, but these results have not been repeatable after a realignment of the cavity. At each new cavity mirror position the mirror must be steered to re-optimize

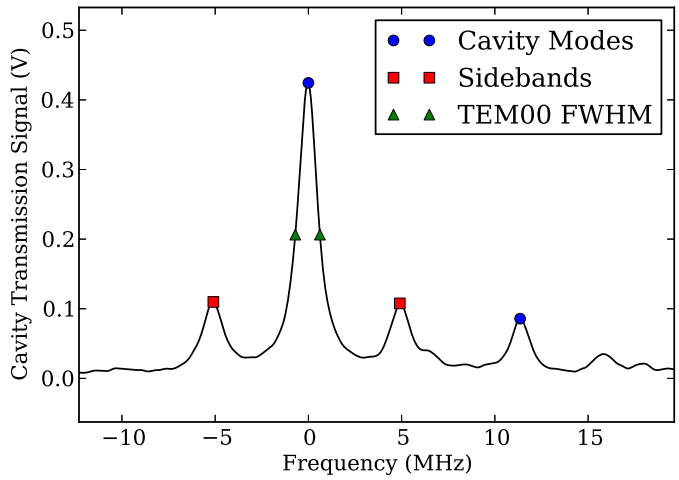

Figure 2.25: A data analysis code automatically identifies the peaks in the cavity mode spectrum and computes the spacings and linewidths.

the TEM_{00} mode making this most likely an error due to cavity alignment. To verify the effect of cavity alignment on the finesse the vertical cavity alignment was perturbed such that the TEM_{00} mode intensity falls by 50 %. This perturbation changed the mode width by 13 %. Restoring the cavity alignment by maximizing the TEM_{00} intensity returned the mode width to within 2 % of its original value. It is possible, given that the cavity has a divergence asymmetry for the x and y axes of the beam, that nearly degenerate transverse modes could beat producing a low frequency sideband which broadens the TEM_{00} mode. This effect would be highly dependent on cavity alignment.

In order for this technique to accurately measure the finesse of an optical storage cavity, several improvements must be made to the cavity mechanics. Increasing the cavity mirror steering lever arm from 3" will effectively increase the resolution of the motors used for mirror steering. Presently the intensity of the cavity modes is reduced by half with a motor motion of fewer than 10 step increments of 30 µrad with a hysteresis of more than 30 steps ($\sim$ 1 mrad). More care must also be taken to align the mirror M1 translation stage to the cavity axis so that the cavity alignment is not perturbed by longitudinal displacements of several hundred µm. Gimbaled mirror mounts would greatly improve performance by removing longitudinal displacement effects while steering the mirror. With these improvements the technique should be capable of repeatably measuring a finesse value closer to the design specification of $\mathcal{F} > 450$. The beam aberrations discussed in Section 2.3.2 could

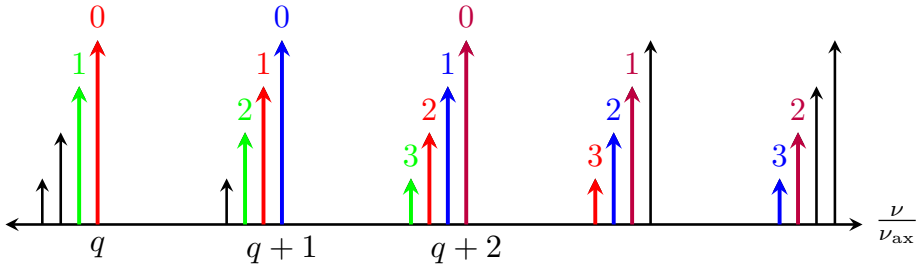

Figure 2.26: (color) The transverse mode spectrum of a near concentric cavity. Each qth order of TEM_{00} mode and its first three transverse modes are plotted in the same color.

also lead to increased cavity loss from the loss of the skew ray portion of the beam after many passes in the cavity. It is also possible that the mirror surface quality has degraded since installation due to dust accumulation and water absorption in the coating, although no such obvious damage is visible.

Gouy Phase Shift

A gaussian beam with Rayleigh range z_R focussed through a waist experiences an addition phase shift of

$$\zeta(z) = \tan^{-1}(z/z_R) \tag{2.13}$$

known as the Gouy phase shift. For higher order Hermite-gaussian modes the net phase shift is actually $(m+n+1)\zeta(z)$ where m and n are the mode orders of the x and y components of the beam[22]. Because the cavity round trip net phase shift depends on mode order, different modes will not have the same resonant frequency.

The presence of additional transverse modes in Figures 2.25 and 2.24 suggests that the cavity Gouy phase shift can also be measured using the RF sideband calibration. This phase shift can provide a direct measure of the cavity's focusing geometry.

In this instance we assume a symmetric two mirror cavity with identical spherical mirrors. This assumption is justified since the focusing elements and flat mirror of the two- and three-mirror cavities only serve to retro-reflect light in the same manner as a single spherical mirror. The Gouy phase shift experienced in one round trip is not altered by the presence of the collimated leg of the cavity (only linear phase is accumulated here) and the Gouy phase is identical to the case of a spherical mirror with radius of curvature $R = f$

where f is the focal length of the collimating optic(s). For a resonator of length L and mirror radius R the cavity 'g' parameter is defined as:

$$g = 1 - \frac{L}{R} \tag{2.14}$$

For a cavity with two identical spherical mirrors of radius R, there is a single g and the resonant frequencies of the cavity modes can be written as:

$$\nu = \nu_{\text{ax}} q + (n + m + 1)\Delta\nu \tag{2.15}$$

where $\nu_{\text{ax}} = c/2L$ is the cavity free spectral range and the mode spacing is

$$\Delta\nu = \nu_{\text{ax}} \frac{\cos^{-1} g}{\pi} \tag{2.16}$$

For a near-concentric resonator where the centers of curvature of the two mirrors overlap by s

$$g = -1 + \frac{s}{R} \tag{2.17}$$

As $s \to 0$ the frequency spacing $\delta\nu \to \nu_{\text{ax}}$ and the modes become degenerate. Figure 2.26 shows the cavity mode structure for a near-concentric cavity.

Knowledge of the Gouy phase shift, ζ, gives us the cavity length L if all of the other parameters are known. We use these relationships along with the RF sideband ruler technique to measure the concentricity s of the four-mirror cavity. It is important to note that in the four-mirror cavity the focal lengths and positions of the cylindrical mirrors are not identical for the two principal axes, resulting in a different Gouy phase shift in each principal axis.

Figure 2.18 shows the transverse mode spectrum of the four-mirror cavity with each mode's order identified. The mean TEM_{i0} frequency offset is $10.98\,\text{MHz} \pm 0.12\,\text{MHz}$ and the mean TEM_{0j} frequency offset is $7.94\,\text{MHz} \pm 0.38\,\text{MHz}$ as measured from Figure 2.18 using 5 MHz sidebands on a prior oscilloscope trace to calibrate frequencies of each mode. These offsets are relative to the nearest TEM_{00} mode (of different order q) so the Gouy phase shift can be written in terms of this offset $\delta\nu$

$$\zeta = \pi(1 - \frac{\delta\nu}{\nu_{\text{ax}}}) \tag{2.18}$$

The Gouy phase can also be derived from $g = -|\cos\zeta|$ so it is now possible to determine the cavity g for each axis using the frequency offset results. The cavity concentricity is then

$$\Delta s = (1 + g)R \tag{2.19}$$

The Figure 2.18 data results in cavity concentricity's of

$$s_{x'} = 1.18\,\mathrm{mm} \pm 0.02\,\mathrm{mm} \tag{2.20}$$

$$s_{y'} = 0.62\,\mathrm{mm} \pm 0.06\,\mathrm{mm} \tag{2.21}$$

for the rotated principal axes seen in Figure 2.17. Using these results the mirror M1 position can be adjusted to achieve the desired cavity concentricity and waist size. These data also indicate that the residual astigmatism of the cavity is $s_{x'} - s_{y'} = 0.56\,\mathrm{mm} \pm 0.06\,\mathrm{mm}$, below the 1 mm requirement.

This technique looks promising as a method of precisely determining the concentricity of the optical storage cavity. The measured concentricity uncertainty of 60 µm is larger than desired; however, this result is based on analysis of only a single oscilloscope trace. Presently the process of tagging the modes in the spectrum is quite labor intensive. With appropriate automation it will be possible to obtain the statistics needed to reduce the uncertainty to a suitable resolution for the concentricity of 8 µm required for x-ray production.

2.3.7 Mechanical Resonance Limitations

In order to scan the cavity length with a linear relationship to the cavity mode frequency, a ramp function was initially used to drive the piezo transducer on mirror M4. However, this drive produced irregular motion when compared with a sinusoid due to the excitation of mechanical resonances by the higher harmonic content in the ramp waveform. An LVDT displacement sensor was installed on the piezo driven translation stage (M4) to track the actual response of the stage to the piezo drive voltage. The LVDT amplitude and phase response was measured as a function of the driving sinusoid frequency and is shown in Figure 2.27. These data show a strong mechanical resonance at the low frequency of 96 Hz. Even with a driving frequency as low as 50 Hz the stage experienced significant phase lag and is extraordinarily sensitive to vibrational noise. This resonance appears to be the due to the 1.5 "⌀ post on which mirrors M2, M3, and M4 are mounted. Two additional optical posts were installed in light contact with the mounting platform which provided some additional damping; this resulted in the the first resonant frequency moving up to ~ 140 Hz, thus making scans at 50 Hz useful. Many additional resonances were also found for higher driving frequencies. It is clear that great care must be taken in future designs to mitigate the effects of unwanted mechanical resonances. Since the beamline is 6.5" above

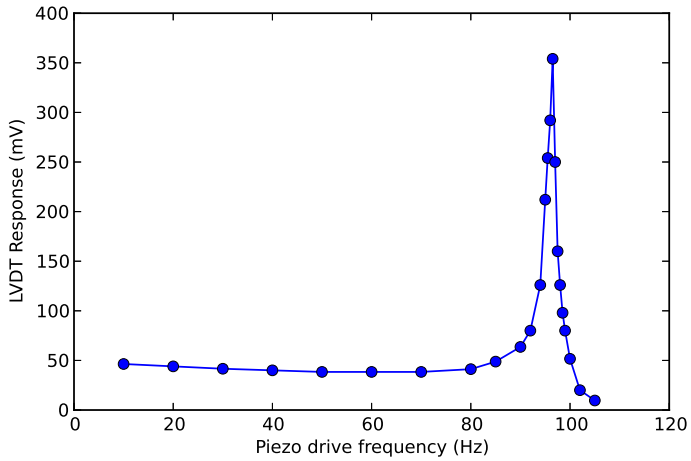

Figure 2.27: Translation stage response to pieze drive frequency showing a strong resonance at 96 Hz

the table, far more rigid mounting structures are needed for all cavity optics before a fully functional stabilization system can be implemented. This is especially important since the principle noise components of the system are acoustic at several kHz, presently beyond the feedback bandwidth of the system. The cavity experiments discussed in this chapter were performed with a sinusoidal piezo drive frequency of 50 Hz to avoid the effects of the 140 Hz resonance.

Cavity Length Stability

The short term stability of the cavity can be assessed through observation of TEM_{00} mode position on the oscilloscope while scanning the cavity length in the manner described above. In one minute the TEM_{00} mode experiences a fast random jitter of about 0.03 times the FSR but does not drift by more than ± 1 FSR within a 1 min observation period. This corresponds to cavity length jitter of $3.4\,\mathrm{nm}_{\mathrm{RMS}}$ and drifts over ± 300 nm. The cavity is quite sensitive to acoustic noise in the room; talking loudly near the apparatus can double the amplitude of the fast jitter. The noise observed is most likely due to vibrations from building air conditioning or cooling fans on lab equipment. The slower drift component will easily be removed by active stabilization of the existing system, however, the higher frequency noise will require a higher feedback bandwidth than is available with the existing mounts. The stabilization system will need to lock the cavity length to a precision better

than the 0.3 nm cavity linewidth to achieve a stable mode. Appendix A describes the proposed stabilization system design in detail.

2.4 Infrared High Power Storage Cavity Test-Bench

The next stage of the project is the development of a test cavity for use with high power infrared pulses from the MkV FEL. While the low power cavity enabled us to test the geometrical properties of the cavity the IR cavity allows us to:

- Develop IR cavity stabilization systems
- Demonstrate the auxiliary cavity stabilization system.
- Measure the mirror coating reflectance and IR cavity finesse.
- Demonstrate pulse stacking with GHz repetition rate.
- Measure the effects of dispersion in the mirror coatings.
- Assess the thermal distortion of the mirrors/coatings in a high power cavity.
- Test the coating damage threshold.

These developments represent a major component of MkV FEL Lab's present research objectives and they will be addressed in the near future.

2.5 Conclusions

The development of an optical storage cavity is a very promising pathway towards a viable compact, low-cost, high-brightness x-ray source. This research effort has examined many of the challenges involved in the design, construction and commissioning of a three- or four-mirror cavity. Experiments using the four-mirror visible test cavity have demonstrated:

- A four-mirror optical cavity using an astigmatism compensating cylindrical mirror pair is able to achieve near-diffraction limited performance.
- Detailed alignment procedures have been developed for optimization of a four-mirror storage cavity.

- An RF side band technique has been demonstrated for the precision synchronization of the cavity free spectral range to an RF reference.
- The RF sideband system was used to measure the finesse of the optical cavity.
- The cavity concentricity can be precisely measured by using the RF sideband technique to obtain the Gouy phase shift of the cavity.

It is clear from these experiments that in future storage cavity experiments, more attention must be paid to the design of robust optical mounts. Vibration and mechanical resonances were determined to be the key limitations to increasing the concentricity of the cavity to achieve the small spot size required for x-ray generation. Raytracing simulations are also a powerful tool for the development of alignment procedures by exposing the causes of aberrations possible in complex optical systems.

Future development of the optical storage cavity will include the implementation of a cavity stabilization system for the four-mirror test cavity and construction of an infrared high-power test cavity. Stabilization of the four-mirror test cavity will allow further experimentation involving optimization of the cavity for single mode TEM_{00} performance as well as realtime adjustments of the concentricity. The infrared cavity will allow performance testing of the optical coatings to be used in the full-up storage cavity for x-ray production.

Chapter 3

Stabilized Tunable Reference Laser

3.1 Introduction

A principal feature of the Compton backscatter x-ray source is the ability to easily tune the wavelength and photon energy. The photon energy is most sensitive to changes in electron beam energy, however, changing the beam energy requires reconfiguration of the accelerator and beam transport optics, which may also require re-optimization of the FEL and storage cavity after such a change. It is far more convenient to exploit the tunability of the free electron laser for this purpose. While broad tuning of the MkV FEL requires adjustment of wiggler gap, fine tuning can be achieved simply by adjusting the length of the laser resonator. Changes to the FEL wavelength will in turn require re-tuning of the optical storage cavity to maintain resonance. Both resonators require active cavity length stabilization to compensate for drift and vibrations in order to maximize the x-ray source yield. This chapter describes the development of a stable tunable laser system to be used as an optical frequency reference for both the FEL and optical storage cavity. By sharing a common reference source both resonators can be simultaneously and precisely tuned simply by varying the frequency of a single RF generator without losing synchronism between the two cavities.

This system stabilizes and sets the frequency of a tunable diode laser (TDL) with respect to a stable fixed frequency reference, in this case a commercial frequency stabilized helium-neon (HeNe) laser. Tunable laser stabilization is achieved by an optical phase-locking technique known as frequency offset locking [33, 34]. This opto-electronic heterodyne technique, originally developed for atomic spectroscopy, compares the beat frequency between the tunable diode laser and reference HeNe with that of an external RF signal.

The phase/frequency error between these signals is used to form an error signal with which to tune the diode laser, thus closing the optical phase-locked loop.

This method of frequency locking was developed to lock tunable diode lasers to atomic frequency references, thus reducing their frequency fluctuations below 50 Hz in some cases. It has been shown, using this technique, that controlled optical frequency sweeping can be accomplished by varying the frequency of the RF source [35, 36]. The performance of these tunable stabilization systems is limited primarily by availability of wide-band microwave electronics. The broad tunability of the free electron laser provides a unique challenge since most commercial microwave technology is narrowband. The tunability of the FEL requires an RF system that is operable continuously over several GHz. Advances in microwave technologies, particularly in high speed GaAs semiconductor devices, have made the solution discussed in this chapter realizable.

Frequency locking of the TDL to the stabilized HeNe is expected to improve the frequency stability of the diode from $\pm 2\,\mathrm{GHz}$ to $\pm 2\,\mathrm{MHz}$ over an 8 hour time scale. While the TDL line width of $\approx 750\,\mathrm{kHz}$ is sufficient for its application to the FEL stabilization problem, better short term stability could in principle be achieved by use of an atomically stabilized HeNe reference laser and a higher bandwidth feedback loop.

This system offers several advantages over an all optical stabilization system. It is fairly insensitive to misalignments and variations in laser intensity, the latter becoming significant as the HeNe laser tube ages. The tunability of the system also does not rely on the variation of any sensitive optical alignment. Also, none of the optical elements involved has a significant thermal sensitivity. An all optical system designed to achieve the same stability would necessarily involve several high precision, high cost optics.

3.2 Conceptual Overview

In Figure 3.1, a tunable laser and a fixed wavelength reference laser are coincident on a fast photodetector. These two beams can be treated approximately as co-propagating plane waves (assuming proper mode matching) by:

$$E_{\mathrm{det}}(t) = E_D \cos((\omega_D + \delta\omega)t + \phi_D) + E_H \cos(\omega_H t + \phi_H) \tag{3.1}$$

where the tunable laser frequency $\omega_D = \omega_H + \omega_0$ differs from the reference laser frequency ω_H by a variable offset ω_0. An error in the tunable laser's frequency is included

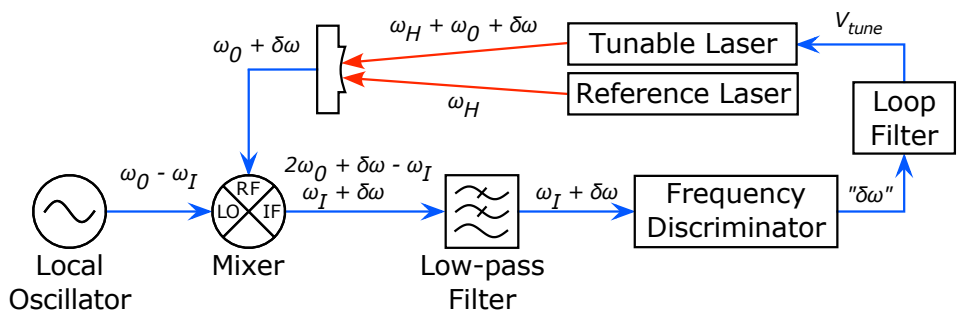

Figure 3.1: The stabilized tunable laser system mixes a tunable laser with a stable reference laser. ω_H is the frequency of the reference HeNe laser while ω_0 is the offset frequency of the tunable laser with respect to ω_H. The deviation of the tunable laser is denoted by the error term $\delta\omega$.

as $\delta\omega$. The resulting signal as measured with the AC coupled square-law photodetector only consists of a component oscillating at the beat frequency between the lasers.

$$\omega_S = \omega_D - \omega_H = \omega_0 + \delta\omega \tag{3.2}$$

The system is tuned to the desired frequency offset (on the order of several GHz) by adjusting the local oscillator frequency $\omega_L = \omega_0 - \omega_I$ where ω_I is a fixed, low frequency offset (on the order of 30 MHz). The local oscillator signal (LO) is mixed with the photodiode signal (RF) in a double-balanced mixer (MX).

The mixer output contains two frequency components: the sum frequency $2\omega_0 - \omega_I + \delta\omega$ and the difference frequency $\omega_I + \delta\omega$. This difference frequency component contains the tunable laser's error, $\delta\omega$, as a frequency modulation on an ω_I carrier. The higher sum frequency component is of no interest, typically out of band for the electronics, and is filtered out. The frequency modulated error $\delta\omega$ is precisely the error signal required to compensate the error in the tunable laser frequency and can be extracted by standard FM demodulation techniques. Note that the local oscillator frequency, ω_L, may be larger or smaller than the photodiode output frequency, ω_s, so the intermediate frequency ω_I may be positive or negative. In general, FM demodulators do not differentiate between positive and negative frequencies so the lock points $\pm\omega_I$ are degenerate.

The simplest but least robust technique for demodulation of an FM signal is by the 'slope' method [37, p.899]. By designing a low-pass filter such that the signal at the

intermediate frequency ω_I is attenuated by 50%, variations in frequency will produce variations in the attenuation. The attenuation for a 6 dB per octave filter is given for $\delta\omega \ll \omega_I$ by:

$$A = \frac{1}{2}\left(\frac{1}{4}\right)^{\frac{\delta\omega}{\omega_I}} \simeq \frac{1}{2}\left(1 - 1.39\left(\frac{\delta\omega}{\omega_I}\right) + 0.97\left(\frac{\delta\omega}{\omega_I}\right)^2 + \cdots\right)$$

Rectification of the signal followed by a second low-pass filter to smooth out the ω_I ripple results in a near-DC voltage that varies approximately linearly with the frequency error $\delta\omega$. Due to the logarithmic nature of the low-pass filter roll-off, the signal generated is only approximately linear in $\delta\omega$ over a very narrow range. Such a system has rather limited sensitivity and is subject to error from signal amplitude fluctuations. This technique is used for initial testing of the stabilization system due to its simplicity. However, several, more robust techniques are described along with their challenges and benefits.

The more common method of demodulating an FM signal is by use of a phase-locked loop in which a voltage controlled oscillator (VCO) has its frequency compared to the input signal by a phase/frequency detector. A voltage proportional to the frequency difference between the two signals is fed back to the VCO as a correction forcing the oscillator to track the input frequency. This correction signal is directly proportional to the error signal, $\delta\omega$, which we wish to extract for feedback to the tunable laser. Due to the rapid phase excursions that are present in the laser beat signal it is not practical to implement a standard phase-locked-loop. Prevedelli described the construction and use of a digital frequency-phase detector with extended phase tracking range designed for this purpose[38]. The digital logic described in this work is readily implemented on a field-programmable-gate-array (FPGA) programmable logic device. However there are a number engineering challenges presented in the design and construction of the RF front end electronics for this type of system. Due to the lack of a commercially available system with adequate bandwidth, this technique will not be applied to this project at present.

Another option for implementing this type of digital phase-locked-loop lies in using software defined radio (SDR). SDR relies on the digital sampling of an RF signal as early in the signal chain as possible. In our case the beat signal between the two lasers is multi-GHz but the IF can be selected at any lower frequency (10.7 MHz was chosen in this case). The SDR can digitize the entire IF waveform and perform demodulation either in firmware (on the board) or software (on a computer). Advanced digital signal processing (DSP) techniques can provide accurate and very wide bandwidth demodulation with far greater

ease and system simplicity than the above mentioned techniques and thus is ideally suited to the requirements of our system. A preliminary SDR based system has been developed for use with this project and is described in Section 3.4.1. This system was promising but was abandoned due to technical difficulties with the chosen SDR hardware in favor of the analog method mentioned above. The SDR system has proven extremely useful as a data acquisition tool for system diagnostics in Section 3.4.2. The challenges involved in adopting an SDR based feedback controller are not insurmountable but exceed the resources presently available to this project.

With the demodulated error signal already digitized, the control signals needed to feed back to the TDL for correction can also be derived through DSP techniques. The accuracy and reliability of DSP based feedback systems is much improved over their analog counterparts. If a proportional-integral-differential (PID) control system is implemented then the tuning parameters can be varied easily and repeatable as compared with the analog counterpart. Computer control also allows for sophisticated optimization schemes and precisely recalled configurations.

3.3 System Implementation

3.3.1 Overview

Figure 3.2 shows the intended practical implementation of the system described in Section 3.2. Beamsplitter BS1 is used to sample the tunable diode laser (TDL) beam for stabilization while the remaining beam is available to dependent systems via a Faraday isolator. The TDL beam is combined with the stabilized reference laser (HeNe) in a 50:50 non-polarizing beamsplitter. Appropriate mode matching and focusing optics (OPT) are used to image the combined beams onto the photodetector (DET1) active area of 0.2mm x 0.2mm.

The laser beat signal is detected by a Hamamatsu G4176 GaAs photodiode with a 30 ps rise time. This diode is conveniently packaged in a TO-5 package with integrated SMA connector and bypass capacitor. This diode screws directly onto the Minicircuits 12 GHz bias tee and followed by a pair of 8 GHz, 10 dB amplifiers. All microwave components are packaged with SMA connectors with 50 Ω impedance for simplicity in system assembly and testing.

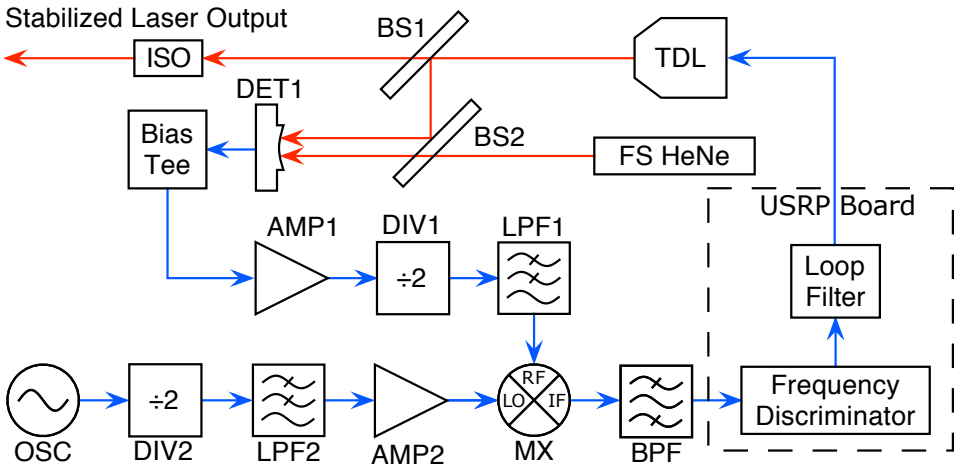

Figure 3.2: The Stabilized Tunable Reference Laser system consists of HeNe laser and a tunable diode laser (TDL), which are co-incident on a detector to generate a GHz range beat signal. This signal is then amplified, divided in frequency and mixed with a microwave reference oscillator. The resulting heterodyne signal represents the frequency error, which is fed back to the diode laser for stabilization. The individual components are described in Table 3.1.

The Newfocus TLB-7000 tunable diode laser (TDL) has an effective tuning range of 150 GHz; however, the actual tuning range of this system is limited by available microwave technology. A limit of 4 GHz bandwidth is imposed by the chosen mixer (MX) but a divide-by-two prescaler (DIV1) extends this to 8 GHz. A larger divide ratio could extend this even further, limited mainly by the photodetector used. While the tuning bandwidth can be extended in this manner, the sensitivity of the system for stabilization is reduced by the prescale factor. Another benefit of the prescaler is an insensitivity to the photodetector amplitude. The prescaler acts as a limiter accepting an input signal over a 25 dB dynamic range and outputting a fixed amplitude signal. A low pass filter (LPF1) should be used after the prescaler to smooth the transient behavior of the digital signal and remove harmonics due to the limited output.

The available HP8648C signal generator (OSC) functions from 0 MHz to 3200 MHz and is thus well suited for locking to beat signals up to 6400 MHz (before prescaling). A future improvement to the system would be replacement of DIV1 by a divide-by-eight prescaler and OSC by a signal generator covering the range from DC to 1 GHz, thus allowing most of the system to operate at significantly lower frequencies. This simplifies the design since

Table 3.1: STRL system components shown in Figure 3.2

Component	Description	Vendor
FS HeNe	Frequency Stabilized Helium-Neon Laser	Melles-Griot
TDL	Tunable Diode Laser	New Focus
ISO	Faraday Isolator	OFR
BS1	Wedged Brewster window	
BS2	50/50 Beamsplitter	
DET1	Fast Photodiode - 8 GHz detection bandwidth	Hamamatsu
BIAS	Wide-band bias tee and and DC block	Minicircuits
AMP1	Wide-band amplifier	Minicircuits
DIV1,2	Divide-by-2 microwave prescalers	Hittite Microwave
LPF1,2	Harmonic blocking filters	
OSC	Wide-band tunable RF source/synthesizer	HP
AMP2	Wide-band amplifier	Minicircuits
MX	Double-Balanced RF Mixer	Minicircuits
BPF	High rejection bandpass filter	
OPT	Mode matching lenses (not shown)	
USRP	Universal Software Radio Peripheral	Ettus Research

higher frequency RF signals require more specialized components such as cables, connectors and amplifiers.

The mixer output signal of interest is isolated by a high rejection band-pass filter (BPF) centered at the intermediate frequency $\omega_I = 10.7\,\mathrm{MHz}$. The TDL frequency error $\delta\omega$ is frequency modulated onto the surviving ω_I carrier and demodulation is accomplished using readily available SDR hardware and software.

Finally, a loop filter control circuit converts the detected error signal into a control voltage suitable for feedback to the diode laser. This loop filter has many possible analog and digital implementations. The design of such loop closing filters depends heavily on the performance characteristics of the system described above as well as the dynamics of the control inputs on the TDL itself. It is natural to incorporate the loop filter into the SDR subsystem for a complete digital control solution.

3.3.2 Stabilized HeNe Frequency Ripple

It was observed while testing the PDH stabilization system (see Section A.4) that the Melles-Griot stabilized HeNe laser produces a 30 % intensity ripple at 5.26 kHz when the cavity is on resonance. This noise appeared to be a product of the laser's internal stabilization servo as no other system components have a 5 kHz component. Close examination of the laser intensity on a DC photodiode shows short pulses of 4.9 mV amplitude at 5.26 kHz superimposed on the 580 mV_{DC} photodiode signal. This ripple is a factor of 40 lower than the ripple seen in the cavity resonance, so clearly even a small ripple is problematic when injected into a resonant cavity. In fact it proved impossible to lock a related 2 m cavity with the PDH technique with this ripple present.

The Melles-Griot user manual does indeed list a 5 kHz servo noise among the laser specifications but does not provide schematics or details about the function of the servo system. Thanks to Sams's Laser FAQ[39] a schematic for the laser controller was obtained showing that the 5 kHz ripple is in fact due to the pulse width modulated drive to the laser heater. The heater controls the temperature of the HeNe laser tube and thus its cavity length and frequency. Pulse width modulation is used to increase the efficiency of the circuitry at the expense of increased ripple. Sam's Laser FAQ describes a modification to the circuit board to convert the pulsed heater drive with a DC drive.

With the laser heater ripple reduced from 10.7 $V_{p\text{-}p}$ to 430 mV the pulses are no longer visible on the DC photodiode signal.

3.4 System Realization

The "as built" STRL system differs from the above design in several ways. First, the microwave pre-scaler was damaged during initial testing and is not present in the final system; thus limiting the tuning range to the 3.2 GHz range of the HP8648C signal source. Initial tests of the pre-scaler were successful before damage so it is reasonable to assume that the technique will extend the tuning range as described above. Second, the complexity of the firmware development effort required for utilization of the Universal Software Radio Peripheral (USRP) as a demodulator and feedback controller was beyond the scope of this researcher's intent for the project. The USRP hardware resources turned out to be only marginally sufficient for this design. The Cyclone I FPGA provided on the USRP is not adequate for the complex digital system processing tasks required of it. Particularly

problematic is the lack of hardware multiplier circuitry needed for the most routine DSP computations. Many common DSP design tasks are provided by the FPGA vendor at prohibitive cost and thus would have to be designed and debugged from scratch. While of educational value this firmware design effort was beyond the scope of this project. The USRP system still proves to be useful as a system diagnostic tool, as will be discussed. The demodulation and control functions are now handled by custom built analog circuitry. The complete optical apparatus is shown in Figure 3.3.

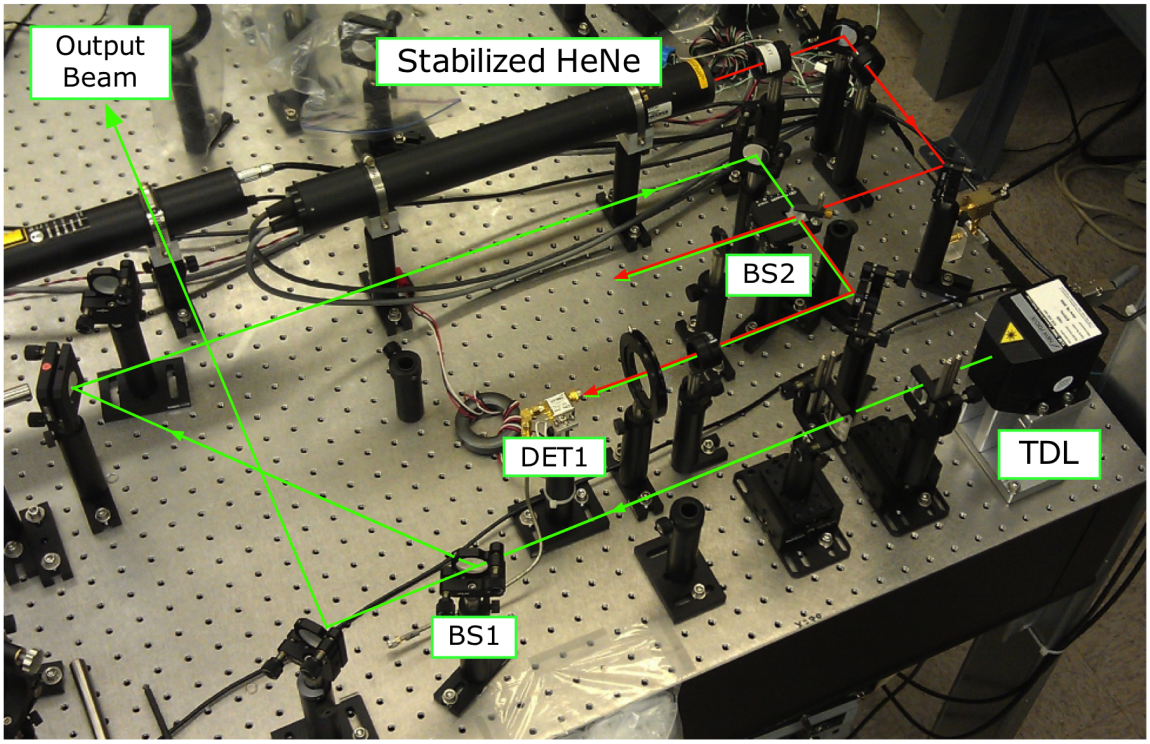

Figure 3.3: The tunable diode laser beam (TDL) shown in green, and the HeNe beam (red) are combined in 50:50 beamsplitter cube (BS2). The co-aligned beams are then both incident on the GaAs photodetector (DET1). Only a few percent of the TDL beam is sampled by BS1 for the STRL system, the remainder of the beam is available for use as a frequency reference for other stabilization systems.

Figure 3.4: The Universal Software Radio Peripheral (USRP) from Ettus Research[3]

3.4.1 Software Defined Radio Hardware

3.4.2 USRP Diagnostics

Demodulation of the error signal from the IF can be accomplished using the Universal Software Radio Peripheral[3] (USRP) and the GNU Radio[40] software suite (see Figure 3.4). The USRP is a flexible SDR hardware platform incorporating analog to digital conversion and digital signal processing technology. Input signals are sampled by the USRP analog to digital converters (ADCs) and digitally preprocessed by an FPGA for transmission to a computer via USB. The open-source, free software GNU Radio performs the digital demodulation and signal processing before transmitting the results back to the USRP board. The USRP digital-to-analog converters then generate the analog signal used to control the TDL. If higher processing speeds are required than can be provided by the computer and USB connection then the FPGA firmware may be customized to perform any necessary tasks.

In addition to performing the functions of frequency discriminator and loop filter, we will also have the capability to record the data which is required to perform analyses of system stability. Data collected could be used to calculate the Allan Variance, a common figure of merit for oscillator stability[41].

The USRP is very flexible in that the FPGA firmware and GNU Radio software can be reprogrammed and repurposed at any time. Interchangeable daughterboards are used as the RF front ends for the USRP and allow several different RF frequency bands to be used on the same motherboard. The proposed 10.7 MHz IF frequency is compatible with the 1 MHz to 50 MHz input bandwidth of the BasicRX daughterboard. The TDL control output will be generated by the LFTX daughterboard with its DC to 30 MHz input bandwidth. The BasicTX and LFRX daughterboards will be used for diagnostic and development purposes.

The Ettus DBSRX daughterboard is a complete 800 MHz to 2300 MHz receiver, which will allow the USRP board to also meet the RF processing needs of the storage cavity stabilization system described in Section A.4 using the same hardware, techniques and experience. These and related devices may also prove useful for the e-beam stabilization system discussed in Chapter 4.

3.4.3 Analog Frequency Discriminator

The IF frequency is detected with the analog frequency discriminator circuit shown in Figure 3.5. The first stage is a limiter consisting of a high gain, high speed amplifier with a ± 0.5 V clamp on its output. This converts an arbitrary amplitude input signal to a 1 V amplitude square wave, removing any dependence on the input amplitude which may be a result of laser power or alignment stability. The square wave is then low-pass filtered with a cutoff frequency of 16 MHz. The signal is next rectified by a Schottky diode and integrated, providing a DC voltage proportional to the frequency of the input IF signal.

The circuit was calibrated and tested using a Rigol DG3061A arbitrary waveform generator as the signal source. The reference voltage VREF is set to 1.64 V so that the circuit output will be zero at the design frequency of 10.7 MHz while the rectifier is sufficiently biased to provide an output over a ± 5 MHz range. The frequency of an input sine wave was varied from 5 MHz to 18 MHz and the DC output of the discriminator measured. The optimally tuned circuit has a gain of 435 mV MHz^{-1} in the ± 5 MHz range about 10.7 MHz. There is a 5 mV residual RF feedthrough in the DC output, however this will not effect performance as the RF frequency is out of band for the feedback loop.

3.4.4 Analog PI controller

A simple proportional/integral (PI) loop filter is used to provide feedback to the diode laser from the error signal.

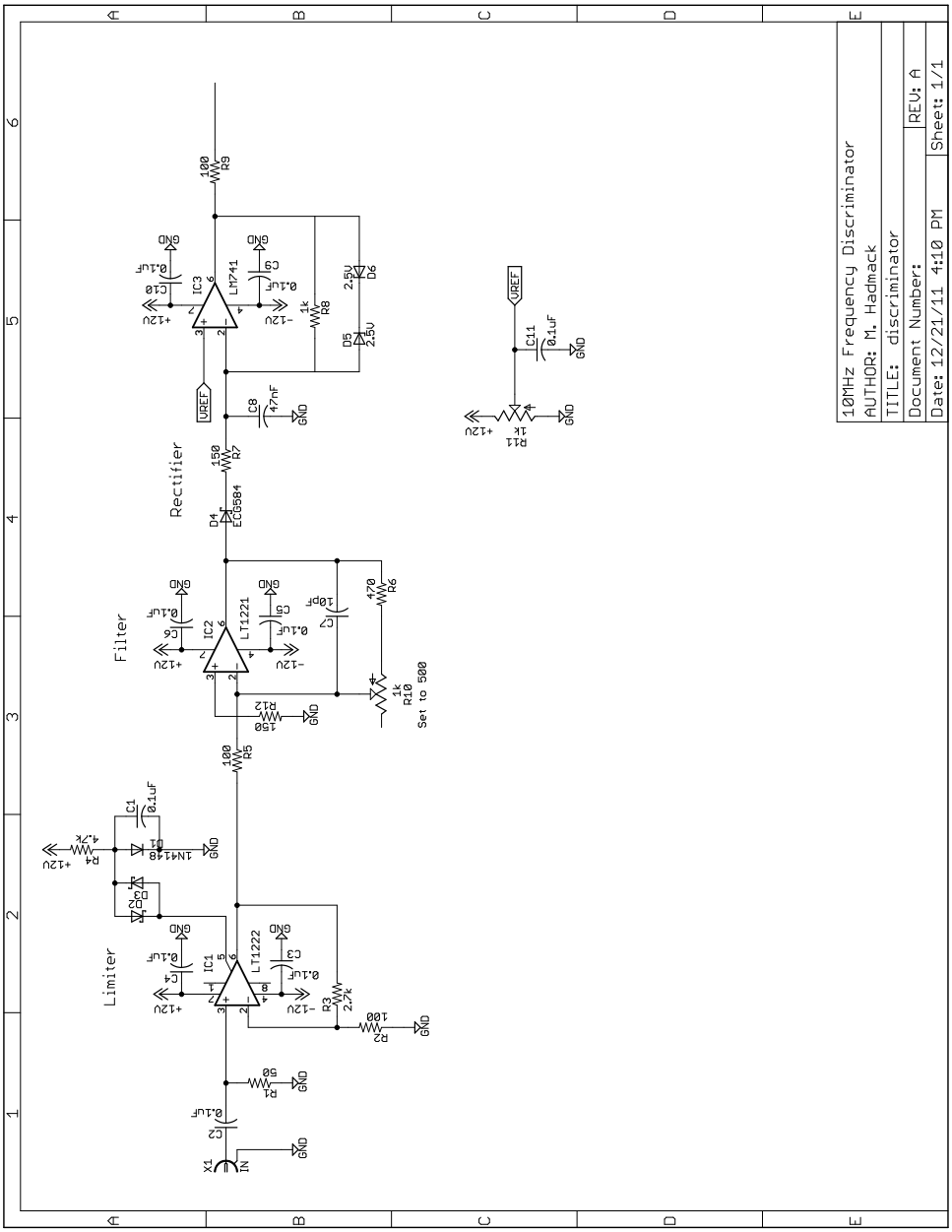

Figure 3.5: The analog frequency discriminator consists of three stages. First, a limiting amplifier (IC1) is used to normalize the input signal level to $\pm 0.5\,\mathrm{V}$. Next, a $16\,\mathrm{MHz}$ cutoff low-pass filter (IC2) is applied to the signal, using its roll-off to convert frequency to amplitude modulation. Finally, the signal is rectified with a Schottky and integrated by IC3.

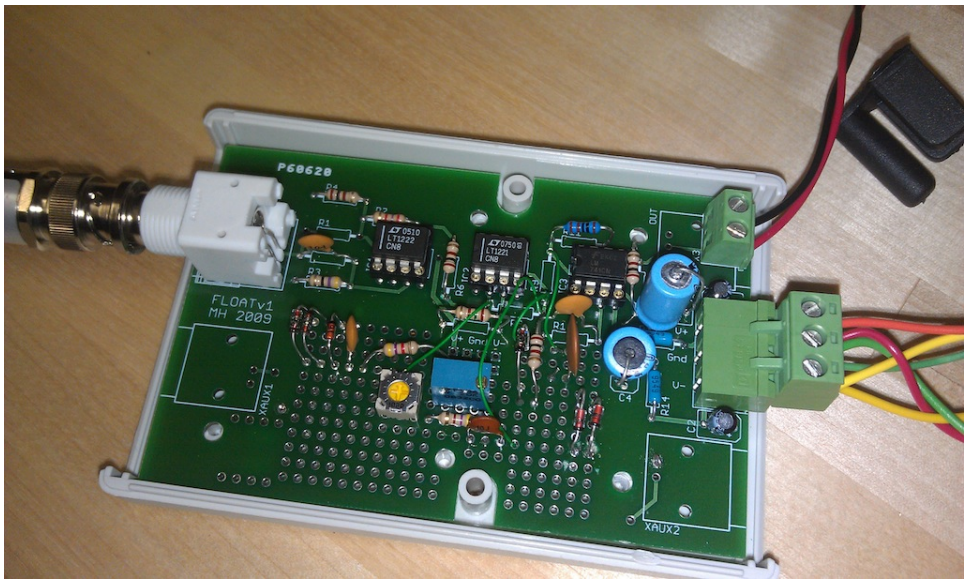

Figure 3.6: The circuit shown in Figure 3.5 is implemented on a FLOATv1 printed circuit board. The FLOATv1 board is a generic PCB developed for permanent assembly of three op-amps in a variety of predefined configurations.

This circuit is primarily intended to track slow drifts in the diode laser frequency relative to the stabilized HeNe. No attempt has been made at this point to compensate for instabilities faster than 100 Hz, but with this system the beat signal will remain stable enough to allow a more thorough analysis of the higher frequency noise sources. This information will be useful in determining the frequency ranges of interest for compensation with a second version of the control circuit.

The PI filter generates the control signal:

$$c(t) = K_P e(t) + K_I \int_0^t e(t)dt \tag{3.1}$$

where $e(t)$ is the error signal. The filter is tuned by varying two parameters; the proportional gain K_P and the integral gain K_I. The tuning parameters for the circuit in Figure 3.7 are computed from the component values:

$$K_p = \frac{R_{15}}{R_{16}} \tag{3.2}$$

$$K_I = \frac{1}{R_8 C_1} \tag{3.3}$$

These parameters were tuned empirically by observing the stability and capture characteristics using the 7L12 spectrum analyzer. The system captures consistently with a wide

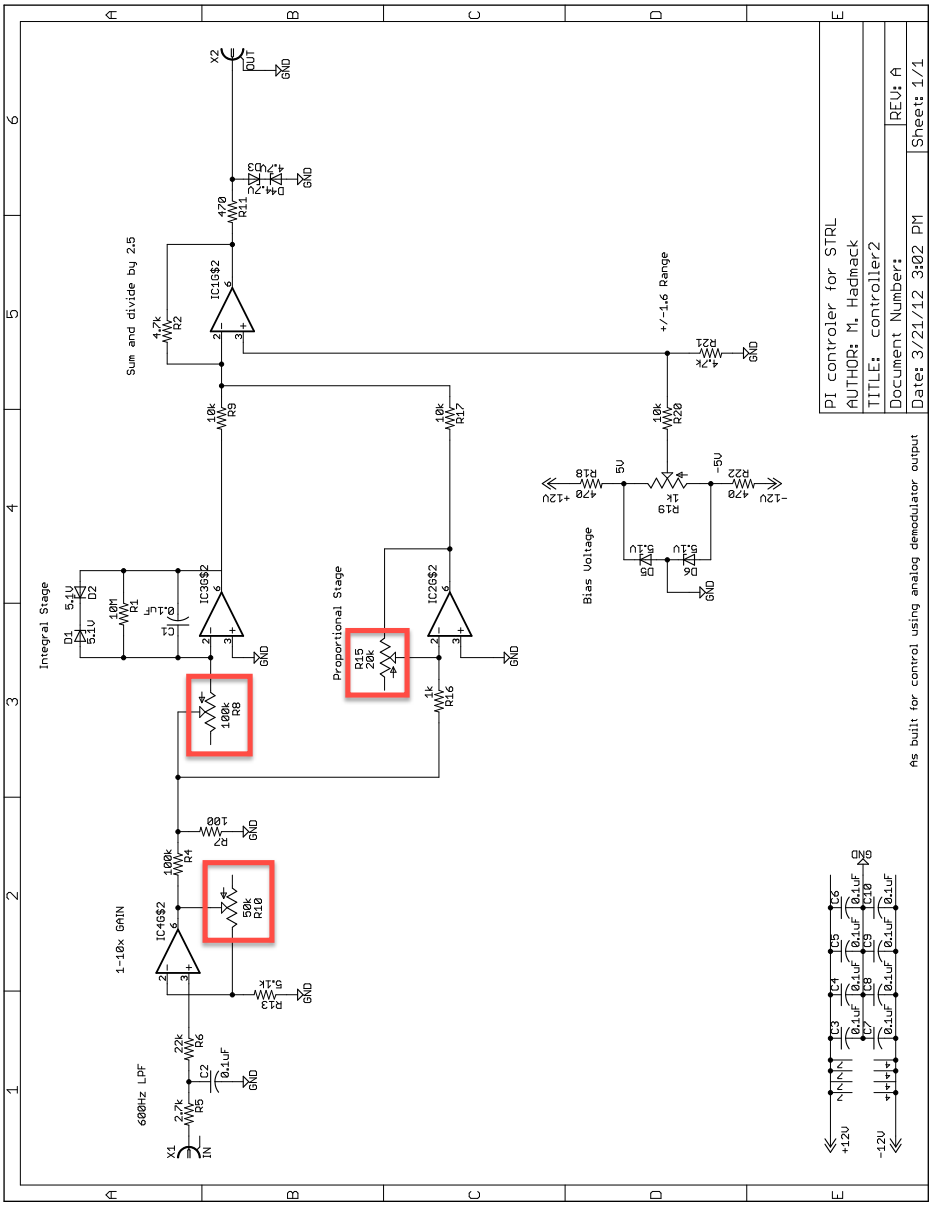

Figure 3.7: A proportional-integral (PI) feedback controller consists of a buffer amplifier followed by parallel linear and integral amplifiers. A summing amplifier combines the outputs of the PI stages and adds a variable offset voltage. The controller is tuned with potentiometers R8, R10, and R15.

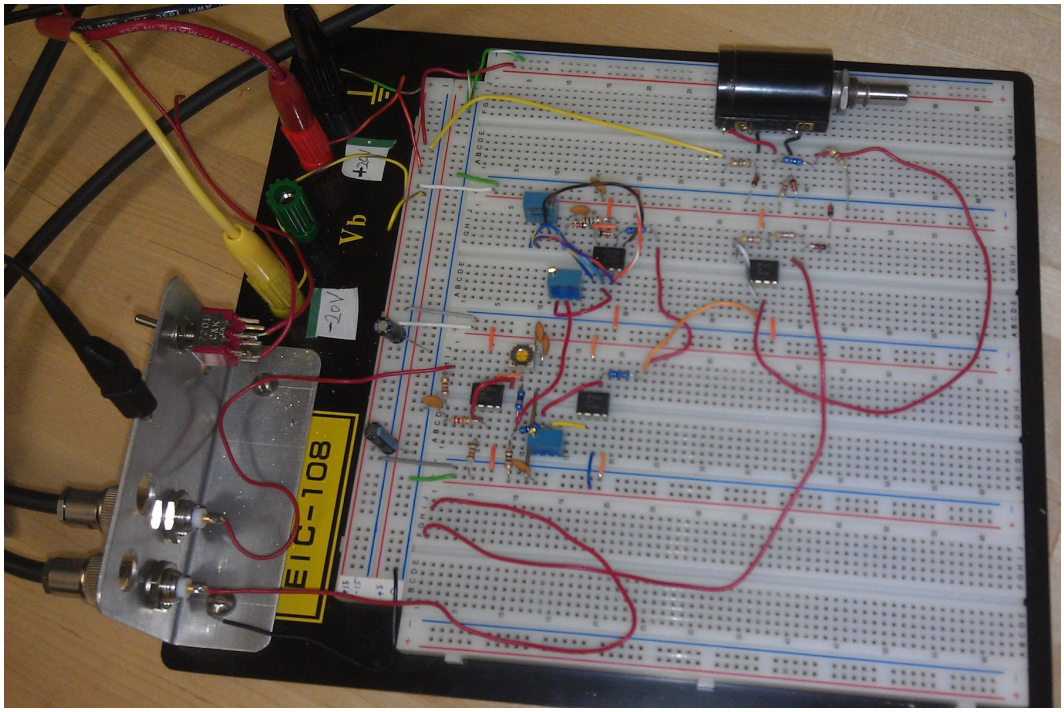

Figure 3.8: The prototype PI control circuit from Figure 3.7 is implemented on a solderless breadboard. A 10-turn potentiometer (at top) is used the achieve fine control of the piezo offset voltage.

range of K_I values, however, any amount of K_p added results in instability. When the value of R_{15} is increased to $200\,\Omega$ ($K_p = 0.2$) or higher while locked, the system begins to oscillate between the two degenerate lock points at $\pm\omega_I$. To remove the oscillatory behavior R_{15} is set to zero to disable the proportional gain entirely. With R8 set to $7.8\,\mathrm{k}\Omega$ the integral gain is $K_I = 1280$. The step response of the circuit is show in Figure 3.9 with a rise time of 220 ms.

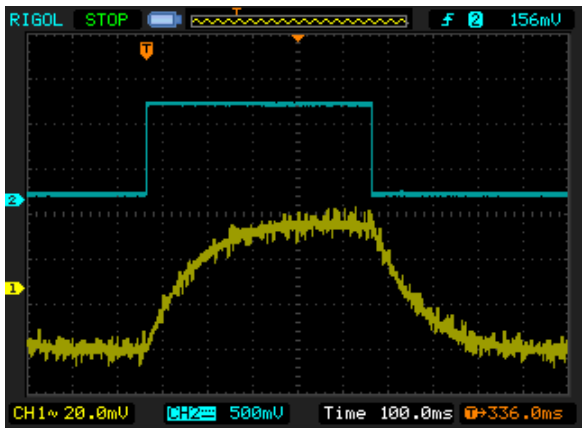

Figure 3.9: The response of the PI control circuit to a step input was captured with a digital oscilloscope. The proportional stage was disabled and the integral amplifier results in a 220 ms time constant.

Due to the oscillations causes by the proportional stage, the tests described in later sections are performed with integral control only. Besides a slow feedback response, another limitation of integral only control, is the tendency of the controller to undershoot the set point due to the long integration time. It was noticed that while the system is stable under lock, the actual RF frequency for which a lock is obtained varies and seems to depend on the rate at which the lock was acquired. This is consistent with the theory for integral controllers although the problem would be eliminated with even a small amount of proportional feedback, to be implemented in future designs.

While the Universal Software Radio Peripheral did not prove useful as an integrated DSP controller for this system, it did serve as an invaluable diagnostic tool. Using the stock FPGA firmware and the GNU Radio software environment, a wide-band FM radio receiver was implemented. This receiver allows any amount of demodulated laser frequency vs. time data to be recorded on a PC for offline analysis.

Although the USRP sample rate is 64 MS/s, the actual recordable data rate is limited by the USB interface to 8 MS/s. Even with the maximum USB data rate the system is subject to occasional buffer underruns and overflows so the USRP is programmed to use an internal 10x decimation rate to reduce the sample rate to 6.4 MS/s before transmission to the PC over USB. The PC has been able to stream data to a file at 6.4 MS/s indefinitely, however with 64 bit samples this rate consumes 51.2 MB s^{-1} of disk space. For the purpose of stability analysis, data files are typically recorded for 5 s, corresponding to 32 MSamples or 256 MB data files.

Under lock the IF signal has an observed bandwidth of about 4 MHz on the spectrum analyzer. At 6.4 MS/s the Nyquist frequency of 3.2 MHz is the maximum frequency deviation that can be measured. The decimation filter applied by the USRP includes an anti-aliasing filter to remove ambiguous frequency components above the Nyquist frequency. If the USRP is tuned close to the nominal IF frequency then its ± 2 MHz excursions fit within the sampling bandwidth but not with much room to spare.

The IF frequency deviations can be extracted from the sampled data by digital frequency demodulation. Since the USRP data consists of a complex signal with in-phase and quadrature components, demodulation is straightforward. For a complex signal $A(t) = I(t) + iQ(t) = \cos(\varphi(t) + i\sin(\varphi(t)))$ the phase is simply computed as $\varphi(t) = \arctan(I/Q) = \arg(A)$. Discontinuities in phase at $\pm\pi$ are removed using the phase unwrap algorithm provided by the `numpy` numerical toolkit for Python[42]. Furthermore, the frequency can be estimated as the single sample derivative of the phase:

$$f_i = \frac{\varphi_i - \varphi_{i-1}}{2\pi dt} \tag{3.4}$$

where $dt = 1/f_s$ is the sample interval and i is the sample index.

At this point the data rate can again be reduced by a decimation filter. This time a 32x decimation is used to reduce the sample rate from 6.4 MS/s to 200 kS/s resulting in more manageable data files, 32 times smaller in size.

The data collection and demodulation system performance was tested using data sampled from the HP8648C signal generator. The signal generator was tuned to 15.1 MHz and a frequency modulation 200 kHz deep at a rate of 1 kHz was applied. The USRP was tuned to 15 MHz and 32 Msamples were collected over five seconds. Figure 3.10 shows that the demodulation produces the exact frequency, amplitude, and offset as programmed into

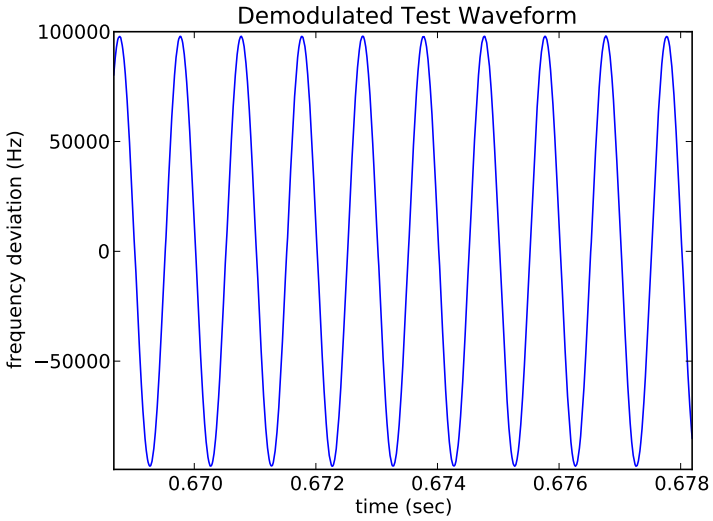

Figure 3.10: A test signal at 15.1 MHz with a 1 kHz frequency modulation was acquired by the USRP board tuned to 15 MHz. A 10 ms window of the demodulated data shows that the modulation waveform is perfectly reconstructed.

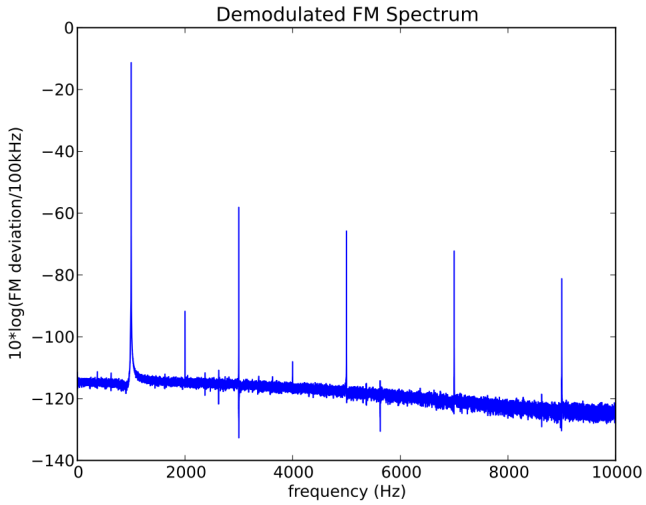

Figure 3.11: The spectrum of the time domain test data plotted in Figure 3.10 is computed using the fast fourier transform (FFT). This spectrum contains the expected large component at 1 kHz along with its higher harmonics with at least 50 dB less power.

the test source. Figure 3.11 shows the fast Fourier transform (FFT) of the demodulated data containing a single frequency component at 1 kHz, plus its harmonics.

3.5 System Tests

With the system locked as described above the USRP was used to analyze the system performance. The actual IF signal frequency under lock is measured with a Tektronics 7L12 spectrum analyzer to be approximately 13 MHz. The USRP was configured for a center frequency of 13 MHz and to collect 1 Msamples at 200 kS/s for a total sample window of 5 s. This data was collected during an interval in which the system maintained lock for more than 80 min. Figure 3.12 shows the FFT of the demodulated beat signal over the data duration. Repeated measurements produced essentially identical spectra with some variation in the amplitudes of various peaks. The noise is clearly dominated by a peak at 2.285 kHz, which is 9 Hz wide FWHM. There are also two other significant noise components at 2.222 kHz and 1.587 kHz, where are each less than 3 Hz wide. The cause of these oscillations in the laser frequency have not been identified, though given the acoustic frequencies, are likely due to mechanical noise in the building, probably air conditioning. It is also possible that there is a not yet identified source of electrical noise in the tunable diode laser controller unit. Figure 3.13 is an oscilloscope capture of the analog frequency demodulator output that clearly shows the 2.285 kHz modulation.

Figure 3.14 shows the spectrum of the beat frequency spectrum as viewed on the Tektronics 7L12 spectrum analyzer. While the system is able to maintain lock for over an hour at a time without operator intervention, it is certainly the 2.285 kHz noise source that is responsible for the observed 5 MHz wide RF spectrum. In fact the raw demodulated USRP data is dominated by a 2.285 kHz waveform of 3 MHz depth.

It should be possible to compensate for most of the low frequency noise by increasing the bandwidth of the PI control circuit. The 3.5 kHz frequency modulation bandwidth of the TDL is still the limiting factor in system performance. The 2.285 kHz noise is so significant to the system performance that an effort must be made to identify and eliminate the source of this interference. The other cavity stabilization systems described in previous chapters are dependent on the STRL as a stable frequency reference. Therefore system noise must be reduced to a minimum, so that the errors do not propagate into other dependent system.

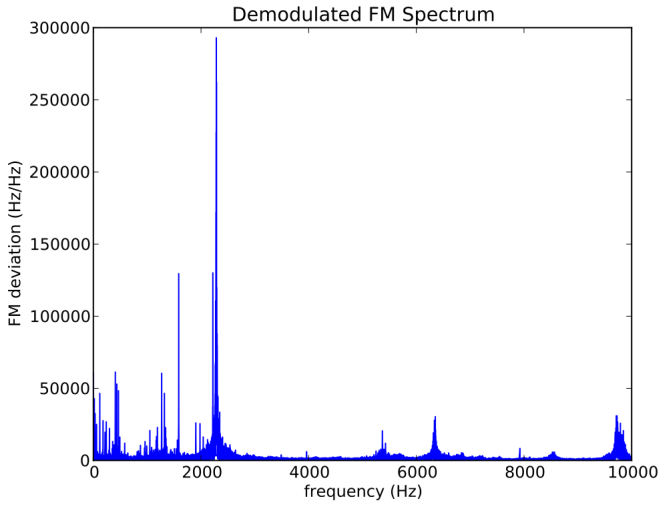

Figure 3.12: The noise spectrum of the STRL system is the FFT of data acquired while the system was locked and stable for over 80 minutes. The dominant noise component is the peak at 2.285 kHz, for which the source is unknown.

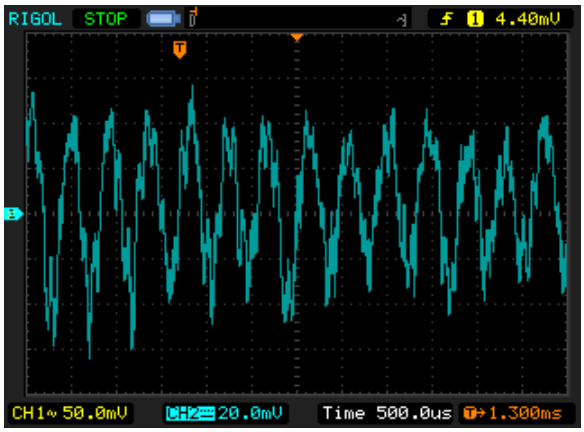

Figure 3.13: While under lock, the analog demodulator output contains a dominant frequency modulation noise component at 2.285 kHz.

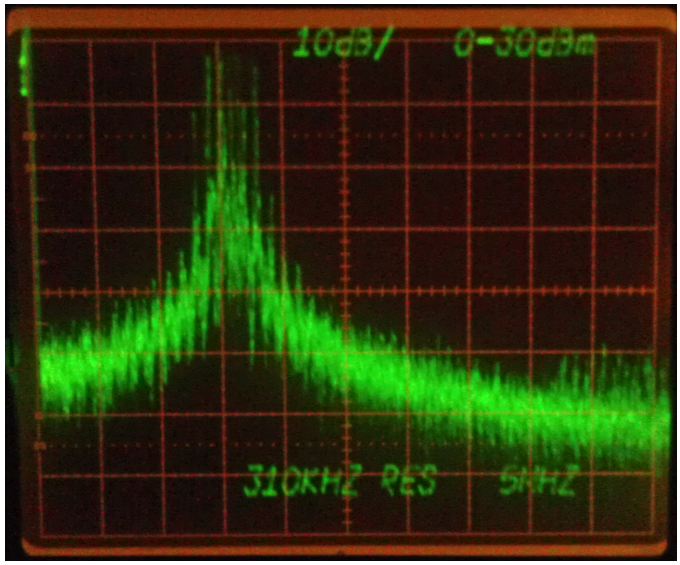

Figure 3.14: The laser beat signal spectrum is observed using the 7L12 spectrum analyzer. The instantaneous width of the peak appears to be much narrower than the 5 MHz shown, but is presumably broadened by the 2.285 kHz FM noise component.

The frequency tuning performance of the STRL was tested by tuning the HP8648C local oscillator frequency while the system was under lock. The system was able to track discrete variations in LO frequency of 1 MHz without losing lock. While tuning the LO continuously from 826 MHz to 947 MHz, the output of the control circuit varied by 120 mV for an overall DC loop gain of $1\,\mathrm{mV\,mHz^{-1}}$ which is consistent with the measured tuning rate of the TDL. The ± 2 V output range of the control circuit would allow the laser to track beat frequencies over a 4 GHz range if not for limitations of the RF components described in an earlier section.

3.6 Conclusion and Future Work

A stabilized tunable reference laser has been developed for free-electron laser resonator tuning and stabilization applications. The present system has a tunability of 3.4 GHz and is constructed of entirely off-the-shelf components. While the technology is basically functional, many future improvements can be made. A custom engineered integrated system could reduce the entire system from its present $900\,\mathrm{in}^2$ layout to a monolithic assembly occupying less than $40\,\mathrm{in}^2$. Much of the observed instability is attributable to the Newfocus

tunable diode laser itself. This laser was one of few tunable diode lasers available on the market at the time of purchase, but is not suitable for RF opto-electronic systems despite its 150 GHz potential tuning range. A slight bump of the optical table sometimes results in changes in laser frequency and high frequency impulses in excess of 100 MHz that are difficult to compensate with feedback due to the controller's 3.5 kHz tuning bandwidth. Many compact Littrow type grating tuned diode laser designs can be found in the literature which would be suitable for this system due to their mechanical robustness, high tuning bandwidths, and high powers[43].

Overall stability can also be improved with an alternate reference source. The dual-mode stabilized HeNe laser with its 1 MHz linewidth is an appropriate reference source for the FEL control applications described. However, using a HeNe or diode laser locked to an atomic reference line could in principle reduce the line-width of the STRL to sub-Hz levels if required for precision spectroscopic applications while maintaining wide and well controlled tunability.

The RF tuning bandwidth of the system is presently limited to 3.4 GHz by the HP8648C signal source. Introduction of an RF pre-scaler, as described in a prior section, should be able to increase this range by 2x or 4x. The tuning range will still be limited to the 9 GHz bandwidth of the photodiode and gain circuitry. By exploiting the state of the art in high speed photodetector and broadband microwave electronics this maximum range can probably be at least double, but at much greater expense.

Finally, a complete conversion of the control system to a digital signal processing solution would greatly improve the reliability and utility of the system. A software defined radio (SDR) system would allow the RF front-end to be instantly reconfigured for alternate operating and diagnostic modes. A digital version of the feedback controller can be easily and repeatably programmed from a computer and can be optimized by automated algorithms not possible with an analog controller. Analog electronics are also subject to thermal drifts and component aging, which pose far less of a problem in digital electronics. The use of the USRP in this system has shown that SDR is useful as a wide-band FM receiver used only for system diagnostics. A more modern SDR hardware platform would provide an FPGA with the hardware resources and software tools required to perform the digital signal processing that was unsuccessful with the USRP board.

This project has successfully demonstrated a stable tunable reference laser (STRL) for use as a wavelength reference for the optical storage cavity and its free electron laser

pump. With the FEL and storage cavity resonators dynamically locked to the same reference laser, both cavities can be synchronously and precisely tuned by varying the frequency only the local oscillator for the STRL system. This will enable rapid and precise tuning of the x-ray photon energy without loss of x-ray flux or brightness or the need to manually resynchronize the optical cavities.

Chapter 4

e-Beam Phase Stabilization

4.1 Introduction

A critical factor in the performance of the free electron laser and the x-ray source is the amplitude and phase uniformity of the high-power RF pulses used to drive the microwave gun and linac. Irregularities in the phase of the RF waveform result in variations in the timing between the electron micro-pulses that drive amplification in the laser cavity. The laser is tuned by selecting a cavity length that synchronizes the arrival time of circulating optical micro-pulses with the arrival of new electron pulses from the accelerator and transport system. For example, only a 1.03° phase excursion at 2856 MHz results in an electron bunch delayed by 1 ps, which is the entire nominal pulse length. De-synchronization of the incident micro-pulse timing from the cavity resonant timing results in depressed laser gain and reduced laser power.

This micro-pulse synchronization is of particular importance for the optical storage cavity. Incoming electron micro-pulses must by synchronized to the circulation timing of laser pulses in the optical storage cavity. Any loss of beam synchronism in the interaction region will lead to reduced x-ray flux. Additionally, the FEL must produce micro-pulses with a fixed RF frequency, since the length of the optical storage cavity is locked to the RF master oscillator.

A high power ITT Triton 2960 klystron is used to power the MkV FEL Linac; it amplifies low noise microwave pulses to the 30 MW power level required for the acceleration of a relativistic electron beam. The accelerating potential of the klystron amplifier is responsible for the device's gain and takes the form of a 300 kV pulse. Uniformity of the klystron gain requires careful regulation of the pulse amplitude over its $\sim 8\,\mu$s duration.

A high voltage DC potential applied to the klystron discharges through activation of a hydrogen thyratron switch via an LC resonant pulse forming network (PFN). Tuning the poles and zeros of the PFN circuit allows the high voltage impulse through the thyratron to be regulated to include a flat-topped region, suitable for uniform amplification of the RF pulse over some interval. The "flat top" interval and quality of regulation are limited by the number of poles and zeroes in the PFN circuit. Additionally, the complex gain of the klystron is affected by the time-dependence of the high voltage applied through the PFN, so the tuning procedure must be carried out based on the shape of the RF pulse waveform post-amplification. This procedure is typically performed at low RF powers and PFN voltages, and is only an approximation of the performance to be realized at full power. Typically, only the amplitude of the RF pulse is optimized with this tuning procedure, while realistically a phase shift of several degrees is still present over the output RF pulse duration.

Further optimization of the RF pulse amplitude and phase could be achieved (and has been) by increasing the number of degrees of freedom in the PFN filter. Tuning, however, is still a cumbersome and dangerous procedure. The existing Mk3 PFN consists of many high voltage inductors and capacitors submerged in a large tank of dielectric oil and is unable to accommodate any further filter complexity within the present design.

Another approach to this regulation problem is the use of active feedback to provide a correction signal to either the high voltage pulse or input RF pulse. The most straightforward approach is to regulate the amplitude and phase of the input RF signal to compensate for any non-uniformity in the complex transfer function of the klystron. Such a feedback loop requires fast measurement of the amplitude and/or phase of the high power RF output and a means to feed this signal back to an amplitude/phase modulator on the RF source. Unfortunately, the long distances between components in the lab leads to latencies and long phase delays (hundreds of ns). These effects make a high bandwidth and stable feedback loop impractical in this system.

Alternatively, given the good pulse to pulse repeatability of the high power RF system, and slow drift in the amplitude and phase perturbations observed in the output RF pulse, a feed-forward compensation scheme can be applied. This correction is not applied in real time to each pulse, but rather, is applied to subsequent pulses. The RF pulse amplitude and phase are measured and the data used to compute a correction waveform. Using an arbitrary waveform generator, the correction is applied to amplitude/phase modulators

operating on the input RF pulse. Subsequent measurements of the amplitude and phase show the compensated high power RF pulse and allow iterative correction of any residual error.

Not only can the amplitude/phase of the RF pulse be normalized to remove the ripples observed in the RF and electron beam systems, but also the pulse amplitude and phase can be sculpted to custom waveforms that may optimize the performance of the free electron laser and optical storage cavity-based x-ray source.

4.2 Laser Performance

The free spectral range of the MkV free electron laser is, by design, 1/39th of the electron beam RF frequency. In order to maintain resonant operation and high gain the 39th incoming electron pulse must be timed such that it overlaps with the return of the 1st optical pulse to the start of the undulator, and so on. Free-electron laser simulations have demonstrated that a 0.25° phase modulation (240 fs), applied to the electron beam, has a negligible effect on the laser gain and pulse energy[44].

4.3 Direct Conversion Microwave Receiver

The phase and amplitude of the RF waveform to be corrected are reconstructed using direct quadrature demodulation (IQ demodulation). The received RF signal is written as $V_{\mathrm{S}}^{\mathrm{I}}(t) = A(t)\cos(\omega t + \varphi(t))$, where A(t) and φ(t) are the amplitude and phase modulation components and $\omega = 2\pi(2.856\,\mathrm{GHz})$ is the RF carrier frequency. Half of this signal is to be delayed in phase by 90°, giving $V_{\mathrm{S}}^{\mathrm{Q}} = A(t)\sin(\omega t + \varphi(t))$.

When these two signals are then mixed (multiplied) with an unmodulated reference signal $V_R = \cos(\omega t)$ and then sent through a low-pass filter, the in-phase and quadrature signals are obtained:

$$I(t) = V_R V_S = A(t)\cos(\omega t)\cos(\omega t + \varphi(t)) = \frac{A}{2}\cos(\varphi(t)) \tag{4.1}$$

$$Q(t) = V_R V_S^* = A(t)\cos(\omega t)\sin(\omega t + \varphi(t)) = \frac{A}{2}\sin(\varphi(t)) \tag{4.2}$$

Now the amplitude and phase are easily reconstructed by:

$$A(t) = 2\sqrt{I^2 + Q^2} \tag{4.3}$$

$$\varphi(t) = \arctan(\frac{Q}{I}) \tag{4.4}$$

Another convenient representation for digital signal processing is as a complex signal:

$$\tilde{A}(t) = 2(I + iQ) = A(t)e^{i\varphi(t)} \tag{4.5}$$

4.4 Stabilization System Design

4.4.1 RF System Components

This section describes the components of the system block diagram shown in Figure 4.1. This system has a feed-forward bandwidth of about 3 MHz, which is limited by the compensation phase modulator. However, the overall system bandwidth is limited by the high power ITT klystron to approximately 1 MHz.

- Gain Control Digital Attenuator: A Hittite Microwave digital attenuator provides up to 31 dB attenuation for calibration of input signal amplitude.

- Calibration Phase Shifter: A SLAC-designed voltage controlled phase shifter is used to control the absolute phase of the input signal so that the peak amplitude of the Inphase and Quadrature signals are available for system calibration. This device can provide a 180° phase shift for a 10 V input signal with a modulation bandwidth of 3 MHz.

- Power Monitor Diode: An RF diode detector provides a calibrated power measurement of 6.7 mV dB^{-1}. It is used in conjunction with the digital attenuator to keep the mixer input levels below the 1 dB compression point, so that the conversion is linear.

- Computer Control Interface: An Arduino microcontroller board provides USB control of the digital attenuator and also the calibration phase shifter by way of an external 16-bit DAC.

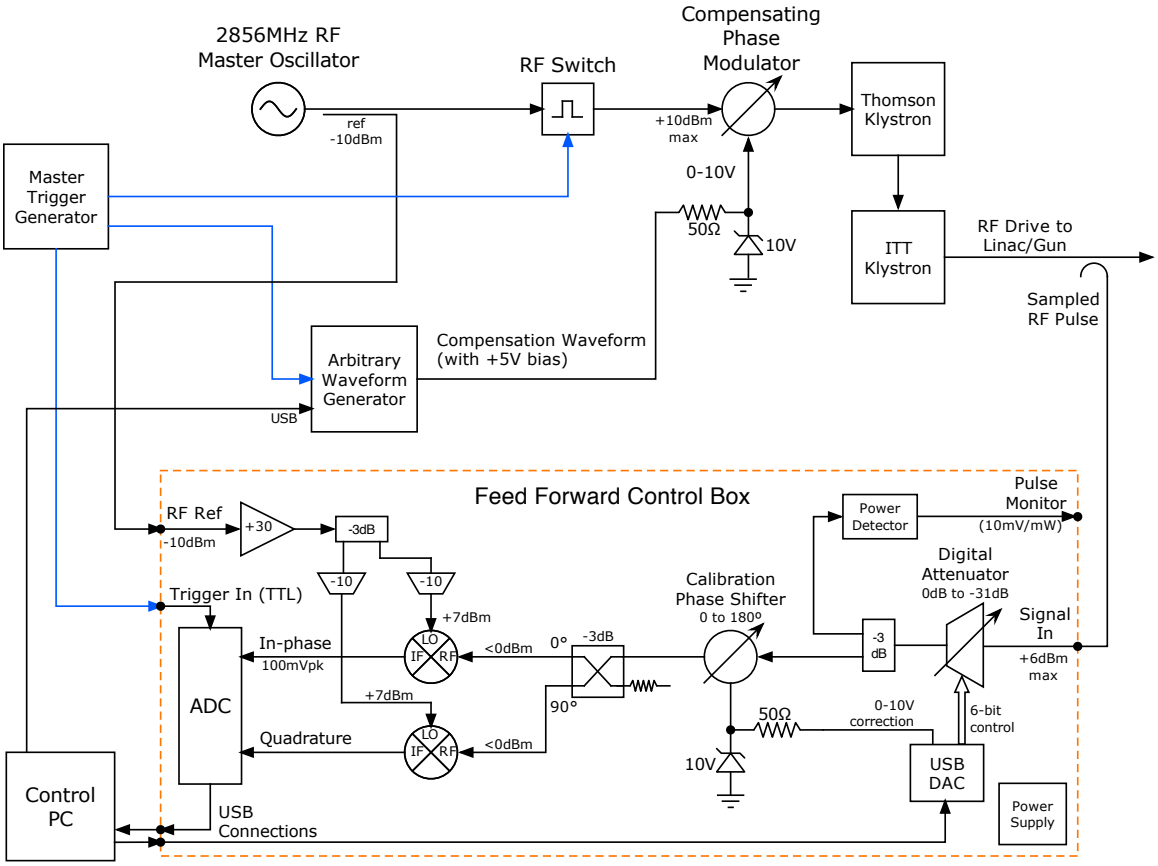

Figure 4.1: The MkV RF signal chain consists of a low-noise microwave master oscillator followed by modulator and amplifier systems. The high-power RF drive to the linac is sampled and measured by the Feed-Forward Control Box. The control box takes an arbitrary 2856 MHz signal as its input and applied appropriate attenuation and phase shifts such that the signal can be mixed with the system master oscillator. The mixer outputs are the in-phase and quadrature components of the microwave signal which is then sampled by a control computer. The control PC computes a compensation waveform that corrects the RF phase via an arbitrary waveform generator.

- Quadrature hybrid splitter: The RF signal is divided into two components of equal amplitude with a 90° relative phase shift between them. The Mini-circuits ZX10Q-2-34-S+ guarantees an amplitude imbalance less than 0.52 dB and a phase imbalance less than 0.28°.

- Double balanced mixers: Mini-circuits ZEM-4300+ are used as phase detectors when input signals of equal frequency are supplied to the RF and LO ports. The output is proportional to $\cos(\varphi)$ where φ is the phase difference between RF and LO.

- Phase reference amplifier and 0° splitter: The MkV RF drive system provides 0 dBm while the Mixers each require a 7 dBm LO signal. A Mini-circuits ZHL-1042J power amplifier and attenuators are used in conjunction with a Mini-circuits ZX10-2-42-S+ 0° power splitter.

- Digital oscilloscope: A Rigol DS1102E 100 MHz bandwidth oscilloscope serves as the system ADC and is used to capture 500 samples over 6 µs (a 12 ns sample interval). The in-phase and quadrature signals are digitized by the two oscilloscope channels and the data is read from the control computer via a USB connection.

- Arbitrary waveform generator: A Berkley Nucleonics Model 645 AWG is used to drive the compensation phase shifter and complete the feedforward loop. The AWG has a 10 MHz output bandwidth. The 14-bit compensation data is sent to the device from the control computer over a USB connection.

- Compensating Phase Modulator: A second SLAC voltage controlled phase shifter is used to apply the feed-forward compensation waveform from the AWG to the master oscillator output. This device provides a 180° phase shift for a 10 V input signal with a modulation bandwidth of 3 MHz.

4.5 Phase Measurement Error

The precision with which the RF phase can be measured is primarily limited by quantization error in the oscilloscope's ADCs. The Rigol DS1102E oscilloscope samples the I and Q signals with an effective 7-bit resolution for a dynamic range of $\frac{\delta I}{I} = 2^{-7} = 0.008$ resulting in an LSB noise of 0.9 mV for a 120 mV full scale signal. It is assumed that I and Q will always be sampled with the same precision such that $|\delta I| = |\delta Q|$.

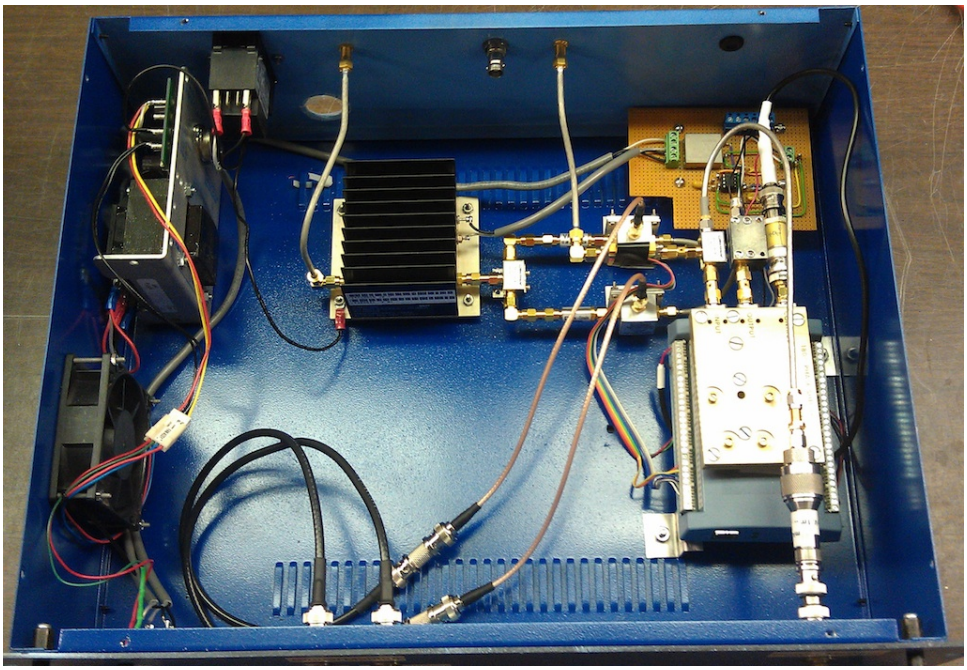

(a)

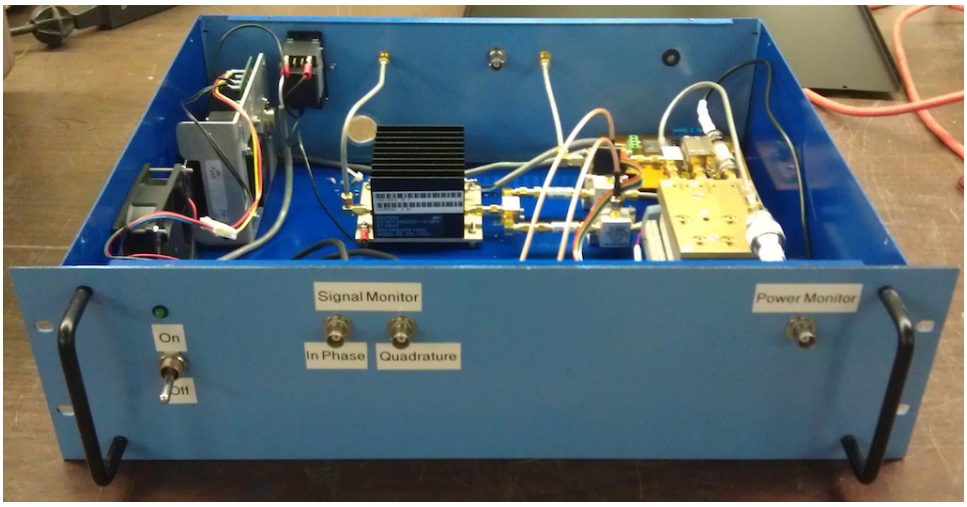

(b)

Figure 4.2: The feedforward control chassis contains the components drawn within the dashed border in Figure 4.1. The system is enclosed in a standard 19" 3U rack mount chassis with the input connectors located on the back panel and the outputs on the front panel.

When the system is adjusted such that the quadrature signal is minimized, the nominal measured phase (in the absence of any errors or modulation) is zero. For small values of Q and φ

$$\varphi = \arctan(\frac{Q}{I}) \simeq \frac{Q}{I} \tag{4.1}$$

Since $Q \ll I$, the fractional uncertainty $\frac{\delta Q}{Q}$ dominates over $\frac{\delta I}{I}$ so that

$$\frac{\delta\varphi}{\varphi} = \frac{\delta Q}{Q} \tag{4.2}$$

The absolute phase uncertainty can then be found

$$\delta\varphi = \varphi\frac{\delta Q}{Q} = \frac{\delta Q}{I} \simeq \frac{\delta I}{I} \tag{4.3}$$

When using 7-bit sampling, this results in a phase uncertainty $\delta\varphi = 0.46°$. This result, however, only accounts for random quantization error and not for other systematic error that is most likely present in the data. Clearly, though, future efforts to increase the phase stability would benefit from the use of a higher resolution digitization instrument.

It is also possible to operate with the system such that the quadrature and in-phase signals are equal in amplitude so that the nominal measured phase is 45°. The uncertainty in this configuration can be similarly derived except that now the uncertainty in I cannot be neglected, adding an additional factor of $\sqrt{2}$ to the result. The Taylor series for arctan, when expanded about unity, also contains an additional factor of $\frac{1}{2}$. Overall, the net uncertainty in the 45° configuration is reduced by an insignificant factor of $\sqrt{2}/2(= 0.71)$ to $\delta\varphi = 0.16°$.

There is a small amount of error due to variations in the DC offsets and gain experienced by the I and Q signals. Calibration factors applied by software minimize the effect of these errors. Failure to calibrate the system has typically resulted in DC offsets in I and Q on the order of 1 mV and mismatch in the peak amplitudes of I and Q of 1 %. These static systematic errors result in an error in the absolute phase measured of up to 0.3° but only contributes a 1 % error to the relative phase measurement used for compensation.

4.6 Software

The system is controlled from a PC running Linux in the FEL control room. The instrumentation is directly connected to the PC via USB cables. The control software is written in the Python programming language with a graphical user interface (GUI) utilizing the wxPython[45], and Matplotlib[1] toolkits. The oscilloscopes and arbitrary waveform

generator are both compliant with the USBtmc interface standard, which allows for familiar GPIB style control via a modern USB connection.

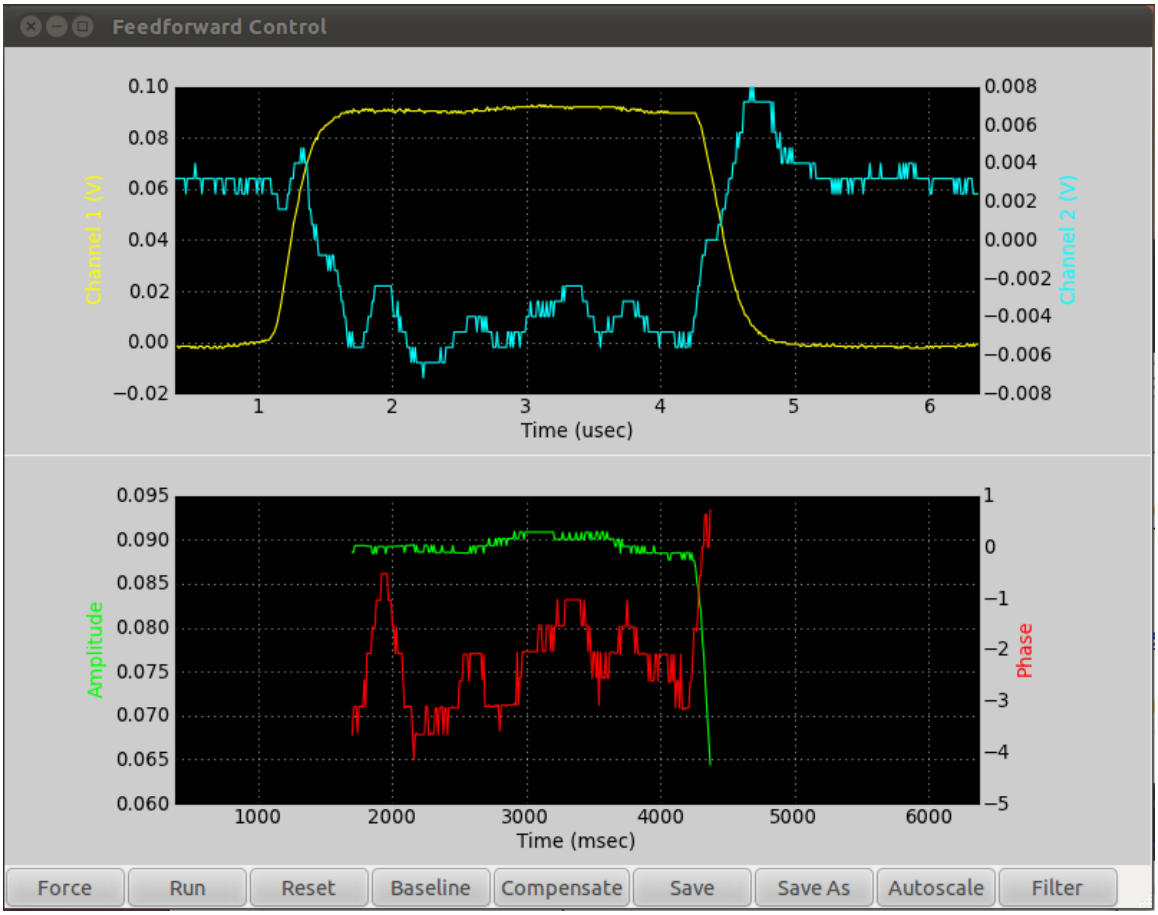

Figure 4.3: The graphical user interface for the Feedfoward system is implemented in wxPython[45] running on Linux. The upper plot shows the raw sampled in-phase and quadrature signals, while the bottom plot shows the reconstructed amplitude and phase. System commands are issued using the buttons at the bottom of the window.

The control software uses a modular design to facilitate future maintenance and upgrades. A graphical user interface (GUI) provides a user friendly subset of commands for day-to-day use of the system. A command line interface (CLI) provides more comprehensive access to all system functionality. The CLI allows scripts to automated common measurement tasks (such as before and after performance comparisons). These high-level interfaces are based on a low-level software module that provides programatic control over

all functions of the system. Additional command line programs allow for offline analysis of captured data.

4.7 System Tests

4.7.1 Calibration

Mismatch between the in-phase and quadrature RF paths may result in DC offsets or gain errors in the signals sampled by the oscilloscope. These errors may be due to mismatch of the double balanced mixers, oscilloscope calibration errors, or mismatch in any of the other RF components of the nominally identical I and Q signal paths. The effect of a calibration error as described in Section 4.5 may be negligible but can be minimized by applying software calibration factors to the sampled data, such as described in the following procedure

1. Adjust the calibration phase shifter to maximize the amplitude of the in-phase signal on oscilloscope channel 1.

2. Adjust the digital attenuator and oscilloscope gain to maximize the dynamic range of the sampled data. Typically an oscilloscope scale of 20 mV/div is chosen with a peak in-phase amplitude of 100 mV. Record the peak and baseline voltages.

3. Adjust the calibration phase shifter to maximize the amplitude of the quadrature signal on oscilloscope channel 2. Record the peak and baseline voltages.

The software then uses the offset voltages and the ratio of the peak voltages to correct and normalize the sampled data before the amplitude and phase are reconstructed.

Compensation of the RF phase requires knowledge of the loop gain and delays. Both may be measured by programming the arbitrary waveform generator with a short pulse of given amplitude and time delay. When the RF phase is measured and reconstructed the amplitude and time offset of the resulting phase pulse are used to set the system gain and delay. Because of the finite bandwidth of the klystron, the pulse has a much longer rise time, which makes identification of the delay difficult. As long as the pulse is long enough to reach its peak amplitude with a flat top the loop gain can be measured precisely. The measured loop gain of $18.0\,^{\circ}\,\mathrm{V}^{-1}$ is in very close agreement with the specification of 180° per 10 V provided with the SLAC voltage controlled phase shifter. The time delay, however,

is due to cable delays and thus depends on which source is to be used for compensation. Fine tuning of the delay must be performed for each source configuration.

The digital oscilloscope is configured to perform an 8 sample average of the I and Q waveforms. Instabilities in the form of 2° to 3° absolute phase jumps from one macro-pulse to the next were observed in the phase measured from the un-averaged waveforms. These jumps in phase are likely caused by plasma instability in the PFN discharge thyratron. These phase offset errors do not affect the structure of the measured phase; they only produce a random offset from shot to shot. A simple multi-sample average eliminates the phase instability in the reconstructed phase. The instabilities in the thyratron discharge result in a change in impedance and thus, the peak voltage applied to the high power klystron causes the gain and phase to vary slightly. While these changes in RF power cause variations in e-beam energy and thus result in laser instability, at least a net absolute phase shift has no effect on laser performance and the ripple is still effectively removed.

4.7.2 Time Shift Invariance

The dependance of the ITT klystron gain on a transient high voltage pulse raised the possibility that the impulse response of high power RF system may not provide time shift invariance. To check this, the arbitrary waveform generator was used to generate phase pulses at three different times within the RF macro-pulse. Figure 4.4 shows the measured phase response to the identical phase modulation pulses with varying delays and sign. When the background phase is subtracted it is clear that all six pulses are nearly identical in Figure 4.5. The maximum observed variation in phase is 0.6° and 60 ns wide. Both are consistent with measurement error for the system. Therefore, for the purpose of phase and amplitude compensation, the klystron transfer function is considered time invariant.

This result greatly simplified the requirements for further development of the phase compensation system. Only a single, time-invariant kernel needs to be used to deconvolve the required phase correction from the measured phase data.

4.7.3 Phase Compensation

This system allows the compensation of the RF phase based on an RF measurement made at any point in the accelerator system. For example, a the RF waveform sampled at the linac feed point may be used to derive a feedforward compensation correcting the waveform at this point. Ultimately, it is the phase of the actual electron bunches that must

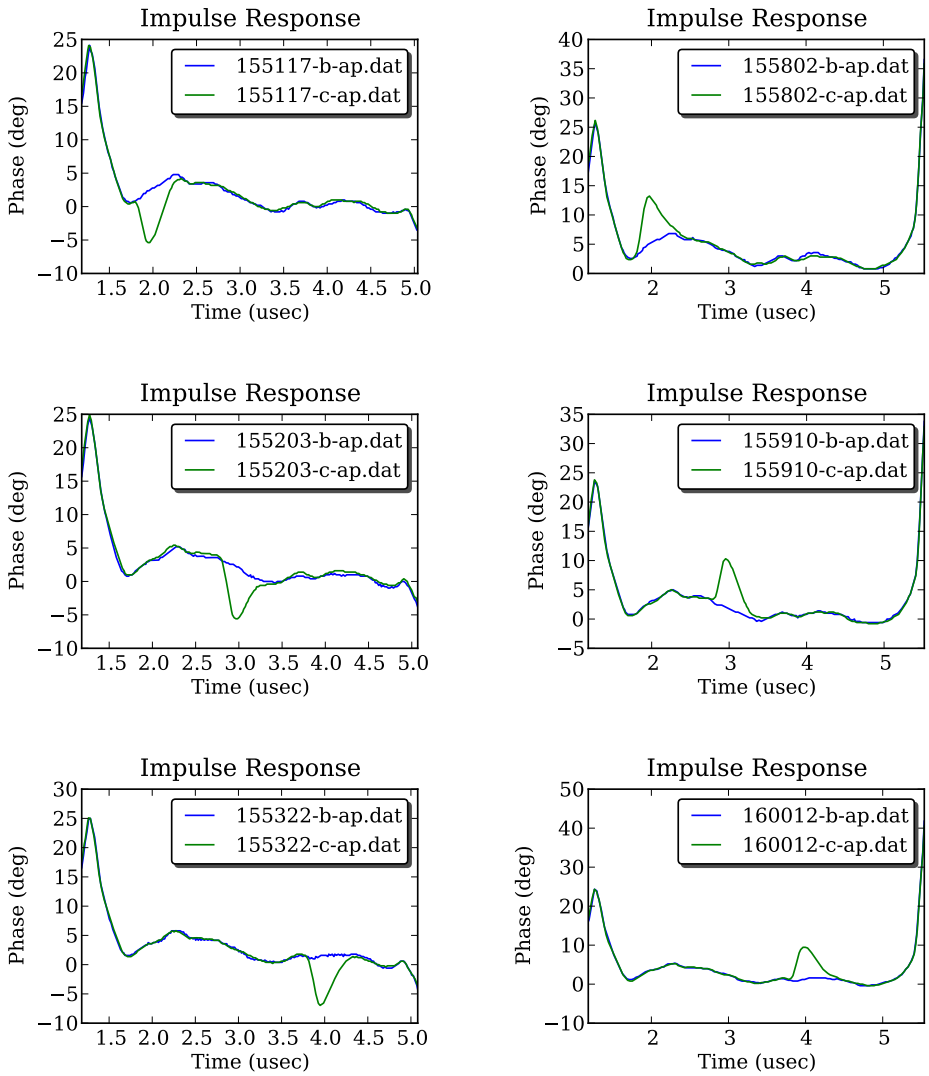

Figure 4.4: The impulse response of the RF system was measured for 200 ns impulses for both polarities and various delays. These plots show the reconstructed RF phase with and without each of the impulses.

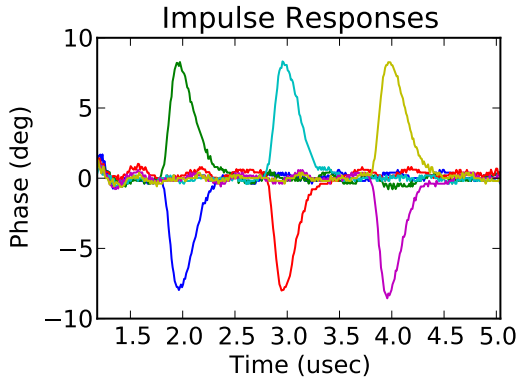

Figure 4.5: Each of the impulses shown is the result of subtracting an impulse from Figure 4.4 from its corresponding background. Clearly the impulses responses only differ in the delay and polarity imposed.

be compensated, so the signal from one of several beam position monitors will be sampled and corrected. Strip-line beam position monitors (BPMs) along the beam-line output a signal proportional to electron beam current and have sufficient bandwidth to resolve the 2.856 GHz bunch phase component of the current. When the signals are sufficiently amplified the electron bunch phase may be analyzed and/or compensated at any of these locations.

The ability to measure the electron phase at several beam-line locations is a powerful diagnostic tool. Used in conjunction with beam position monitors, the performance of the electron gun, linac, beam focusing elements and laser can be studied.

Commissioning of the system was performed using the signal from the linac forward power (LFP) directional coupler port. This signal is a measure of the RF pulse in the waveguide prior to injection into the accelerator. The compensation waveform is simply a scaled and shifted copy of the measured phase waveform. The time shift was determined empirically by stepping the compensation in 10 ns increments in order to minimize the residual RMS ripple on the measured phase. The optimal delay of −870 ns compensates for latency in the electronic equipment and cable delays. The RMS phase ripple is also minimized for a scale factor corresponding to a negative unity gain through the system (a requirement of feedforward systems). The actual optimized scale factor is exactly equal to the measured gain of the SLAC phase shifter. Figure 4.6 shows the effect of the phase compensation system. The peak to peak phase error is reduced from 6.18° to 1.00° and

the RMS phase ripple is reduced from 1.71° to 0.26°. The residual phase ripple has a time constant faster than the bandwidth of the system and is thus uncompensated.

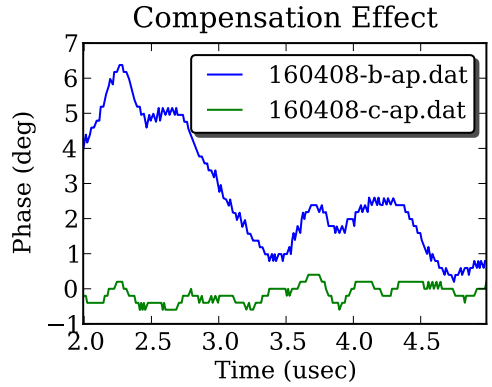

Figure 4.6: The RMS phase ripple in the uncompensated waveform (blue) is reduced from 1.71° to 0.26° with phase compensation active (green).

This system has proven useful, not only for feed-forward compensation, but also as a general purpose measurement tool for RF diagnostics. Beyond the linac drive system, the 2856 MHz repetition rate is present in every part of the system. The ability to easily measure RF amplitude and phase modulations yields a very useful diagnostic for understanding the micro-pulse structure of the electron beam and free electron laser. The system has been successfully demonstrated with alternate RF sources such as beam position monitors and fast photodetectors. It may even be possible to use feed-forward compensation of the RF waveform to control the structure of these alternate source signals.

4.8 Laser Performance

The spectrogram, or frequency vs. time plot, is a very useful visualization of the performance of the free electron laser. The spectrograms in Figure 4.7 show both the temporal and spectral evolution of FEL macro pulses. These data are the result of capturing the laser pulse waveform after filtering by a scanning monochromator. Since this measurement involves a slow spectral scan of the laser, the spectrogram is an average of the laser performance over many independent macro-pulses. Random variations in the electron beam energy are evident from the horizontal bands seen in the image.

Each row of the spectrogram image represents the intensity of a single FEL macro-pulse. The scanning monochromator steps in increments of 0.6 nm between each FEL pulse with a FWHM spectral discrimination of 0.4 nm. The laser waveforms are captured with a LeCroy WaveRunner2 digital oscilloscope. The laser is sampled with two Ge:Au IR photodiodes, one looking at the output of the monochromator and another at the full FEL macro-pulse. The latter is used for normalization. Before each scan a pyroelectric detector is inserted into the beam to measure the full pulse energy in mJ. A typical scan has a duration 75 s and contains waveforms from 300 FEL macro-pulses (given a 4 Hz rep rate). Each waveform represents a different spectrometer wavelength and contains 1000 samples in a 2 µs window containing the laser pulse.

For monochromator data $y_1(t, \lambda)$ and reference pulse data $y_2(t, \lambda)$ the y_1 data can be re-normalized such that the pulse energy seen by the reference detector is held constant. The normalization factor for the ith pulse in the data set (corresponding to wavelength scan steps or rows in the spectrogram plot) is a dimensionless factor such that samples $y'_{1i} = N_i y_{1i}$ are the normalized data rows.

$$N_i = \frac{\int y_{2i} dt}{\langle \int y_{2i} dt \rangle_i} \tag{4.1}$$

The data can be calibrated using the total pulse energy E measured by the pyroelectric detector. Assuming a stable source, the integrals of the reference pulses and the spectrogram are assumed equal to the total pulse energy for calibration purposes.

$$E = \alpha_2 \langle \int y_{2i} dt \rangle_i = \alpha_1 \iint y_1 d\lambda dt \tag{4.2}$$

The calibration factors α are then applied to the spectrogram data to give the plot units of power spectral density (PSD). The same calibration factor may be applied to other data sets captured for the same center wavelength to allow for consistent comparison of PSD. The full pulse power and spectra are calculated by integration of the spectrogram data along the λ and t axes respectively. Figure 4.8 compares the power and spectrum of the spectrograms presented in Figure 4.7 for phase compensation turned on and off.

Figures 4.7 and 4.8 clearly show a change in laser performance with phase compensation activated. With compensation turned off, the pulses have a duration of 0.73 µs and an energy of 1.7 mJ. When compensation is turned on, the pulses lengthen to 1.02 µs with an energy of 2.8 mJ. With the compensation active, the FWHM spectral width also

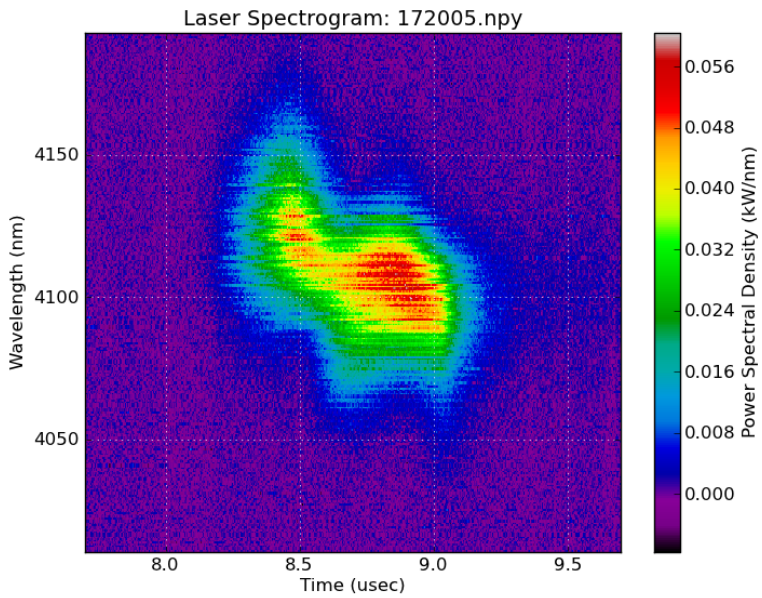

(a) Phase compensation off

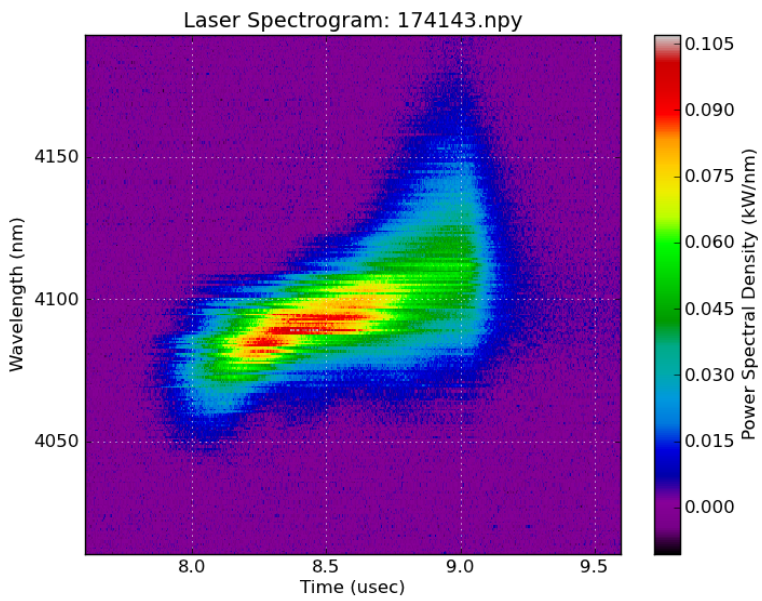

(b) Phase compensation on

Figure 4.7: Spectrograms show the effect of compensation on FEL operation at $\lambda = 4.091\,\mu\text{m}$. Without compensation (a), the laser contains two spectral peaks. Enabling phase compensation (b) results in a narrower spectrum and higher peak power.

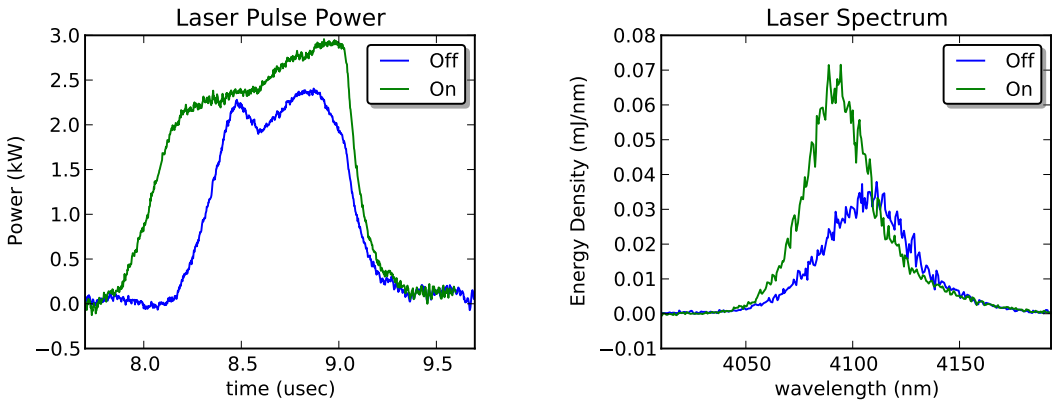

(a) (b)

Figure 4.8: The laser pulse powers and spectra are compared with the phase compensation system on and off. The laser pulse power (a) and spectrum (b) are computed as the integrals of the spectrogram plot in λ and t respectively. The compensation lengthens the pulse duration from 0.73 µs to 1.02 µs, while the spectrum narrows from 40.1 nm to 32.4 nm.

decreased from 40.1 nm to 32.4 nm. It is also observed in Figure 4.7 that the FEL turn on performance improves with compensation. Before phase compensation there are two distinct peaks in the spectrogram with the laser initially starting at a longer wavelength then lasing more strongly at a shorter wavelength. With phase compensation, not only does the instantaneous spectral width decrease notably but there is a continuous wavelength slew as the laser builds to saturation. This wavelength slew, seen in Figure 4.7b, is in agreement with frequency pulling phenomenon predicted by FEL theory[46]. Figure 4.7a shows that without compensation enabled we actually see the reverse of the expected frequency pulling behavior due to the phase perturbations present. The system thus far has focused on achieving the flattest possible amplitude and phase of the linac drive power. An intentional slope added to the phase may be able to mitigate the effects of FEL frequency pulling, thus producing FEL macro-pulses better suited for use in the optical storage cavity for x-ray production.

4.9 Dynamic De-synchronism

During FEL startup there is a discrepancy between the wavelength of spontaneous emission in the undulator and the resonant wavelength emitted during laser saturation. By

imposing a phase slew on the incident electron bunches we can optimize the radiation efficiency for startup and saturation as well as the intermediate turn-on regime. Such a configuration should lead to faster laser turn on, longer pulse lengths, and higher laser pulse powers[47].

Laser turn-on performance may be optimized by slightly decreasing the spacing between electron micro-pulses during laser turn on. This can be achieved by applying a linear phase ramp (i.e a frequency shift) to the RF waveform during the initial part of the macro-pulse and then flattening the phase during the remainder. This way the electron bunch frequency will be properly biased for the small signal gain regime and also appropriate for lasing in saturation.

This technique, known as dynamic de-synchronism[48], is easily applied in software. When the phase compensation waveform is computed to null the phase error an additional deliberate phase waveform is added. The de-synchronism waveform consists of linear ramp with programable slope, sign, and zero phase intercept time. For a given degree of cavity de-tuning, δL, the required frequency bias and thus, phase slew, for optimal laser turn-on can be computed. The intercept point must be determined empirically since improving laser turn on will change the time at which the laser reaches saturation.

This feature of the phase stabilization system is presently under development with experimental results forthcoming.

4.10 Amplitude Stabilization

The stabilization has been recently upgraded with the ability to compensate both amplitude and phase. Since the hardware was designed to capture the complex I/Q signal (see Section 4.3), the modifications involved upgrading the software to derive a feedforward signal from the measured amplitude. Amplitude compensation should be able to correct e-beam perturbations introduced by beam loading in the electron gun, resulting in a more uniform electron beam current and reduced energy spread. An additional independent BNC Model 645 arbitrary waveform generator is programmed with the amplitude compensation waveform in the same manner as the phase compensation AWG. An HP8616, klystron-based, microwave signal generator is used as the master oscillator for the entire RF system. The device includes a voltage controlled PIN diode attenuator for its output that is controlled by an 'Amplitude Modulation (AM)' input port. The rise time of the amplitude

impulse response of this modulator was measured, giving a modulation bandwidth of 1 MHz bandwidth. The AWG output is then fed to the 'Amplitude Modulation (AM)' port of the HP8616 microwave source. The HP8616 AM input directly drives a voltage controlled PIN diode attenuator on its output enabling modulation with 1 MHz bandwidth. New controls added to the GUI give the operator control over the delay, gain, and target level of the amplitude compensation signal. Unlike phase compensation, which always acts to null the phase to zero, the amplitude compensation system derives an error signal by subtracting the reconstructed amplitude from a specified target voltage. The error signal is then applied the specified gain and delay before programming the AWG. The delay is determined by the same calibration procedure used for phase. The gain required is a function of the present nonlinear gain of the klystron. In practice the gain is gradually incremented until the inflection point is found, where the sign of the measured phase is inverted. The final gain setting is that which minimizes ripple in the measured amplitude. In the case that the ITT klystron is operated in saturation, a much larger gain is required to compensate the same magnitude amplitude error. In some instances the gain required to compensate the amplitude ripple has varied by a factor of four.

Figure 4.9 shows the RF waveform amplitude and phase measured at the linac input with amplitude and phase compensation turned on and off. The phase ripple is reduced with the same effectiveness as before with a residual RMS phase fluctuation of 0.7°, a 75 % reduction from the uncompensated phase. The amplitude peak-to-peak variation of 2.2 mV is reduced to 0.7 mV and the RMS amplitude ripple reduced from 0.6 mV to 0.2 mV. This amounts to a 9.3-fold ripple reduction in the RF power delivered to the accelerator.

Given the similarity in effectiveness of amplitude and phase compensation, it is likely limited by one of the common components of the system. The most likely cause of the limitation is the dynamic range of the sampling oscilloscope. The data in Figure 4.9 was collected with 8 bit sampling and the oscilloscope configured for 5 mV/div resulting in a theoretical resolution of 0.16 mV. This is precisely the measured RMS amplitude ripple. If higher resolution compensation is required a higher resolution ADC will be necessary.

The electron beam showed a 30 % reduction in energy spread with amplitude compensation activated. Figure 4.10 shows the electron spectrometer readout signal for the compensation turned on and off.

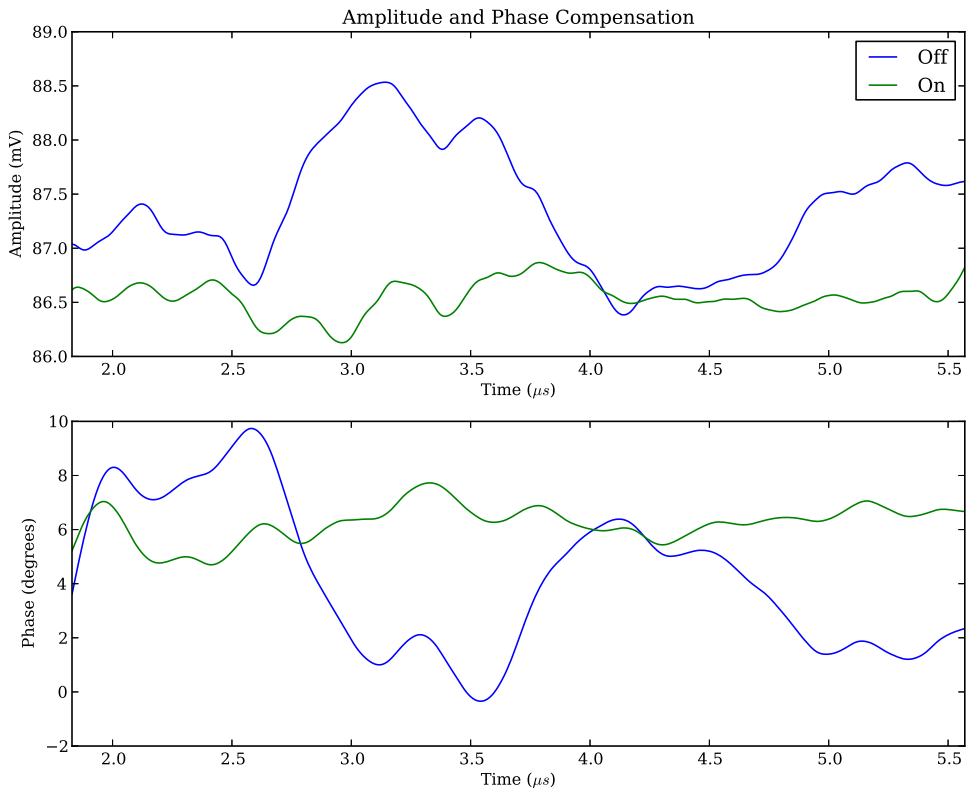

Figure 4.9: The amplitude and phase of the uncompensated (blue) and compensated (green) RF waveforms are plotted for the central 3.5 µs of an RF macro-pulse.

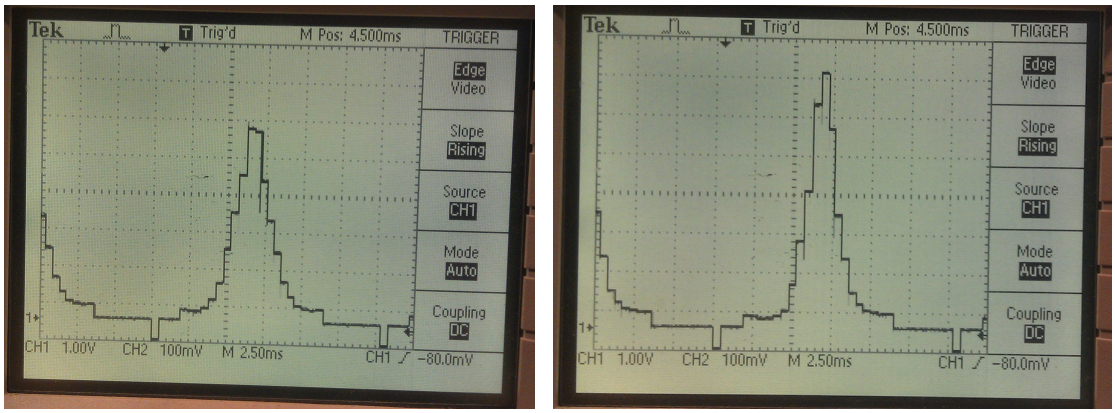

(a) Compensation off

(b) Compensation on

Figure 4.10: The electron beam spectrum with amplitude compensation turned enabled (b) sharpens by 30 %.

4.11 Future Developments

A more sophisticated compensation algorithm should be capable of further reducing the residual phase and amplitude ripples in the RF. The present algorithm produces the compensation waveform by simply scaling and shifting the measured error waveform. This technique relies on the assumption that the feed-forward bandwidth is infinite (i.e. the transfer function $h(t) = \delta(t)$). By measuring the actual transfer function of the system, a more accurate compensation waveform can be constructed by deconvolution of the error waveform and the system transfer function. Performance may even be similarly enhanced by simply applying a low pass filter to the compensation waveform to limit the bandwidth to that of the feed-forward loop. This feature will be implemented in a future version of the control software.

Implementation of a 'running average' mode in the software should eliminate the effects of pulse-to-pulse jitter. Repeatability of the compensation system is presently hindered by incidences where an anomalous pulse is used to computer the compensation waveform. In addition to the existing low-pass filtering of the captured data this averaging will make the system operation more consistent and less prone to operator error. This feature has been implemented successfully using the built-in averaging mode of the digital oscilloscope. It would be preferable, however, to perform this averaging in the control software, so that the operator can have greater control over its behavior.

4.12 Conclusion

The Feedforward Amplitude and Phase compensation system has proven very effective in reducing the amplitude and phase ripples on the accelerator RF drive and electron beam. Flat phase is essential to the efficient operation of the free electron laser and a significant improvement has been measured. These performance enhancements are important steps to maximizing the peak power and pulse length of the FEL used to pump the storage cavity and will enhance the x-ray production rate. The reduced energy spread of electron beam will reduce the spectral width of the x-ray beam, further increasing the spectral brightness.

Chapter 5

Scanning Wire Beam Profiler

5.1 Introduction

One of the more challenging aspects of realizing a Compton backscatter x-ray source is co-alignment of the electron and laser beams. With high intensities and spot sizes as small as 30 µm, it is not possible to blindly align these beams without some special diagnostic tools. The electron beam can be positioned repeatably using strip-line beam position monitors and transition radiation screens. However, the resolution of these techniques are limited to about 100 µm by the sampling electronics and video cameras used. This chapter describes the design and commissioning of a scanning wire beam profile monitor (SWBPM) for performing diagnostics on both the laser and electron beams at the interaction point.

Wire scanners are commonly employed on accelerator beam-lines as alignment aides. The "flying wire" type scanners, such as those used at CERN, are too large to use in the space allocated on the MkV beam-line at UH. The x-ray interaction point, where the scanner must be installed, is shared by two other insertion devices in a crowded vacuum chamber that also housing the x-ray interaction optics. The wire scanner described here is based on the designs used at NBS-LANL[49] and the SLC[50].

The SWBPM is an insertion device integrated into the x-ray scattering chamber described in Appendix B. The wire scanner consists of a 200 µm diameter tungsten wire stretched over an aluminum harp as shown in Figure 5.1. The wire is wound crossing the fork in two perpendicular directions. The insertion axis is inclined 45° above the beam plane so that the two wire crossings are horizontal and vertical. When the fork is translated through the interaction point the vertically oriented wire first crosses the beams followed by the horizontal wire. Since the motion along the wire axis does not affect the amount of beam

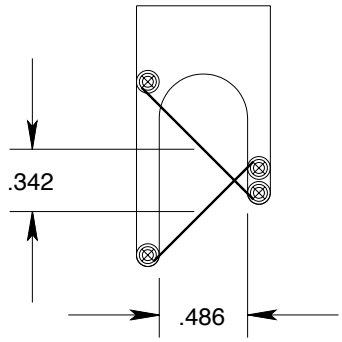

Figure 5.1: Improved second generation wire scanner fork (dimensions in inches)

intercepted, it simulates pure horizontal and vertical motion with a single actuator. The laser beam size and position are determined by measuring the decrease in laser transmission when blocked by the wire, which is measured with a pyroelectric detector outside the vacuum chamber. Intercepted high-energy electrons will ionize the wire, ejecting secondary electrons, creating a positive voltage pulse. This pulse is transmitted by coaxial cable to a $50\,\Omega$ load and is sampled with an oscilloscope. The 'as built' longitudinal position of the wire scanner *defines* the longitudinal position of the interaction point. The transverse position of the IP is fixed by the e-beam focusing quadrupole positions and the wire scanner will be calibrated for this axis.

This chapter describes the wire scanner mechanical design, electronics, computer control, and data acquisition system. The results of calibration experiments and preliminary beam measurements are presented, followed by plans for future improvements to the system.

5.2 Wire Scanner Design

5.2.1 Scanning Wire Head

The wire scanner head consists of an aluminum fork with a 0.486" gap with a tungsten wire spanning it. The dimensions were chosen to maximize the beam aperture through the fork as constrained by the translation stage range of motion and the clearances with other IP insertion devices. The wire is wound in a V shape around four plastic standoffs as shown in Figure 5.2 and secured with an insulated clamp before being terminated on the support shaft. The fork is attached to the end of a 1/4" stainless steel (SS) rod the other

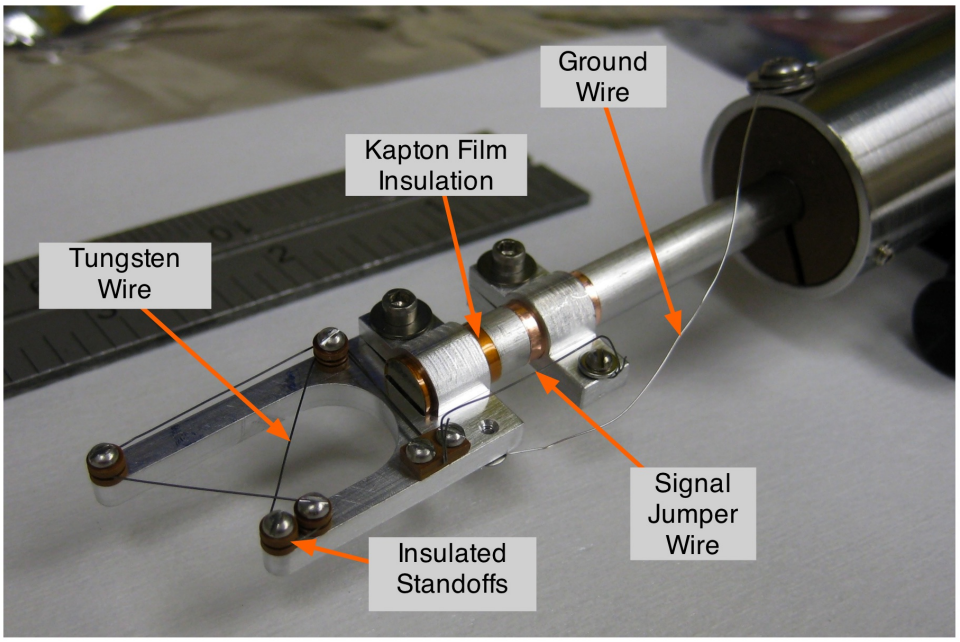

Figure 5.2: The second generation wire scanner fork electrically isolates the wire from the fork with plastic standoffs. The mounting rod is connected to the wire and conducts the signal to the vacuum feedthrough. A second wire grounds the fork to the vacuum chamber wall.

end of which is clamped to the center contact of a BNC connector vacuum electrical feedthrough. The narrow rod is centered and supported by two plastic insulating discs within a 1" SS tube welded to the electrical feedthrough reducer flange. The spacers stabilize the rod and maintain alignment. The completed wire scanner assembly is shown in Figure 5.3 and Figure 5.4 shows the full system integrated into the x-ray scattering chamber.

The BNC connecter allows extraction of a current generated by the collection of secondary electrons when the high-energy beam passes through the wire. The two wires forming a V are oriented at 90° relative to one another. When the head is inserted into the beamline at 45° the two wires provide subsequent horizontal and vertical scans with a single motion. The fork body is connected to the support tube by a grounding wire to prevent charging due to intercepted electron beam.

The first commissioned wire scanner fork did not include any electrical isolation between the fork, wire and mounting rod. These components were connected as a single unit and fed the signal directly to the BNC connector center conductor. Initial tests showed

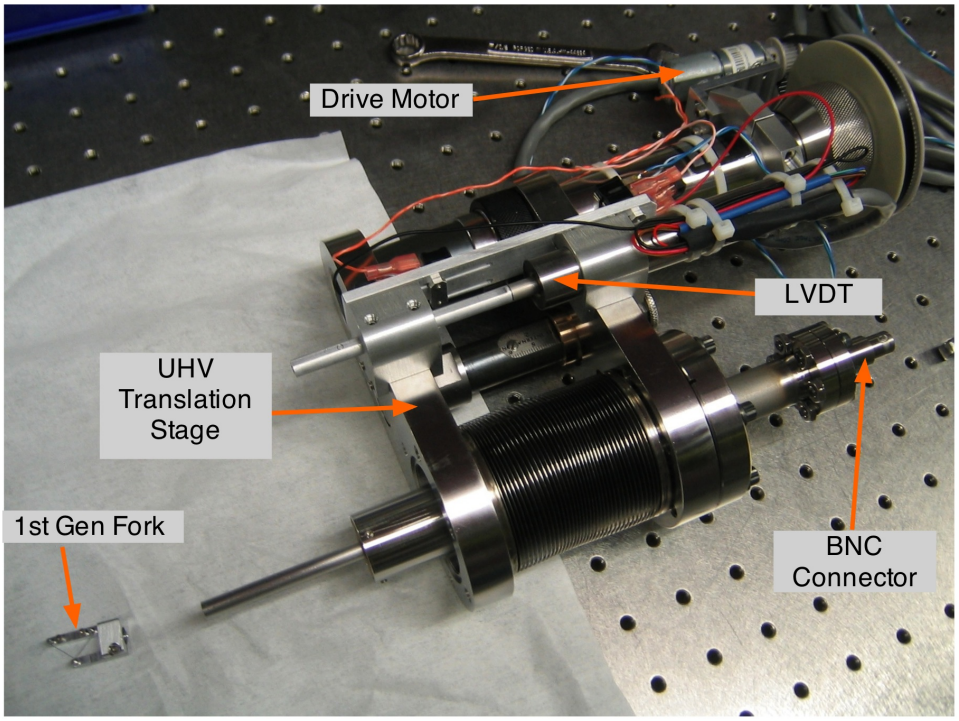

Figure 5.3: Scanning Wire Beam Profiler drive assembly and first generation fork. The wire and fork are electrically connected to the support rod, which conducts the signal to the vacuum feedthrough on the far end.

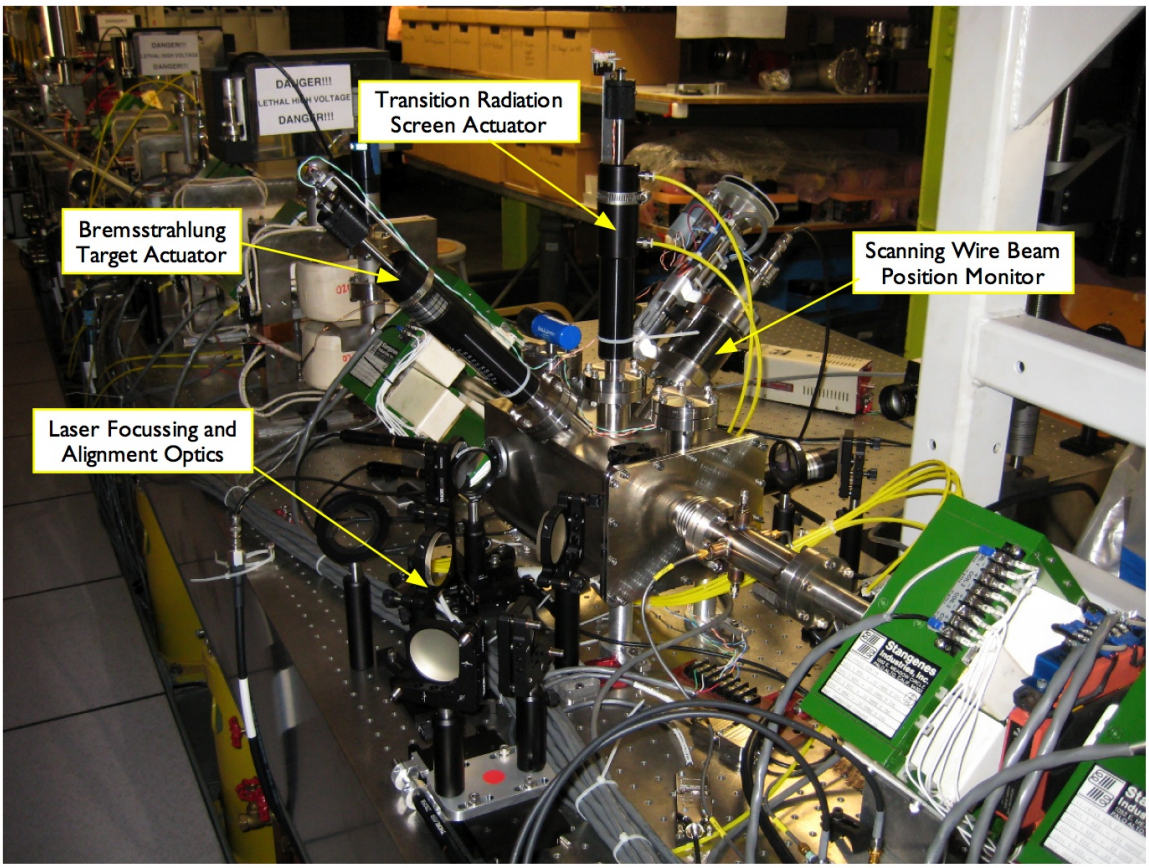

Figure 5.4: The Scanning Wire Beam Position Monitor is installed along with other insertion devices on the x-ray scattering chamber on the MkV FEL beamline.

that a large background, presumably due to the beam halo intercepting the aluminum fork, prevented discrimination of a useful signal from the wires. In cases where the beam was clearly transmitting through the fork between the wires, a strong background was still observed. The 200 µm Re wire used was also brittle and prone to breakage during winding.

The redesigned second generation fork described above was made as large as possible given the space limitations in the vacuum chamber near the interaction point. The wire is now wound around plastic standoffs screwed to the aluminum frame. A tungsten wire proved much easier to wind without breaking and should not melt when subjected to the high current e-beam or high intensity laser pulses. The mounting rod is still used as the electrical connection to the BNC connector center pin but is now isolated from the fork with Kapton film and provides a termination anchor for the wire. The standoffs also serve to bend the wire at a larger radius than the previous design reducing stress. The fork itself is connected to the vacuum chamber body by a grounding lead to bleed charge accumulated from scraping e-beam.

5.2.2 Translation Stage

Precision translation of the wire scanner head is achieved using the MDC Vacuum 665503 single axis translator. This device allow precise control over the distance between two 2 3/4" ConFlat flanges connected by a welded bellows. A precision 18 TPI lead-screw controls the separation and is turned by a DC motor. A reducer flange is used to connect a BNC connector electrical feed-through to the translator. A 1" diameter stainless steel tube is welded to the inside of the reducer flange to serve as a rigid guide for the scan head shaft. The scan head shaft is attached to the electrical feed-through with a copper finger coupling and centered within the guide tube with insulating plastic spacers. The wire scanner actuator must be mechanically stable offering repeatability and scan precision on the order 1/10th the beam size or 3 µm.

5.2.3 Translation Stage Drive

The translator lead-screw is driven by a DC motor and gear-train. The motor drive speed was chosen to meet the scan resolution requirement of 3 µm with a 5 Hz beam repetition rate. The nominal continuous scan speed is then $15\,\mu\mathrm{m\,s^{-1}}$ and with the 18 TPI lead-screw pitch yields a 0.64 rpm rotation rate.

A maximum drive speed of 1 ”/min was chosen to achieve reasonable times to fully retract the wire scanner fork away from the beamline. This corresponds to a maximum shaft rotation of 18 rpm. Driving the motor with a digital pulse-width-modulation (PWM) controller with an 8-bit duty cycle resolution gives a theoretical speed control resolution of 0.07 rpm, which is suitable for this application.

The MDC665503 translator starting torque was measured to be 37 oz-in so a 90 rpm, 8 oz-in motor with a 5:1 external gear reduction should provide adequate speed and torque. Unfortunately, the motor stalled at anything below full speed so the motor was replaced by a 32 oz-in higher torque model. Even with the new motor the minimum speed was limited to ~ 2 rpm to prevent stalls. This corresponds to a $47\,\mu\mathrm{m\,s^{-1}}$ minimum scan speed and a 9.4 µm scan resolution. Although three times the specification, this is still a sufficiently high resolution for analysis of a 30 µm beam spot.

5.2.4 Position Readback

A linear-variable-differential-transformer (LVDT) is mounted on the side of the translator and precisely measures the position of the wires. The active range of the LVDT covers the entire range of motion of the wire scanner, including the parking position. Limit switches are installed to prevent the motor from overdriving the stage and to set the fully retracted parking position.

The LVDT readout module provides a 12 bit digital position value over a serial connection. The readout was calibrated by comparing the translator flange spacing, as measured with calipers, to the digital output. One unit on the LVDT readout corresponds to 10.1 µm of scan motion. This resolution is limited by the need to span not only the ≈ 20 mm scan range but also the actuator park position for a total range of 32 mm. The readout resolution shows fluctuations of about ± 2 making the effective instantaneous resolution ± 20 µm.

5.2.5 Data Acquisition and Analysis

Typical wire scans are performed with the actuator speed set to $66\,\mu\mathrm{m\,s^{-1}}$. Data is sampled every five LVDT counts or 50.1 µm for an average sample interval of 0.77 s. A full automated scan over 14 mm takes approximately 3.5 min during which the beam is sampled at 280 positions. The sample rate is limited by the latency of the digital oscilloscope, which

captures the wire current waveforms. The sample interval is also kept at five LVDT counts so that duplicate position measurements are not recorded due to random fluctuations of ± 2 in the LVDT readout.

System control and data acquisition is performed by custom software developed in Python. The `WireScannerControl` class serves as the backend providing low-level control over the motor, LVDT readout, digital oscilloscope and analog to digital converter. It also provides all of the logic for seeking the motor to a particular LVDT position, scanning a given range, and acquiring and storing the data. This class also provides a basic command line interface used for debugging. An overview of the data acquisition system is shown in Figure 5.5.

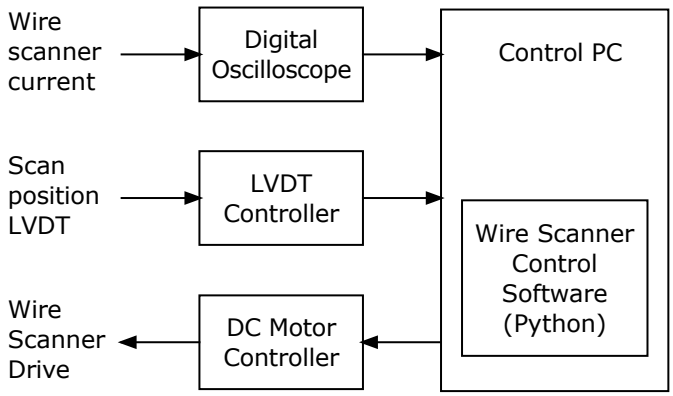

Figure 5.5: The current picked up by the wire scanner is sampled by a digital oscilloscope and read by the control PC over a USB connection. The digital LVDT position and the motor controller are both interfaced over an RS232 serial connection.

The `WireScannerControlGui` module provides a comprehensive graphical user interface for the wire scanner system. The main window created using the wxPython[45] toolkit is shown in Figure 5.6. The top row of buttons contains controls for: 'Scan' over the given range at the given speed, 'Seek' to a specific location, 'Stop' the motor, 'Save' data to disk, and 'Park' the wire scanner in its home position. The second row contains shortcuts for scanning over preset horizontal and vertical ranges and a continuous sampling mode used for debugging. In the future the software will be able to fit peaks in the data and instantly display the beam position, however, this analysis is presently performed offline with a standalone analysis script.

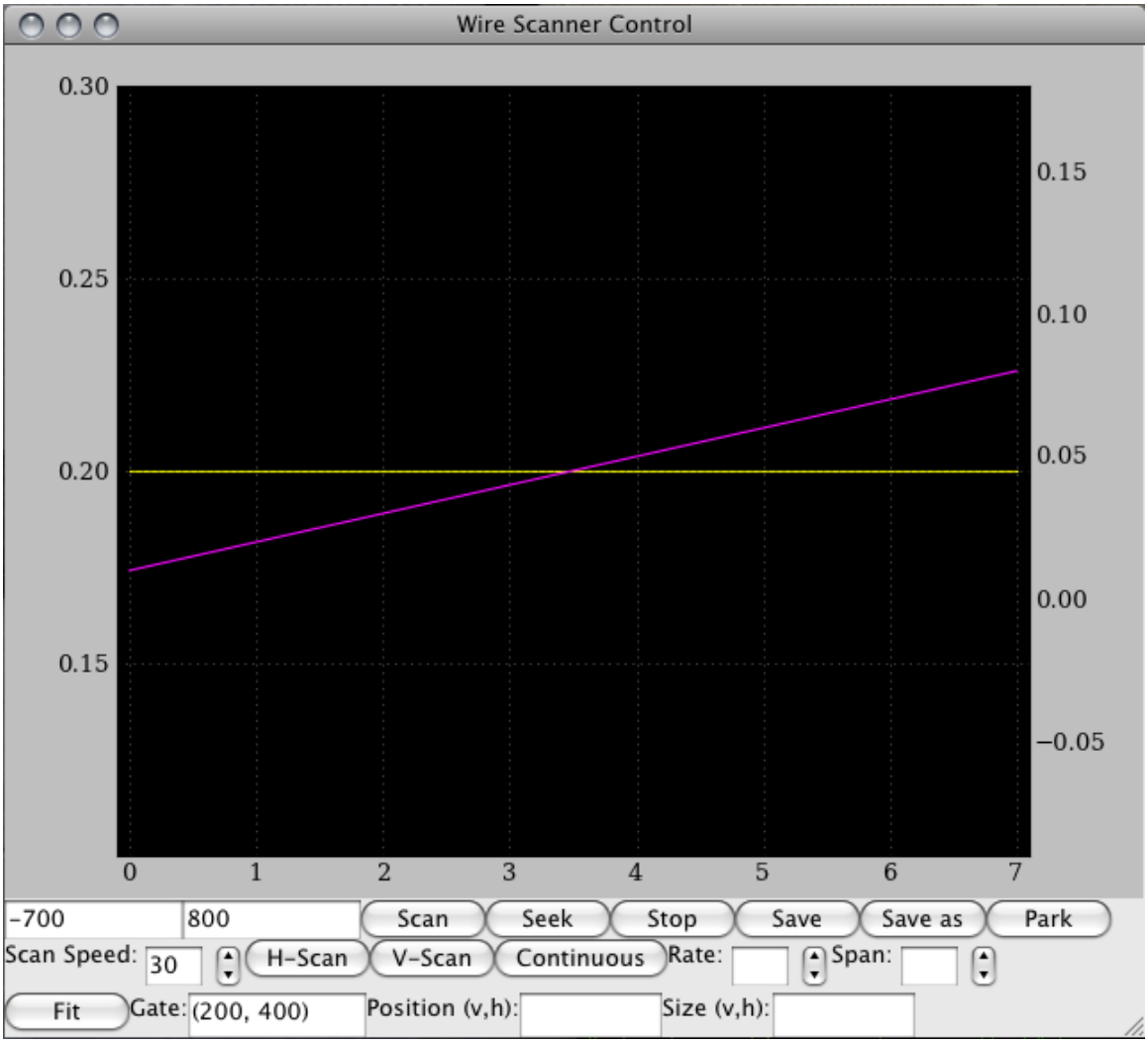

Figure 5.6: The graphical user interface for the SWBPM presents the electron beam (yellow) and laser (purple) beam profiles in the plotting area and is updated in real time during a scan. The buttons below allow the operator to configure scan parameters and perform analysis on the sampled data. Note that the figure does not show actual scan data, but rather debugging data.

When a 'Scan' command is issued, the wire scanner will automatically 'Seek' to the scan starting position. During a scan, the motor is run at a constant speed and the LVDT position sampled at 100 ms intervals. We presently do not have a means to trigger the computerized data acquisition synchronously with the master e-beam trigger, so when the LVDT reading has increased by five units, the most recently acquired data is retrieved from the oscilloscope. The oscilloscope itself is triggered synchronously with the electron beam and always displays the last pulse waveform. For a typical system repetition rate of 5 Hz there is potentially a 200 ms latency between the LVDT reading and the associated scope data. The systematic component of this error results in an a offset in the absolute measured position of the beams, but should have little effect on the size or relative positions between the two beams; a slight hysteresis may result for scans performed in opposite directions. The latency may also present some random error, however, it is, at most, of the same order as the uncertainty in the LVDT position measurement. The effect of these random errors on measured beam positions and sizes are negligible once curve fitting is applied to the data.

The absorption of the laser by the wire is measured with a pyroelectric detector monitoring the beam transmitted through the interaction point. The response of the pyro is considerably slower than the secondary emission current and cannot be sampled in the same oscilloscope timebase. Since the pyro only measures integrated energy, a boxcar integrator is used to sample the peak voltage and provides a DC signal digitized with a low speed ADC. A LabJack U8 data acquisition module is used to sample this signal and is read out concurrently with the oscilloscope data over a USB connection.

When the scan is complete the motor will stop and the user may review the data on-screen or save it to disk. Each scan consists of about 280 oscilloscope captures of 600 samples each in addition to the LVDT positions, laser current readout and time stamps. This data is stored in the the NumPy '`.npz`' self-describing binary data format with a typical file size of 1.3 MB. Figure 5.7 shows the data collected from a scan over the focussed electron and laser beams and processed with the `plotscan.py` data analysis script. The upper plot shows the electron beam evolution in time, while the lower plot shows the average laser beam and electron beam positions during a specific window in time. In most cases, the window is chosen for the duration of the laser pulse since this is the region over which the two beams must stay co-aligned for x-ray production. Note from Figure 5.7, that while the beam remains well aligned in the vertical direction (left peak) over the 3 µs pulse duration, the horizontal position of the beam slews by 3 mm and defocusses during the last 2 µs. This

likely reflects an energy slew in the electron beam. The fast deflection in the first half microsecond is attributable to a high voltage kicker used to gate the electron beam prior to injection into the linac. The start of the pulse also shows the effect of beam-loading in the linac. Data such as these are useful for tuning the electron beam to reduce energy slew and achieve the desired tight focus at the IP. Figure 5.8 shows the electron beam imaged by the transition radiation screen at the interaction point.

5.3 Calibration

The wire scanner translator flange separation was measured with both calibers and the LVDT for two different positions giving an LVDT calibration of 10.1 µm/count. Displacement measurements must be divided by $\sqrt{2}$ to give actual wire displacement along the horizontal and vertical axes.

A small hysteresis was detected in the scan motion. Even for very low scan speeds an offset of 3 counts or 30.3 µm exists between beam positions for scans run in different directions. Repeating the scans for different scan speeds indicates that this error is not consistent with sampling lags in the electronics. Although a backlash specification was not provided by the stage manufacturer, there must be mechanical backlash in the translator lead-screw, probably as a result of the torque applied between the translator flanges by vacuum pressure. Fortunately this error does not affect the repeatability of measurements made in one scan direction nor does it affect the relative position of the electron and laser beams found from the scans.

The FEL alignment HeNe is aligned to the x-ray scattering chamber following the procedure described in Section B.2. The HeNe beam is then scanned to determine its position at the interaction point. This beam position is compared with that of a well aligned electron beam at the IP and corrections are made using the final steering mirror to ensure that the HeNe is aligned to the nominal electron beam position. The IR FEL beam will then follow the same path as the alignment HeNe and be co-aligned with the electron beam.

5.4 Experimental Results

Preliminary experiments have been performed to measure the sizes of the laser and electron beams. The system was set up for optimized laser performance with an electron

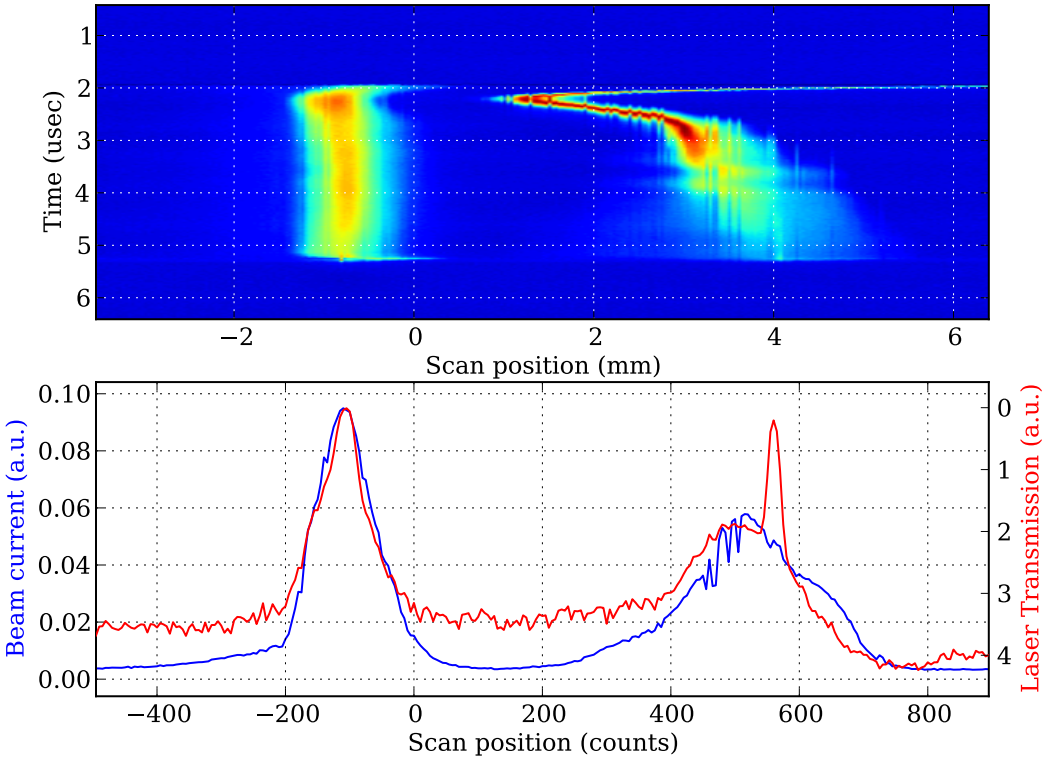

Figure 5.7: Wire scan results are processed by the `plotscan.py` data analysis script to produce space-time plots of the electron macro-pulse structure. The upper plot shows the shape of the electron beam as a function of time along the vertical axis and wire position along the horizontal axis. The left feature represents the vertical beam size and position, while the right-hand feature is the horizontal beam size and position. The lower plot shows time integral (blue) of the wire current from 4 µs to 5 µs. This interval of the electron beam is being used to run the free electron laser. The laser transmission (red) shows broad peaks that overlap the electron beam, indicating that laser performance is decreased while the wire is intercepting the electron beam. The sharp horizontal feature (right) in the laser transmission (red), corresponds to the scan range over which the wire blocks transmission of the laser beam directly.

Figure 5.8: The e-Beam is imaged at the IP using the transition radiation screen with a Vidicon-tube TV camera. Each pixel is 35 µm × 35 µm giving an approximate beam size of 2.0 mm × 0.6 mm. These beam dimensions agree well with the wire scanner results in Figure 5.7, however, notice that the instantaneous horizontal beam size is much less than 2 mm since the video image is integrated over time.

beam waist at the x-ray IP. The electron beam has not yet been optimized for x-ray production at the IP. The data set plotted in Figure 5.9 shows an electron beam well collimated in the horizontal axis while moving and diverging in the vertical axis. This beam is not ideal for x-ray production, however, it provides valuable feedback on the electron beam quality and configuration that would not be observable using only viewing screens and toroid currents. In preparing for an x-ray production experiment we will need to iterate several times between optimization of the IP focus and laser performance using wire scanner data as a benchmark.

These data show an interesting and unexpected anomaly between 4.5 µs and 5.4 µs. A narrow peak appears in the vertical scan wire current 3.5 times the amplitude of the e-beam current. The same peak also appears in the horizontal scan, but more weakly. This peak is aligned with the absorption peak for the laser and must be some kind of photocurrent induced by the laser on the wire. The peak also extends past the end of the electron beam pulse by about 200 ns consistent with the propagation delay between the laser and the IP. The width of the laser transmission peak is $\sim$ 250 µm which accounts for the diameter of the beam plus the diameter of the wire. The photocurrent peak by comparison is only 120 µm wide in the vertical direction. This implies that the effect is not present for the

entire transit of the wire through the laser beam. This effect has only been observed for a highly focussed laser beam, so it is very likely to be dependent on intensity and not just total power. Since the surface of the wire is cylindrical, the intensity of the laser on the exposed wire surface is not constant but peaks when the laser is centered on the wire and at normal incidence. This angular sensitivity greatly enhances the resolution of the wire scanner without reducing the diameter of the wire.

The laser wavelength of 3.18 µm is too long for photo-ionization of the tungsten wire but the current could possibly be a multi-photon effect. This is supported by the sharp dependance of the current on laser intensity. Another possibility is a change in the secondary emission characteristics of the metal due to a surface plasma generated by the laser pulse. This is not consistent with the observation of the effect after the end of the electron pulse, but it does explain the difference in peak current for the horizontal and vertical scans. The laser beam is expected to be a pure TEM_{00} gaussian, due to the simplicity of the transport optics, so the difference in these peaks can only be attributed to a dependance on the current density on the wire at the same time. In this case the electron beam is far more diffuse along the horizontal axis so the laser pulse does not lead to enhanced secondary emission. It is not possible that the visible coherent spontaneous radiation from the FEL could cause this effect since the shorter wavelengths would not focus tightly with the lens configured to focus light at 3.18 µm. This discovery is a valuable diagnostic tool to allow us to measure the size and position of the laser beam with high precision.

5.5 Future Work

The experience with the wire scanner system so far has led to plans for several future improvements. First, the addition of a third wire such as used at Tesla TTF[51] can provide a measure of the xy moment of the beam in addition to the x^2 and y^2 moments that are presently measured for beam characterization. This extra information would allow us to see any rotation in the beam spot that may lead to an over estimate in the beam size. Second, upgrading the drive motor to a high torque stepper motor should enhance the resolution and repeatability of scans by allowing for discrete motions between samples rather than continuous motion. Sampling the wire current only when motor is stopped will reduce the effect of latency error in the position reading. Third, a true hardware based trigger must be made available to the data acquisition software of this system and several other data

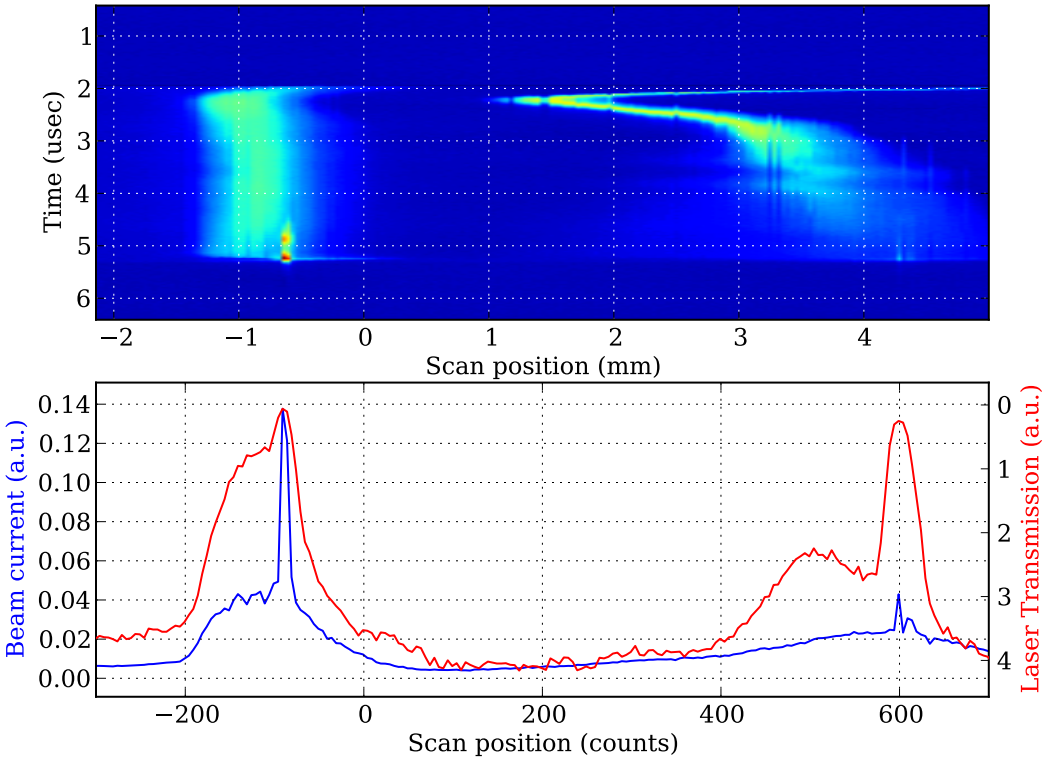

Figure 5.9: An additional peak is observed in the wire current at positions -89 and 599 when the laser beam is tightly focused. The left peak (vertical) is 3.5 times greater than the current due to the electron beam. This signal is indicative of a photocurrent generated by the intense laser pulse. The photocurrent peak is coincident with the positions of the largest laser absorption peaks observed by the pyroelectric detector.

acquisition systems used in the MkV FEL Lab so that data can be acquired synchronously with the electron beam repetition rate. Presently all of these systems acquire oscilloscope data asynchronously resulting in duplicate or missed samples.

Another promising application of the wire scanner is the characterization of the electron using phase space tomography[52]. Time resolved beam emittance measurements can be performed by using the wire scanner in conjunction with quadrupole scans. Although far more time consuming to perform, this technique is expected to have a greatly reduce background compared with the presently used video capture method in addition to providing data on the temporal evolution of the emittance during an electron pulse.

5.6 Conclusion

This compact, precision wire-scanner has been constructed at low cost with minimal custom fabrication. The use of a commercial UHV translation stage greatly reduced the engineering effort since few other moving parts are required. All other components were fabricated, welded and assembled in-house.

A limitation of this wire scanner is that the large 200 µm wire cannot resolve the size of the desired 30 µm beams. For operational purposes, however, the *positions* of the beams are of greater importance. Even for a tightly focused beam a fit of the scan data gives a repeatable measurement of beam position.

The size of the laser spot at the interaction point can be well characterized using the wire scanner. Scans of the laser beam size for different longitudinal lens positions, and thus, different waist positions, will yield the divergence and waist size of the beam. Since the optics for transporting the pure TEM_{00} FEL beam are fixed, the longitudinal waist position depends only on the final focus lens position while the size depends only on the laser wavelength, which may be accurately measured. Therefore, once the laser has been characterized and Compton backscattered x-rays are observed, the laser itself can be used as a 'wire' to provide an accurate diagnostic for characterization of the electron beam. Such laser-wire systems are used at other accelerator facilities to provide non-destructive beam emittance measurements[51]. Rastering the alignment of the laser spot at the IP can produce a map of the election current distribution as a function of time and possibly energy if the x-ray spectra is observable. This technique could be used for subsequent optimization

of the tight electron beam focus without the need for a smaller diameter wire, which may be damaged by high beam currents and powers at the IP focus.

This scanning wire beam profiler is an essential diagnostic tool for the alignment of the Compton backscatter x-ray source. The co-alignment of the laser and electron beams to µm resolution is critical to establishing a high luminosity interaction and a high brightness x-ray beam. The capability to also measure the time evolution of the electron beam profile during a macro-pulse is a valuable new diagnostic for the optimization of the free electron laser.

Chapter 6

Conclusion

The demand for high brightness sources of x-rays has driven the development of many synchrotron light sources, as well as x-ray FELs. However, limited resources at large scale accelerator facilities necessitates the development of compact x-ray sources accessible to smaller institutions and the private sector. The possibility of private ownership and operation of light sources is of particular interest to organizations conducting proprietary research in the fields of genomics, proteiomics, and pharmacology. Compton backscattering allows high brightness x-rays to be produced with electron beam energies orders of magnitude lower than those at a synchrotron; this allows compact sources to be constructed at significantly lower cost. Many of these laser Compton sources are presently under development. However, since most rely on terawatt peak power lasers with very low repetition rates, their average power is too low to be useful in many applications of interest. These limitations can be overcome by using GHz-rate electron and optical beams, together with an optical storage cavity, to increase the average brightness of the source. The approach constitutes a system uniquely suited to RF linac free-electron lasers.

This dissertation has investigated many of the challenges involved in designing, constructing, and using an optical storage cavity-based laser Compton x-ray source at the MkV Free-Electron Laser Laboratory at the University of Hawai‘i. The optical power enhancement provided by the storage cavity overcomes the limitations to x-ray production rates imposed by the low Compton scattering cross-section. The optical storage cavity-based source can be readily scaled from x-ray to gamma-ray production by simply increasing the electron beam energy. Indeed, the use of optical storage cavities has been proposed as the method of gamma-ray production for a future γ-γ collider at the ILC. The intense

optical fields present in an optical storage cavity also provide opportunities for the study of high-field QED effects, such as vacuum birefringence and pair production.

The primary focus of this research, described in Chapter 2, was the development of a prototype optical storage cavity required to establish the design principles, alignment criteria, and physical characteristics relevant to an infrared storage cavity. The full high-power IR storage cavity system requires exquisitely aligned and stabilized mirrors to achieve optimal power enhancement simultaneously with a tight focus at the interaction point. The four-mirror low-power visible test cavity has proven a valuable tool for the development of technologies required to achieve this goal. Alignment techniques have been developed to achieve a near diffraction-limited, near-concentric focus using a pair of astigmatism compensating cylindrical focusing mirrors. Several novel diagnostic techniques using optical modulation sidebands and RF detection techniques have been explored and demonstrated to be important tools for IR cavity development and operation. In particular, these techniques have allowed for the precision measurement of the cavity length, concentricity, and finesse, which are the most important characteristics of the IR storage cavity. Future work includes the implementation of the Pound-Drever-Hall stabilization system described in Appendix A and further refinement of these diagnostic techniques. An infrared test cavity is also being developed to demonstrate synchronization and pulse stacking using the MkV FEL.

Chapter 3 discussed a stabilized tunable reference laser (STRL) designed to couple the stabilization systems of the FEL and the optical storage cavity. This system adapts technology developed to sweep the wavelength of diode lasers used in atomic spectroscopy experiments to a broadly tunable frequency reference for external cavity stabilization. This system is composed of entirely off-the-shelf hardware and utilizes a software defined radio system for RF diagnostics and control. This system will serve as the frequency reference for the optical storage cavity and FEL stabilization systems discussed in Appendix A.

The feed-forward amplitude and phase compensation system presented in Chapter 4 is critical to both operation of the FEL at peak efficiency and optimization of the Compton scattering efficiency. Amplitude and phase ripple in the high-power microwave drive to the accelerator result in variations in electron micro-pulse phase that prevent operation of the laser over the full macro-pulse duration. It has been demonstrated that the feed-forward system is very effective in smoothing the electron beam phase, resulting in improved laser performance. Future development of a dynamic de-synchronism technique

and enhancements to the control software are expected to further optimize laser performance. The increased electron beam phase stability will also improve synchronization with the laser pulses in the optical storage cavity, resulting in enhanced x-ray production by ensuring optimal overlap of the electron and laser pulses at the interaction point during the entire macro-pulse.

The scanning wire beam profiler described in Chapter 5 was shown to be an important diagnostic tool for achieving 3-dimensional overlap of the pulses at the IP and for optimizing the x-ray source. The ability to precisely co-align a tightly focused electron beam and laser beam has been demonstrated; the novel observation of a laser photocurrent due to interaction with the wire results in higher than anticipated scan resolution. The wire scanner also serves as a critical diagnostic for visualization of the electron macro-pulse evolution in space and time, revealing critical dynamic beam overlap issues that must be addressed to maximize x-ray production. With this new capability, these previously unavailable data may now be used for the optimization of the entire compact x-ray source. The mechanical, optical, and vacuum systems for the x-ray interaction point were also discussed in Appendix B.

Work is ongoing at the University of Hawai‘i to commission a proof-of-principle single-pass Compton backscatter x-ray source. This work is primarily driven by the demand for x-ray photons to test emerging high-speed x-ray detector technologies under development at UH. Using the experience gained with the four-mirror test cavity, a *high-power* optical test cavity is presently being developed to demonstrate synchronous pulse stacking and cavity stabilization. Finally, the full high-power optical storage cavity with integrated stabilization systems will be constructed and installed on the MkV FEL beamline providing high spectral brightness x-ray photons and advanced detection capabilities for a wide range of experimental applications.

Appendix A

Optical Storage Cavity Stabilization

A.1 Introduction

Stability is of critical importance to any high finesse optical storage cavity. To achieve the strongest possible optical fields within the cavity's interaction region the size of the mode waist must be minimized. The minimum possible beam waist is achieved when the centers of curvature of the cavity mirrors intersect exactly. While this will allow the most tightly focussed mode, this concentric geometry is only critically stable. The use of a concentric cavity requires not only a careful intersection of the mirror centers of curvature in the longitudinal direction but also precise transverse overlap as shown in Figure A.1. Since a concentric resonator is intrinsically unstable, and thus, impracticable, the proposed storage cavity will consist of a near-concentric resonator where the centers overlap by a finite distance s.

The overall length of the storage cavity was chosen such that every 9th incident FEL micro-pulse overlaps with a pulse circulating within the cavity. For an $f = 2856\,\mathrm{MHz}$ micro-pulse repetition rate, this corresponds to a cavity length of $L = 9c/2f = 472\,\mathrm{mm}$. For this cavity, a mode with a waist radius of $20\,\mu\mathrm{m}$ is theoretically possible with an $s = 8\,\mu\mathrm{m}$ overlap of the mirror curvatures. In practice the alignment and surface figure of the cavity mirrors play a substantial role in achieving a tightly focussed waist.

An initial attempt to stabilize the 4-mirror visible test cavity was unsuccessful due to high cavity finesse. The round trip loss for the cavity should lie in the design range 1.0 % to 1.4 % given a finesse from 450 to 630. The nine pulse cavity has length

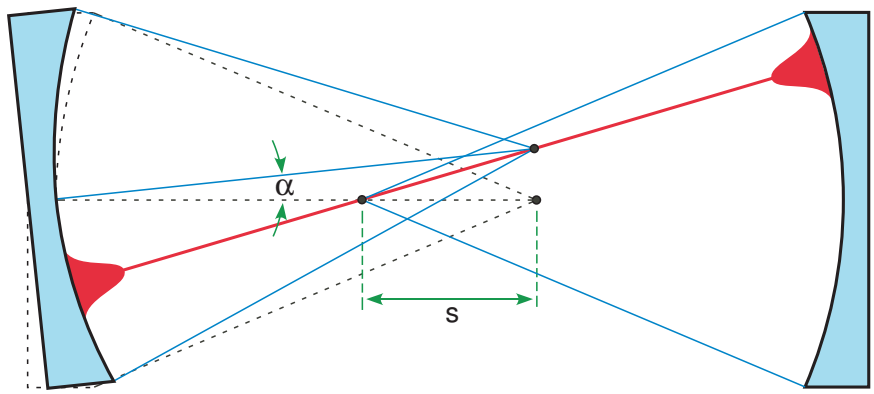

Figure A.1: A two mirror optical resonator is only stable if the centers of curvature of the mirrors lie on a line which intercepts the surface of each mirror with sufficient beam aperture. As the spacing between the centers is decreased to zero (purely concentric) the permissible angular misalignment α of the mirror axes also goes to zero.

$L = c/2\nu_{\mathrm{ax}} = 472.3\,\mathrm{mm}$ for $\nu_{\mathrm{ax}} = 2856\,\mathrm{MHz}/9$. The cavity mode FWHM can then be determined from the finesse:

$$\mathcal{F} = \frac{\nu_{\mathrm{ax}}}{\delta\nu} \tag{A.1}$$

For $\mathcal{F} = 450$ the cavity modes are only 700 kHz wide corresponding to a cavity length offset of $\delta L = \frac{\delta\nu}{\nu_{\mathrm{ax}}}\frac{\lambda}{2} = \frac{1}{\mathcal{F}}\frac{\lambda}{2} = 0.7\,\mathrm{nm}$. Thus, the cavity must be stable to better than a fraction of 0.7 nm in order not to drift off resonance and losing a sign discriminant error signal. This is simply not possible with the 20 nm resolution piezo stage presently in use. Even if a high resolution positioner where used to set the cavity length, its bandwidth would need to be in excess of 10 kHz to stabilize against the observed cavity jitter. Mechanical resonances in the existing mounts presently limit the feedback bandwidth to less than 100 Hz. These problems can be overcome by applying a stabilization technique capable of generating a valid error signal while off-resonance, relaxing the control bandwidth requirements.

There are two significant regimes of stability for the optical storage cavity. First, intra-pulse stability: the cavity must remain resonant over the duration of the FEL macro-pulse (nominally 4 µs). The accumulated phase walk-off error of pulses over their lifetime in the cavity should be less that $\pi/2$. For a nine-pulse cavity with a finesse of 1000, the $1/e^2$ pulse lifetime is 1 µs or 1/4 of the macro-pulse length. Second, inter-pulse stability: the cavity must not drift off resonance in the > 100 ms interval between laser pulses. The first case is best approached by careful attention to the mechanical design of the optical storage

cavity. The bandwidth of any intra-pulse noise will exceed 250 kHz so that active feedback would be impractical to implement with mechanical actuators. Electro-optic and acousto-optic devices may prove useful but would greatly increase the complexity of the system. In the second case, the cavity must be stabilized against thermal drift and vibration which could affect tuning between successive macro-pulses.

The storage cavity requires three stabilization systems. First, in order to maintain stable transverse alignment, one of the cavity mirrors must be actively steered by a control system using feedback from a beam profiler outside the cavity. Analysis of the transmitted mode shape will provide the necessary feedback to steer the cavity mirrors along two axes and to adjust the cavity concentricity to maintain a stable mode size. Second, the overall length of the cavity must remain locked to an axial mode of the laser source. This is achieved by using the well known Pound-Drever-Hall[53, 54] method of feedback control. Third, to achieve the highest possible fields, successive optical pulses must stack temporally within the cavity. This requires locking to the particular axial mode, which optimizes the stacked pulse power in the cavity. The remainder of this chapter will deal primarily with the development of these cavity stabilization systems.

Due to the transient pulsed nature of the FEL pulses used to pump the cavity, no beam is available during the inter-pulse period with which to stabilize the cavity. The proposed solution is to include an auxiliary optical cavity parallel to the high power cavity that is always locked to a stable, low-power, continuous-wave light source[4]. Incorporation of the auxiliary cavity mirrors into the same mirror mounts as the main cavity mirrors provides a close analogue to any disturbances acting on the main cavity. A benefit of this auxiliary cavity is that its geometry can be chosen specifically for the purpose of obtaining an error signal for use with a PDH stabilization scheme without the alignment sensitivity and complexity associated with the near-concentric main cavity.

Another advantage of the auxiliary cavity is that it allows for a choice in the laser source used for stabilization. If a CW mode-locked YAG laser were used as the pump laser in place of the FEL, then a single longitudinal mode could be filtered out resulting in a low power CW beam. This beam could then be used in the auxiliary cavity for stabilization, while remaining in phase with the high power pulses. Precision alignment of the system would be complicated by the invisible infrared YAG radiation.

An independent laser source such as a HeNe or a tunable diode laser may be used with its own external stabilization as a standard against which to stabilize the auxiliary

and the main cavities. The advantage here is that the external laser can be CW, thereby producing a continuous error signal for use in stabilization. Chapter 3 describes a stabilized tunable reference laser system intended for this purpose.

A.2 Auxiliary Cavity Design

The auxiliary cavity to be used for stabilization consists of three or four mirrors in a folded cavity arrangement identical to that of the corresponding high power cavity. In the final embodiment these mirrors will be mounted parallel to their main cavity counterparts. By sharing mounting platforms with the main cavity mirrors, the stability of the two cavities are coupled together.

Both cavities will have the same overall length ($L = 472\,\mathrm{mm}$), and thus, have the same nominal axial mode spacing. This is ideal for stabilization since locking the auxiliary cavity to a particular axial mode allows the main cavity to remain locked to this same mode, thus exactly matching the cavity length. A calibration procedure will be developed to match the cavity lengths precisely in case a small offset exists between them.

Using a confocal cavity geometry[22, ch.19], in which the center of curvature for each mirror lies on the opposing mirror (i.e. $s = R$), a high quality cavity mode can be achieved with considerably relaxed alignment sensitivity. A confocal cavities ease of alignment is a result of the degeneracy of all transverse modes of the cavity. Unfortunately, when such a cavity is perturbed from perfectly degenerate the transverse modes spread out in the frequency domain, making the cavity prone to mode-hopping when using PDH stabilization. For this project the cavity must maximize the frequency separations between all of the lowest order Gauss-Laguerre modes. The azimuthaly symmetric Gauss-Laguerre basis set is chosen since transverse (cartesian) cavity alignment errors are more easily compensated via mirror steering. Azimuthaly symmetric cavity mismatches are typically due to a mismatch in mode size or focussing and are much more difficult to compensate since the lenses in mode matching telescopes must be optimized.

The auxiliary cavity mirror radii are chosen such that the 20 MHz modulation sidebands used for PDH stabilization are not resonant with the higher order transverse modes of the cavity. In the event that the stabilization laser is not perfectly aligned and mode matched to the cavity some energy may couple to higher order Hermite-Guass or Guass-Laguerre cavity modes. Coupling to the higher order modes will degrade the stabilization

error signal and reduce the effectiveness of the system. The frequency of the p-th order transverse mode corresponding to the q-th axial mode is

$$\nu_{qp} = \nu_{\mathrm{ax}}(q + (p+1)\frac{\zeta}{\pi}) \tag{A.1}$$

where $\zeta = \cos^{-1}(\pm\sqrt{g_1 g_2})$ is the Guoy phase shift. $g_i = 1 - \frac{L}{R_i}$ are the cavity mirror parameters for each mirror with radius of curvature R_i[22].

A confocal geometry cavity with $\zeta/\pi = \frac{1}{2}$ offers the greatest stability but also has degenerate sets of even and odd modes. Confocal mode degeneracy can be a very useful feature due to its alignment insensitivity and stability. However, small perturbations from the confocal cavity length cause a loss of degeneracy and a broadening of the apparent cavity mode width as the higher order modes separate from the TEM_{00} mode. In order to maintain a sharp cavity resonance and allow for precision alignment exclusively to the TEM_{00} cavity mode a non-degenerate cavity must be carefully chosen. Figure A.2 illustrates the strategy used. The separation between the RF sidebands (red) and the cavity modes (black) are maximized. In this example the nearest couplings are between the $p = 4$ transverse mode and $m = -3$ sideband, and between $p = 1$ and $m = +3$.

For the values $\nu_{\mathrm{ax}} = 2856\,\mathrm{MHz}/9$ and the modulation frequency $\nu_m = 20\,\mathrm{MHz}$ the relative positions of the modulation sidebands and the cavity resonances are tabulated for various ζ/π. The mode separations for the optimized solution ($\zeta/\pi = 0.4$) are shown in Table A.1. The first three sidebands all reside between the TEM_{00} mode and the nearest higher order modes avoiding the chance of any mode degeneracy. The nearest coupling allowed is between the $p = 2$ transverse mode and the $m = -3$ modulation sideband with a separation of 0.011 axial mode separations or 3.5 MHz. Provided that the phase modulation depth is optimized for PDH stabilization there will be negligible optical power in the $m = \pm 3$ sidebands and the first even transverse mode will not be excited.

The cavity mirror reflectances are chosen to keep the mode width below 3.5 MHz to further reduce the likelihood of coupling to the $p = 2$ mode. The cavity line-width is

$$\delta\nu_{\mathrm{cav}} = \frac{\delta_{\mathrm{cav}}\nu_{\mathrm{ax}}}{2\pi} \tag{A.2}$$

where δ_{cav} is the total round trip cavity loss. $\delta\nu_{\mathrm{cav}} < 3.5\,\mathrm{MHz}$ requires that $\delta_{\mathrm{cav}} < 6.9\,\%$. A reasonable cavity design would have 3 % losses at each end mirror with $< 1\,\%$ at the third (and possibly fourth) folding mirror. The resulting cavity has a line-width of $\delta\nu_{\mathrm{cav}} = 3.03\,\mathrm{MHz}$ corresponding to a finesse of 105.

Table A.1: The distance measured in axial mode spacings between sideband m and the nearest transverse cavity mode of p-th order.

	$p=0$	$p=1$	$p=2$	$p=3$	$p=4$
$m=-3$	0.811	0.411	0.011	0.611	0.211
$m=-2$	0.874	0.474	0.074	0.674	0.274
$m=-1$	0.937	0.537	0.137	0.737	0.337
$m=0$	0.000	0.400	0.800	0.200	0.600
$m=+1$	0.063	0.337	0.737	0.137	0.537
$m=+2$	0.126	0.274	0.674	0.074	0.474
$m=+3$	0.189	0.211	0.611	0.011	0.411

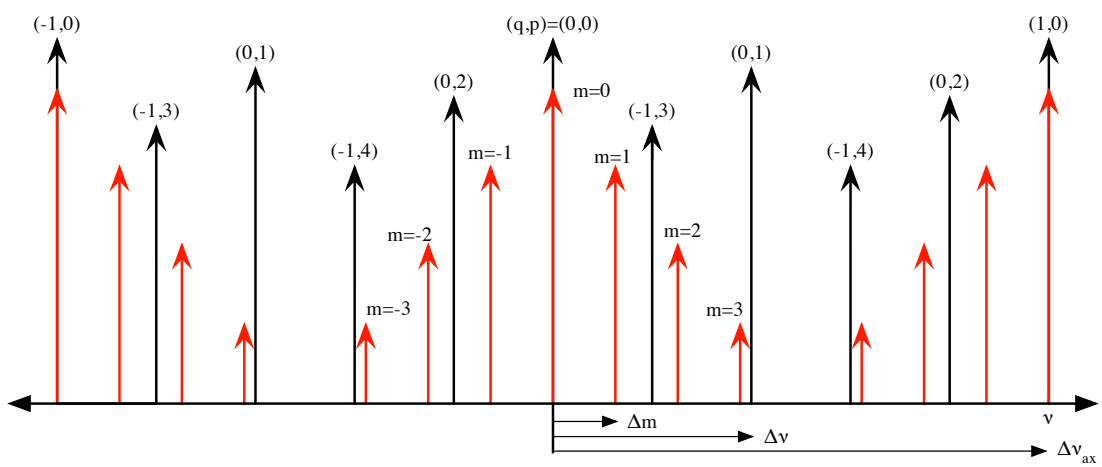

Figure A.2: In black are the p-th transverse modes for axial mode q. In red are the first three phase modulation sidebands for the input beam tuned in resonance with axial mode $q=0$. In this figure, the modulation frequency $\Delta\nu$ is exaggerated to 40 MHz. The relevant design constraint is to maximize the spacing between the low order side bands and the first few transverse modes nearby. Note that this figure is representative of a frequency comb that continues in each direction for positive and negative values of q.

A symmetric spherical cavity with the optimal Gouy phase shift of $\zeta = 0.4\pi$ has mirrors with a 683 mm radius of curvature. For a 473 mm long cavity, the waist will be $w_0 = 0.22$ mm, expanding to a 0.32 mm beam at the mirrors. Due to this small beam size, small mirrors can be mounted in close proximity to the main cavity mirrors. 5 mm diameter mirrors would provide a more than sufficient aperture for this beam. This will allow for compact and mechanically robust mounts to be shared with the main cavity mirrors.

A.3 Stabilization Principles

A Fabry-Perot optical cavity can be used as a high resolution optical frequency discriminator by examining the intensity of transmitted light near resonance. Measurement of the intensity alone is insufficient for closed-loop stabilization, however, since it does not contain any information about the direction of the deviation from resonance. The sign of this error is contained in the phase of light reflected from or transmitted through the cavity. The complex reflection coefficient for an optical cavity is given by

$$F(\nu) = \frac{E_{\text{ref}}}{E_{\text{inc}}} = \frac{r\left[\exp(\frac{i2\pi\nu}{\Delta\nu}) - 1\right]}{1 - r^2\exp(\frac{i2\pi\nu}{\Delta\nu})} \tag{A.1}$$

where (assuming a matched two-mirror cavity) r is the amplitude reflectance of each end mirror. Figure A.3 shows the intensity reflectance and phase shift for the auxiliary cavity design discussed above. Resonant frequencies ν_q are integer multiples of the cavity free spectral range ($\nu_{\text{ax}} = c/2L$). The argument of the complex reflection coefficient is the phase shift induced in light reflected from the cavity and is not directly measurable by a square law detector.

A simple phase measurement method following from microwave techniques was developed by Drever and Hall [53], and is clearly explained in a review by Black [54]. Phase modulation of the incident laser at frequency ν_m results in modulation sidebands with frequencies $\nu_0 + \nu_m$ and $\nu_0 - \nu_m$ for an optical carrier frequency ν_0 (higher order sidebands are also present). Assuming a modulation frequency such that the sidebands lie outside the cavity resonances, they will always experience a full $\pm 180°$ phase shift upon reflection and can thus be used as a fixed phase reference relative to the ideally resonant carrier.

On resonance in a matched cavity, the promptly reflected light cancels exactly with the circulating light transmitted out of the cavity producing a null net reflectance. Even a small perturbation from resonance causes the reflected carrier to interfere with the

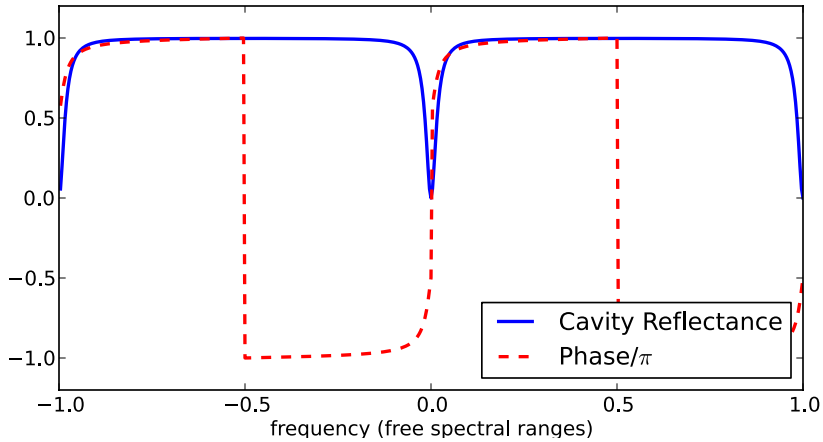

Figure A.3: The intensity reflectance and phase for the auxiliary cavity is plotted using as a function of cavity detuning using (A.1). Off-resonance the phase shift converges to a multiple of π.

modulation sidebands resulting in an amplitude modulation beat-note at the frequency ν_m. Its phase is determined by the magnitude and direction of the carrier de-tuning. Unlike the optical phase, the beat-note phase can be measured directly with an appropriate bandwidth photodetector and standard RF heterodyne techniques.

A typical Pound-Drever-Hall system configuration is depicted in Figure A.4. In this example, a 45° Faraday rotator is used to convert any light reflected from the cavity from $\hat{\mathrm{p}}$- to $\hat{\mathrm{s}}$-polarization. This $\hat{\mathrm{s}}$-polarized light is then extracted efficiently from the incident beam using a polarizing beamsplitter. A variable phase shift is included to compensate for the relative propagation delay between oscillator and photodetector signals. Harmonics of the modulation frequency are blocked by a low pass filter and the feedback amplifier converts the bipolar error signal into a control voltage for the piezo used to set the cavity length. This amplifier is typically a proportional, integral, differential (PID) controller but could be as simple as a first order integrator.

The error signal for a typical PDH system is show in Figure A.5. Clearly the steeply sloped region about the lock point is useful as a precision frequency discriminator for a feedback loop. The wide capture region provides a high integrity lock since a disturbance of more than ν_m is needed to unlock the system.

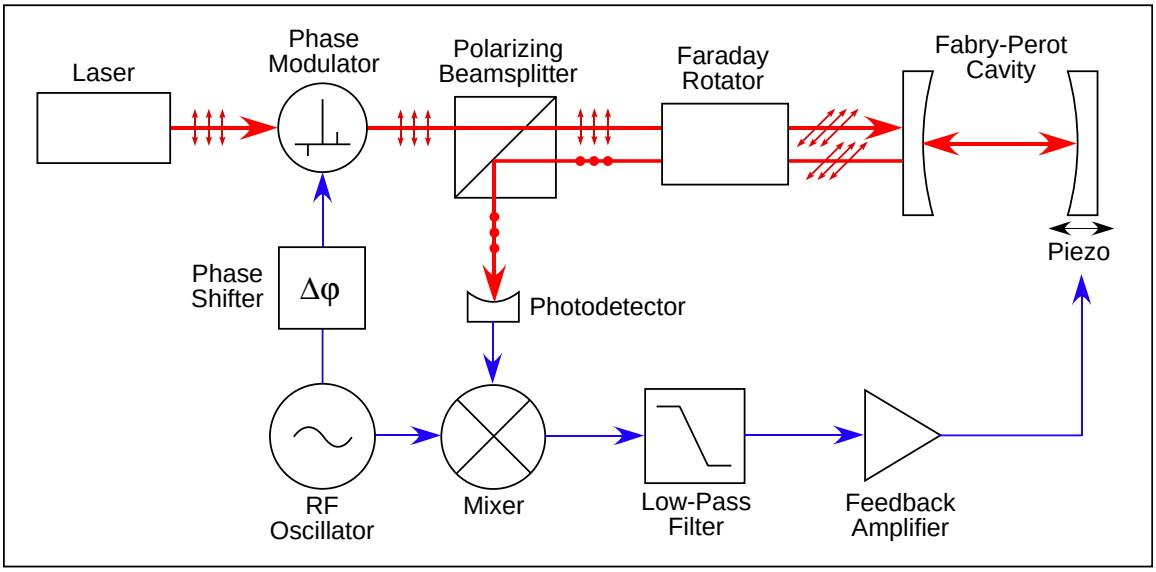

Figure A.4: The most basic example of a Pound-Drever-Hall cavity stabilization system consists of a phase modulated laser injected into a Fabry-Perot resonator. The presence of a polarizing beamsplitter and Faraday rotator allow light reflected from the cavity to be separated from the input beam and detected. The detected signal is mixed with the modulation oscillator to measure its phase. The detected phase is then used as an error signal to correct the cavity length.

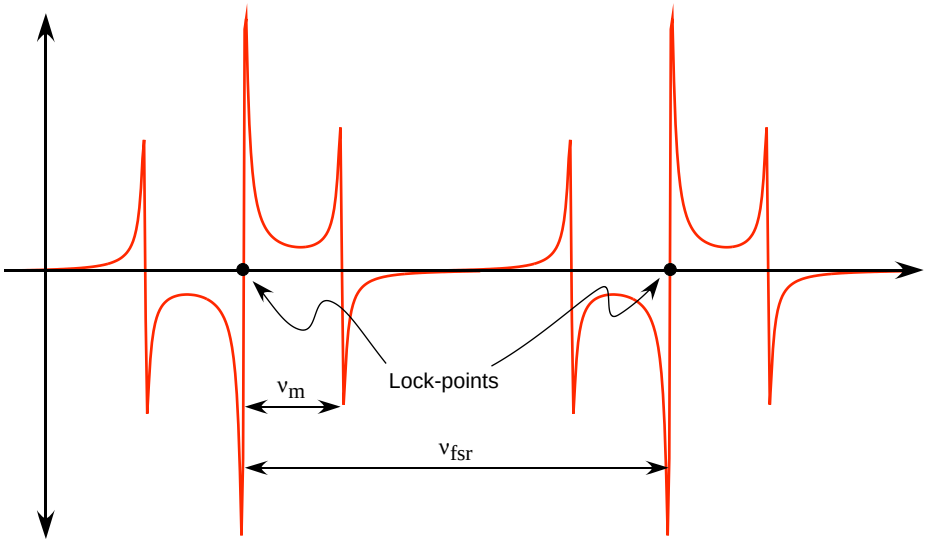

Figure A.5: A typical example of a PDH error signal shows the existence of a high slope at the lock points, surrounded by wide regions of constant sign.

A.3.1 Mode Stepping

Adjacent lock points in a PDH system are separated by one free spectral range ν_{ax} and can be selected by manual tuning of the cavity or laser before engaging the feedback loop. By choosing the modulation frequency ν_m equal to $\frac{\nu_{\text{ax}}}{2}$ the error signal waveforms for adjacent lock-points become connected as shown in Figure A.6. The capture regions for two adjacent lock points are now joined by repulsive regions with opposite slope from the lock points. If the error signal is inverted then clearly these repulsion points become lock points and vice versa. By electronically forcing the resonant mode into one of its capture regions (possibly slowing or disabling the feedback loop response), an instantaneous inversion of the signal will result in the capture by the new adjacent lock point and, thus, constitutes a controlled 'step' from one cavity mode to the next. When using a large modulation frequency, the high phase measurement bandwidth attributed to the steep error signal slope is compromised in favor of a much larger capture region and the ability to mode-step.

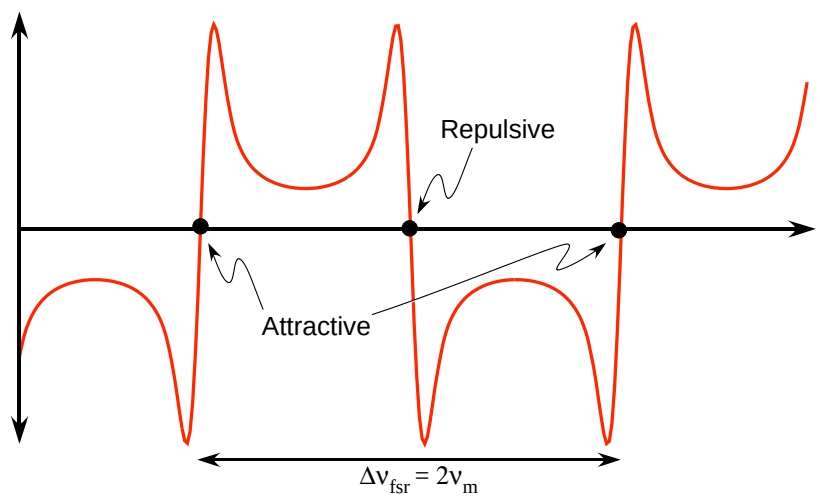

Figure A.6: When the modulation frequency equals the cavity free spectral range, the error signal is continuous with zero crossings of alternate slopes.

A.3.2 Error Signal Calculation

The real amplitude of a CW plane with frequency ν_0 and phase modulated at ν_m can be written as

$$E_{\text{in}}(t) = E_0 \sum_k \left(u_k e^{i2\pi(\nu_0 + k\nu_m)t} + \text{c.c.} \right) \tag{A.2}$$

where $u_k = J_k(\beta)$ are Bessel functions and β is the modulation depth. β can range from 0 to π depending on the amount of RF power applied to the modulator. Simulations indicate an ideal modulation depth of $\beta = 0.95$.

The wave reflected from the cavity is found by modulating (A.2) with the cavity reflectance (A.1). Let $u'_k = u_k F(\nu_0 + k\nu_m)$ and write the reflected wave reaching the detector as

$$E_{\text{ref}}(t) = E_0 \sum_k \left(u'_k e^{i2\pi(\nu_0 + k\nu_m)t} + \text{c.c.} \right) \tag{A.3}$$

The signal $S(t)$ received from the photodetector is

$$S(t) \propto [E_{\text{ref}}(t)]^2 = (\text{D.C.}) + (De^{i2\pi(\nu_o + k\nu_m)t} + \text{c.c.}) + (2\nu_m \text{ terms}) + (\nu_0 \text{ terms}) + ... \tag{A.4}$$

where only the second group of terms is retained to create an error signal. These terms are the result of the interference of frequency components separated by the modulation frequency

$$D = 2 \sum_k u'_k u'^*_{k-1} \tag{A.5}$$

Mixing this signal with the modulation signal $m(t) = \left[Me^{i(2\pi\nu_m t + \phi)} + \text{c.c.} \right]$ in a double balanced RF mixer produces the signal

$$m(t) \times S(t) = (\text{A.C. terms}) + (MD^* e^{i\phi} + c.c.) \tag{A.6}$$

where M is the amplitude of the local oscillator input to the mixer and ϕ is the relative phase shift between the RF and LO signal inputs to the mixer. Using a low pass filter the DC component can be isolated and used as the final PDH error signal

$$\epsilon = MD^* e^{i\phi} + M^* D e^{-i\phi} \tag{A.7}$$

Shown in Figure A.7 is the simplest example of a simulated PDH error signal. Here a CW laser was used with a 40 MHz modulation frequency. The depth of modulation is $\beta = 0.95$ and only the first pair of sidebands is used in the calculation. The high slope of the error signal about the central lock point ensures that any deviation will result in a large signal whose sign indicates the required direction for compensation by a piezo transducer. Since each axial mode of the cavity can be used as a PDH lock point, a low modulation frequency is used here to prevent modulation sidebands from coupling to adjacent modes and to maximize the slope of the error signal.

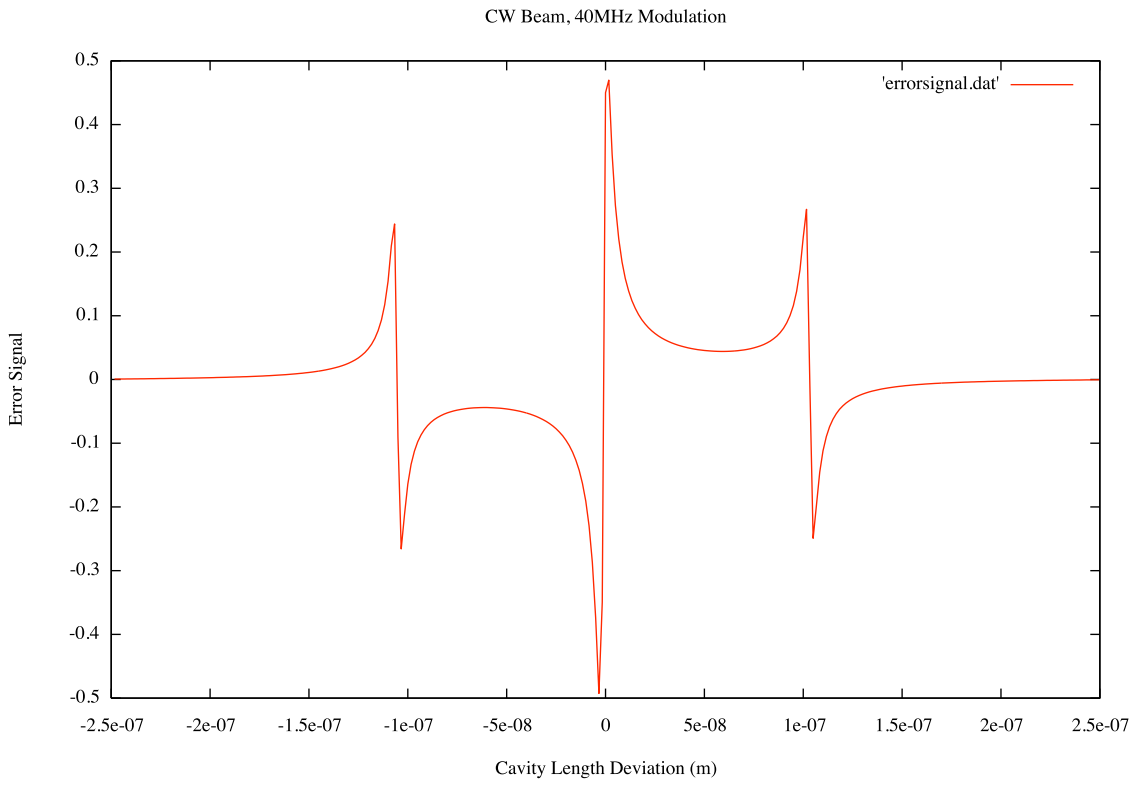

Figure A.7: Simulated PDH error signal for a CW laser with 40 MHz phase modulation.

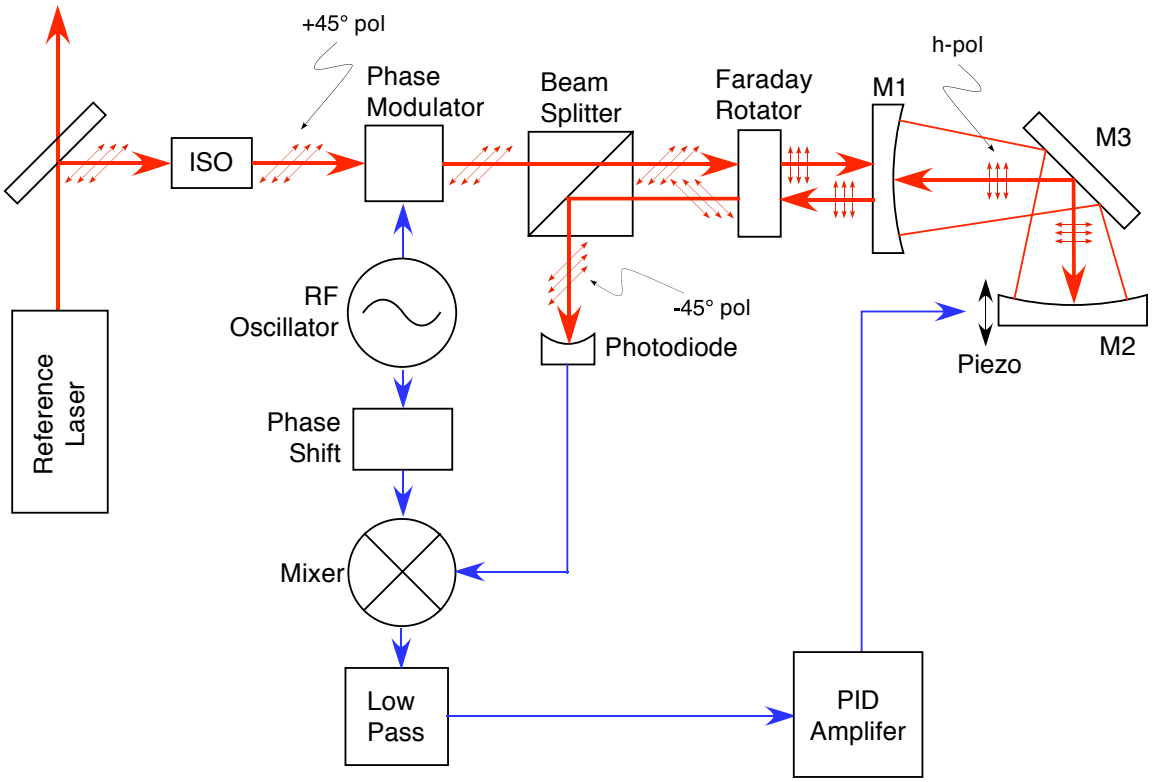

Figure A.8: The auxiliary cavity for a three-mirror storage cavity is stabilized using the PDH technique to lock it to an external reference laser.

A.4 Stabilization System Implementation

Figure A.8 shows an overview of the auxiliary cavity PDH stabilization system. The stabilized tunable reference laser from Chapter 3 serves as the light source for the auxiliary cavity. A Brewster plate (BP) is used to pick off a small fraction of the STRL light, the remainder of which is used to stabilize the FEL. A faraday isolator (ISO) must be used to prevent the PDH system from interfering with operation of the STRL and the FEL. The isolator will rotate the incident polarization by 45° so successive optical components must be mounted for use at this polarization.

The phase modulator (PM) applies sidebands to the beam at multiples of the chosen modulation frequency as described by (A.2). Another faraday isolator (FR) will be used in conjunction with a polarizing beam splitter (BS) to divert light reflected from the cavity to a fast photodetector (PD). The second isolator provides another 45° rotation so that a horizontal polarized beam is injected into the auxiliary cavity.

Finally, the beam is coupled into the auxiliary cavity with reflectance given by equation (A.1). The detailed cavity mirror design is covered in Section A.2.

A high speed photodetector is needed to capture the beat note of interest at the modulation frequency. With a modulation frequency of 20 MHz the sampling theorem states that a detector should be chosen with at least a 40 MHz bandwidth. Thus, a photodiode with a rise time of about 25 ns would be sufficient. The photodiode should also be AC coupled to remove the dominant DC component of the beam.

To generate the PDH error signal, the photodiode signal with proper amplification is combined with the modulation signal in an RF mixer (MX). Since the desired error signal is the DC component of the mixer IF output, a low pass filter will be applied to the signal.

To achieve stable control of cavity length, this error signal is processed by a PID control circuit and amplifier to provide the feedback signal required to drive the mirror piezos. The PID circuit employs a combination of proportional, integral, and differential gain to track both long and short term changes in the error signal effectively. Each of the three PID stages is independently tunable to achieve optimal performance of the feedback loop.

The piezo system itself must be able to fulfill two roles. To aid cavity alignment, first, the concentricity of the cavity will be decreased by 40 µm while the stabilization system is active. This will require the piezo to have a long reach but a relatively slow response governed by how quickly we wish to 'grow' the cavity. Second, the system must actively respond to small perturbations in the cavity length caused by thermal or vibrational disturbances. This requires a range of motion less than 10 µm with a dynamic response up to a few kHz. Due to the limitations of piezo-electric actuators, a single device will not serve both purposes. Instead we propose a stack of four identical PolyTech PI P885-50 low voltage piezo actuators, each with a 15 µm range. Three piezos linked in parallel will provide the long range DC tracking motion while a single piezo will provide the dynamic motion up to 14 µm peak-to-peak at 1 kHz. A custom control circuit will be designed to allow these four actuators to work in tandem. This circuit can also be designed to incorporate the mode stepping technique described in Section A.3.1.

A.5 FEL Stabilization

In addition to stabilization of the optical storage cavity it is important for x-ray production to have a stable pump laser. Drift in the micro-pulse phase or the optical frequency of the laser may lead to loss of synchronism when injected into the optical storage cavity. This section describes stabilization of the free electron laser resonator.

In most precision laser interferometry work it has been desirable or necessary to keep a laser precisely tuned to an interferometric reference such as a Fabrey-Perot cavity or an atomic resonance. Often this precision laser is then used to detect and measure small changes in a less stable resonator that is part of the experiment.

A free electron laser, while broadly tunable, is dependent on variations in undulator field strength (gap), electron beam energy, and cavity length for its tuning. These parameters are typically difficult to tune without disrupting system performance and require system re-optimization and/or realignment after each change. This results is very long tuning time-constants and correspondingly low feedback bandwidths, making active control difficult. Even more cumbersome is the tuning of complex multi-cavity interferometric resonators such as the MkIII FEL with an intra-cavity Michelson or Fox-Smith resonator used to phase lock the laser[21, 55].

Two issues are important to the design of a stabilization system for the FEL resonator. First, the laser is broadly tunable, which requires that the laser be reconfigurable for operation in different optical 'bands'. At the same time, the laser must also have narrow tunability within a limited bandwidth that does not require the reconfiguration of the electron beam or the undulator. Second, in order to provide feedback for resonator control, the laser light must be measured and characterized. This is not a trivial task when dealing with broadly tunable mid-infrared radiation. The mid-IR is a troublesome spectral void between efficient photonic detectors, bolometric detection, and electronic detection. To compound the lack of efficient broad spectrum detectors, the fact that this part of the spectrum is only accessible by limited fixed line lasers, free electron laser, and synchrotron light sources has inhibited the commercial development of detectors. The near-IR in contrast is extremely well served by fast commercial lasers and detectors thanks to the telecommunications industry.

A further complication to stabilization is the pulsed nature of the FEL/RF-linac system. Since the FEL light can only be sampled during the 4 µs laser macro-pulse duration,

the mechanical state of the laser is completely unknown during the intervening 100 ms delay between subsequent laser pulses. For these reasons it is desirable to adopt the same CW auxiliary cavity stabilization scheme described above for FEL resonator stabilization. In fact, the same stabilized tunable reference laser (STRL, see Chapter 3) can be used with the FEL and storage cavity concurrently, thus ensuring that the storage cavity is always synchronized to the laser. Tuning the STRL reference frequency will simultaneously tune the FEL and storage cavity resulting in precision fine tuning of the scattered x-ray energy.

Appendix B

Compton Backscattering Interaction Hardware

This section will describe the design and operation of the custom vacuum chamber and diagnostic devices which comprise the high-luminosity x-ray source. This first generation x-ray source is a single pass system in which there is only a single interaction between the electron and laser beams. A extension of this system, described later in the chapter, is an upgrade to an optical storage cavity intended to vastly increase the beam-beam interaction cross section and thus x-ray production efficiency. The primary purpose of the single pass source is to serve as a testbed and proof of principle for several technologies which will be essential to the operation of the storage cavity.

B.1 Compton Backscattering Source

Infrared photons for Compton backscattering are provided by the MkV FEL and delivered to the interaction region by an extension of the existing optical transport system [56]. An insertable mirror along the vacuum transport line serves as a switch to redirect the laser to the x-ray interaction optics. Scattered x-ray yield from the interaction point is optimized when both the laser and electron beams are tightly focused and carefully aligned such that their respective focal regions overlap longitudinally, transversely and temporally.

The beam overlap conditions and x-ray energy are optimized for a head-on collision as calculated in Section 1.4. Achieving this head-on geometry with an optical storage cavity would require that the electron beam pass through holes bored in the cavity mirrors (see [57] for example). Such an arrangement precludes the use of a diffraction limited TEM_{00}

Table B.1: Single Pass X-Ray Scattering Experiment Specifications

Wavelength	λ	3 µm
IP Rayleigh range	z_R	1 mm
IP spot size	w_0	31 µm
Beam crossing angle	α	5.75°
IP Divergence angle	$\theta_{\frac{1}{2}}$	1.77°
X-ray photon energy		10.4 keV
E-beam energy		40 MeV
E-beam emittance	ε_n	8π mm·mrad
μ-Pulse duration	τ_μ	1 ps

beam to maximize the optical power in the interaction region, and thus, the scattering efficiency. To avoid the need for electron apertures in the mirrors we introduce a crossing angle of 5.75° between the two beams; this reduces the scattered x-ray photon energy by only 0.25 %. The single pass x-ray scattering apparatus also uses a crossing angle of 5.75° to simulate the conditions of the optical storage cavity as closely as possible. This allows for prototyping and specification of as many storage cavity components as possible using a simplified system.

The laser Compton scattering source described here will use a nominal laser wavelength of 3 µm at which the MkV FEL performance is optimal. The system will also be compatible with other wavelengths constrained only by the optical aperture available. For wavelengths longer than 3 µm a smaller radius beam must be used with a correspondingly larger focal spot at the IP to avoid the wavefront perturbations due to beam truncation.

Both electron and laser beams are focused to the same nominal waist radius as for the optical storage cavity; $w_0 = 31$ µm at the interaction point (IP) at a wavelength of 3 µm. The divergence half-angle of this beam is $\theta = \frac{\lambda}{\pi w_0} = 1.77°$ which is approximately 1/3 of the crossing angle. This allows the electron and optical beams to be well separated at the mirrors.

Longer wavelengths can be used in the system if the collimated beam size is decreased, leading to a corresponding increase in focal spot size. Shorter wavelengths down through the visible pose no problem for the system as designed.

B.1.1 Electron Beam Focusing

The typical normalized emittance ε_n of the e-beam provided by the MkV microwave gun and linac is less than 8π mm·mrad. To maximize the scattered x-ray energy and optimize conditions for laser operation at 3 µm wavelength the linac will be operated at an energy of 40 MeV ($\gamma = 78.3$). When the electron beam is focused to the same size as the laser beam (30 µm) the β-function at the focus can be calculated as:

$$\beta_0 = \frac{\pi w_0^2}{\varepsilon} = 8.82\,\text{mm} \tag{B.1}$$

where $w_0 = 30\,\mu\text{m}$ is the focal spot radius and $\varepsilon = \frac{\varepsilon_n}{\gamma} = 0.102\,\pi$ mm·mrad is the beam emittance. The divergence half-angle of the electron beam is then:

$$\theta_e = \sqrt{\frac{\varepsilon}{\pi\beta_0}} = 3.40\,\text{mrad} = 0.195^\circ \tag{B.2}$$

The beam radius at any point in the far field ($z \gg \beta_0$) can be calculated as $w_e(z) = \theta_e z$.

Since $\beta_0 \gg z_R$ the electron beam is clearly collimated within the optical mode waist and good transverse overlap are assured within the optical waist.

B.1.2 Design Constraints

The shallow 5.75° crossing angle between the laser and electron requires the placement of an additional kicker mirror between the focusing optics and the interaction point (IP) in close proximity to the electron beam. A second identical kicker mirror directs the laser away from the electron beam after the IP for diagnostics and disposal. Because of the proximity to the electron beam, both of these kicker mirrors must be located within the IP vacuum chamber and be constructed from materials that will survive bombardment by a high energy electron beam. To avoid possible damage during alignment and configuration of the electron beam the kicker mirrors must be able to retract away from the beam axis in a repeatable manner.

The kicker mirrors will not be adjustable after installation and thus precision beam alignment must be performed outside the vacuum chamber. Precision transverse overlap of the laser with the electron beam is performed using a motor actuated mirror (M1) placed between the final focusing lens (F1) and the kicker mirror, outside of the vacuum system. The distance from M1 to the IP is constrained to be less than the focal length of lens F1 and large enough that the actuators are able to scan across ten times the beam radius at the IP (300 µm) with a resolution of 3 µm.

According to Siegman[22], the clear aperture diameter of any optic should be at least 4.6 times the beam radius to limit diffractive wavefront distortion. Assuming a maximum practical optic size of 2", with circular mirrors mounted at 45° incidence, the maximum beam radius in the system is limited to $w = 8\,\mathrm{mm}$.

Spherical aberration must be kept minimal in all focusing optics in order to ensure a diffraction limited spot and a pure TEM_{00} beam at the IP.

All transmissive optics will be CaF_2 for its IR transmission characteristics and resistance to radiation damage. All commercial reflective optics will have a protected silver coating such as Newport ER.2 with high performance in the IR.

B.1.3 Optical Components

The following list summarizes the optical components of the system illustrated in Figure B.1 followed by descriptions of each.

1. Optical transport mirror S (MS)
2. Collimation telescope (F2,F3)
3. Laser Attenuator (A1)
4. Optical delay line (M4,M5)
5. Turning flat (M3)
6. Beam sampler (P3)
7. Quad detector (D1) and associated optics
8. Turning flat (M2)
9. Final focus lens (F1)
10. Final steering mirror (M1)
11. Vacuum window (P1)
12. Kicker mirror (MK1)
13. Transition radiation screen (TRBPM), TV camera (D5) and mirrors.
14. Scanning wire BPM (SWBPM)
15. Bremsstrahlung Target Foil
16. Kicker mirror (MK2)
17. Vacuum window (P2)
18. Collimating lens (F4)
19. Beam sampler (P4)

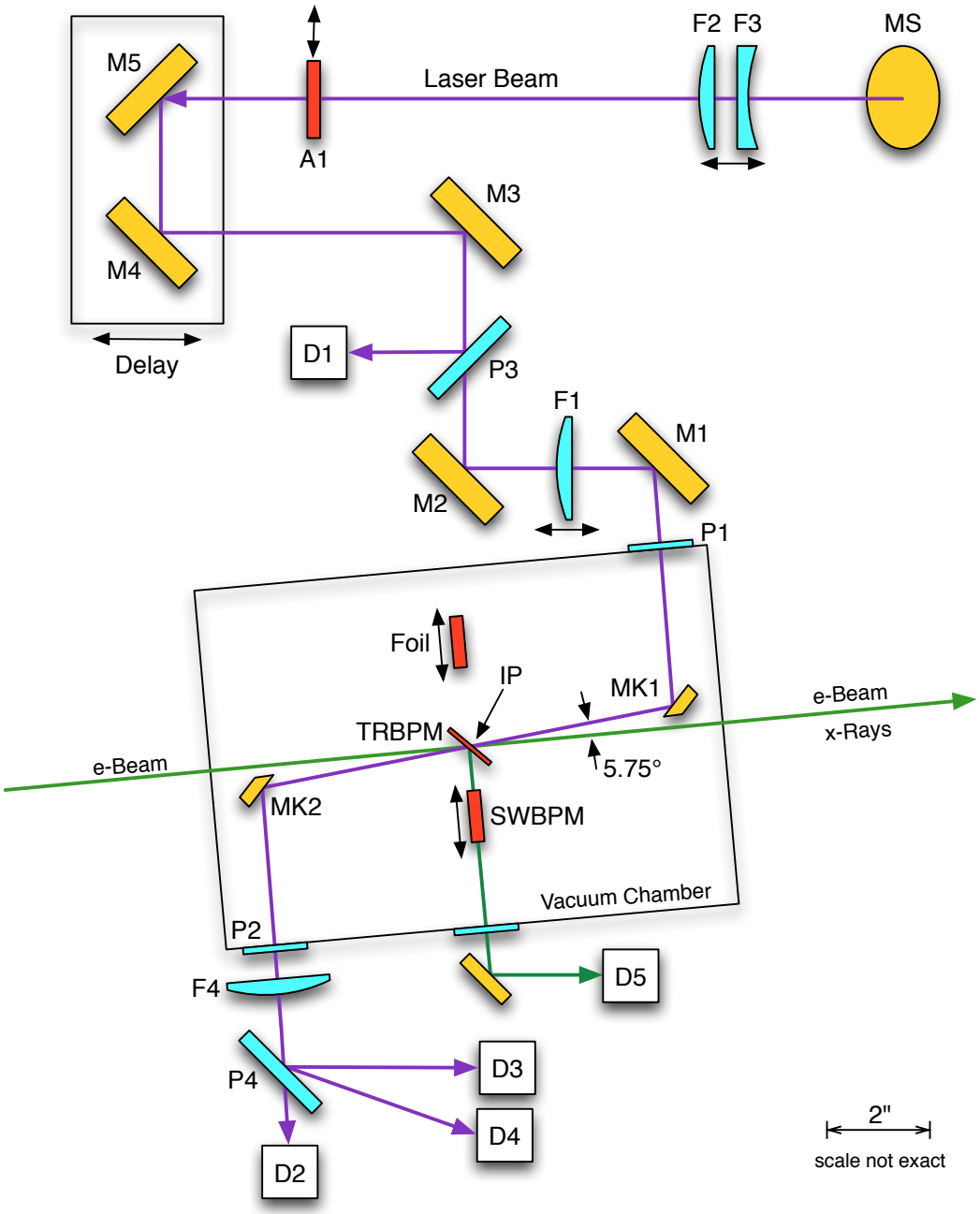

Figure B.1: The optics for the single-pass x-ray system deliver the focused laser beam to the interaction point. The input beam incident on mirror MS is collimated with the F2/3 telescope. An optical delay line is used to adjust the arrival time of pulses at the IP and lens F1 focuses the beam for scattering. Steering of the beam at the IP is accomplished with motor driven mirror M1. The output side of the vacuum chamber provides a number of beam diagnostics.

20. Pyroelectric detector (D2)
21. Quad detector (D3) and associated optics
22. FPA camera (D4) and associated optics

Turning Flats (MS,M1,M2,M3,M4,M5)

All of the mirrors on the collimated portion of the beam-line are Newport ER.2 protected silver mirrors in Thorlabs KM200 mounts. These are 2" diameter mirrors used at 45°, accommodating a maximum beam radius of 8 mm.

Matching Telescope (F2, F3)

The IR beam provided by the MkV FEL via the optical transport system has a Rayleigh range $z_R = 532\,\mathrm{mm}$ and a spot size $w_s = 6.781\,\mathrm{mm}$ at mirror S which is located at $z_s = 5061\,\mathrm{mm}$ from the laser waist. Lenses F2 and F3 form a Galilean telescope designed to collimate the beam to the desired 8.00 mm radius.

The beam radius a distance z from a waist in the far field is given by $w(z) = \sqrt{\frac{\lambda}{\pi z_R}}z$, where z_R is the Rayleigh range of the beam. The beam from the MkV laser expands to 8 mm radius at a distance $z = 5971\,\mathrm{mm}$ from the MkV waist, equivalent to a distance $z_{\mathrm{S,F3}} = 910\,\mathrm{mm}$ from mirror S. This beam could be collimated by placing an $f = z = 5971\,\mathrm{mm}$ lens at this location. Since this is not a realizable focal length, a compound lens can be constructed from two singlet lens' f_2 and f_3 separated by a distance d. The double lens formula:

$$\frac{1}{f} = \frac{1}{f_2} + \frac{1}{f_3} - \frac{d}{f_2 f_3} \tag{B.3}$$

can be simplified for the case $f_2 = -f_3$ giving $f_2 = \sqrt{fd}$. Choosing $f_2 = 259\,\mathrm{mm}$ results in a lens separation of $d = 11.2\,\mathrm{mm}$. A gaussian beam propagation simulation shows that this lens combination will focus a collimated 8 mm radius beam at a distance of 5691 mm. The distance from mirror S to lens F3 should then be $d_{\mathrm{S,F3}} = 630\,\mathrm{mm}$. This design will differ slightly for real beams and lenses but will be tuned empirically.

F2 and F3 are both CaF_2 plano-convex lenses 2" in diameter. The focal length $f_2 = -f_3 = 259\,\mathrm{mm}$ for 3 µm light was chosen since this same CaF_2 lens corresponds to a standard 250 mm focal length at 633 nm. The lens pair is mounted in a 2" lens tube with the separation adjusted by moving threaded retaining rings.

The MkV FEL alignment HeNe laser was used to adjust the telescope to collimate the beam. Using a beam of a different wavelength reduces the beam size throughout the system but preserves the Raleigh range throughout (with the exception of changes in focal length due to wavelength). At 633 nm the net focal length is 5580 mm, a deviation of only 2 % from its IR focal length. The telescope output is projected with a series of flat mirrors over the length of the FEL tunnel ($\approx$ 30 m total). The lens separation was adjusted to give the best possible collimation over this long distance by comparing the spot sizes at 15 m and 30 m.

Optical Delay Line (M4, M5)

Mirrors M4 and M5 are mounted on a 2" travel translation stage. Moving the translation stage adjusts the arrival time of the optical pulses relative to the electron pulses. The spacing between adjacent pulses is 350 ps corresponding to a distance of 105 mm (a delay covered by a translation of 2.065"). The full 2" travel is only needed during the initial setup in order to synchronize the optical and electron pulses at the IP. After the initial synchronization, fine tuning of the delay is only required over a few 1 ps pulse lengths. The motor used only has a 1" range of motion but a mechanical stop can be moved by 1" to extend the range if necessary. In the unlikely (3 %) chance that the required synchronized position lies outside the 2" stage range the entire assembly can be translated as required and the system realigned.

Beam samplers (P3,P4)

2" CaF_2 wedged beam samplers can be installed before and after the IP for diagnostic purposes. The wedges are aligned near the Brewster angle to minimize power coupled to the detectors.

Quadrant detectors (D1,D3)

Quadrant pyroelectric photodetectors positioned before and/or after the IP can aid in beam alignment. Detector D1 monitors the input beam as sampled just before the lens F1. The path lengths from P3 to F1 and D1 are matched so that D1 gives an accurate indication of the centricity of the beam in F1 when the beam is remotely steered by mirror B of the optical transport system. It is assumed that the alignment of the FEL beam

incident on mirror B will not change unless the output couplers from the MkIII optics box are serviced and thus, the alignment of the input beam is completely determined by steering mirror B. In the future, a second quadrant detector D3 may be installed after the re-collimation lens F4 to provide feedback for an active beam stabilization system.

Final Focus Lens (F1)

Focusing to the 31 µm waist at the IP is achieved by an $f_1 = 259$ mm lens positioned a distance of $z_{F1} = f_1$ from the IP. A standard lens focal length of 250 mm is specified for HeNe wavelength and scales to 259 mm when used at 3 µm. This 9 mm deviation in focal length will need to be accounted for by longitudinal translation when using the alignment HeNe for focusing adjustments. The diffraction limited gaussian beam spot size for a lens is given by:

$$ww_0 = \frac{\lambda f}{\pi} \tag{B.4}$$

The 8.00 mm collimated input beam then results in the desired IP waist radius of 31 µm.

The third order spherical aberration limited spot size is

$$2w_s = \frac{0.067 f}{(f/\#)^3} = 4.5\,\mu\text{m} \tag{B.5}$$

where $f = 259$ mm and the system $(f/\#) = \frac{\pi w_0}{2\lambda} = 15.7$[58, §1.12]. Because this aberration is much less than the 31 µm spot size, a simple spherical singlet may be used, provided the surface quality is high.

Lens F1 is mounted on a longitudinal motorized translation stage used to adjust the longitudinal position of the focus relative to the IP. Since the input beam is highly collimated, the size of the focus will remain unchanged while translating. The longitudinal adjustment is needed to ensure overlap of the waists of both beams at the IP. This stage has a 12 mm range so that both the IR beam and visible HeNe can be focussed to the same point with one lens.

Final Steering Mirror (M1)

Mirror M1 is located at $z_m = 212$ mm from the IP and is steered to adjust the transverse overlap of the optical and electron beams. The beam size at M1 is $w_m = 6.75$ mm which requires a mirror with horizontal dimension 1.73" at 45° incidence. A standard 2" flat mirror is used with motorized actuators for remote control. M1 is mounted on a micrometer

driven translation stage to center the beam in the mirror during coarse steering in the initial alignment.

Vacuum Windows (P1, P2)

Laser light enters and exits the vacuum chamber through 0.125" × ⌀1.25" CaF_2 windows at normal incidence. The windows are wedged to avoid etalon effects and are mounted directly on the vacuum chamber wall, held by a retaining flange against an O-ring seal.

Kicker mirrors (MK1, MK2)

The IP kicker mirrors are positioned 4" to either side of the IP at 50.41° incidence. This angle assumes that the incident laser beam is aligned perpendicular to the axis of the optical table, the ebeam is angled at 5.071° from the table axis, and the crossing angle is 5.75°. The spot size at $z_k = 4" = 101.6\,\text{mm}$ is $w_k = 3.25\,\text{mm}$. The electron and laser beam separation here is 10.2 mm with an e-beam radius of 0.35 mm.

To avoid electron beam damage to the mirror 5.5 mm of space will be left between the e-beam axis and the mirror edges. This provides an optical aperture of 4.5 mm (looking along the beam axis) or 2.77 times the beam radius. This is much less than the nominal 4.6 times aperture, but power loss is only 0.3 % and since this clipping is only on one edge of the mirror, minimal wavefront distortion will occur at the IP.

The IP kicker mirrors are silver coated flat copper mirrors. Mirror dimensions are 0.75" square with one edge cut back at 45° to reduce interference with e-beam. The optical beam will be centered 6.40 mm from the angled edge of the mirror. V-grooves will be machined into the top and bottom edges of the mirror substrate for kinematic mounting between three 3/32" balls (see Figure B.2.)

Re-collimation Lens (F4)

Lens F4 serves the reverse role of lens F1 by re-collimating the beam for use with output beam diagnostics.

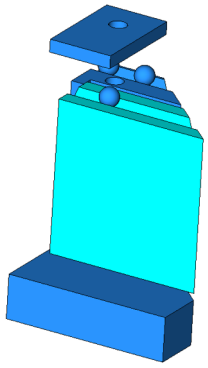

Figure B.2: The kicker mirror mount assembly precisely aligns the mirrors using a ball and groove kinematic design. These mounts are easily removable through ports in the vacuum chamber for service.

Table B.2: Kicker Mirror Specifications

Substrate Material	OFHC Copper
Surface Dimensions	(0.750" $\times$ 0.750") $\pm$ 0.002"
Thickness	0.250" $\pm$ 0.002"
Flatness	$\lambda/10$ P-V @ 633 nm
Scratch-Dig	15-5
Clear Aperture	95 %
Groove Depth	0.050" $\pm$ 0.001"
Groove Angle	45°

Output beam diagnostics (D2, D3, D4, P4)

After it has scattered from the electron beam the 'used' laser beam can be monitored by several diagnostic instruments. The high power beam passing through P4 is 'dumped' into pyroelectric detector D2 for raw pulse energy measurements. The two surface reflections from wedged sampler P4 can be monitored by quad detector D3 for alignment stabilization (via M1) and an infrared focal plane array D4.

Camera D4 allows for measurements of the mode quality and size. While not strictly necessary for this single pass x-ray system, the camera will be an essential feature for the optical storage cavity design. Investigation of possible camera technologies to fit the system requirements is ongoing. Depending on the detector technologies and geometries chosen, additional beam focussing and attenuation optics may be required.

B.2 Opto-mechanics

The kicker mirrors are installed on retractable mounts within the vacuum chamber so that the MkV diagnostic chicane is able to run in other beam focusing configurations without damaging the mirrors or causing beam loss due to the reduced aperture. The design for the mirror retraction mechanism is shown in Figures B.3 and B.4. A pneumatically actuated linkage system rotates the mirror stages about loosely fit pivot rods. When inserted, the stages register against three-point kinematic ball-groove seats and loses contact with the pivot rods. Kicker mirror mounts will be attached to the stages such that they can be easily serviced through access ports in the vacuum chamber in the event of mirror damage. Kicker mirror alignment will be fixed at installation and determined by precisely machined physical stops.

A collimated HeNe laser beam was used to verify the alignment of the scattering chamber optical components. For alignment purposes the TR screen was replaced with a paper screen with a precision laser printed reticle centered at the IP (see Figure B.5). With the chamber fully assembled with the exception of the upstream service flange, the HeNe was aligned using the following procedure:

1. HeNe laser is collimated with a two lens telescope with a confocal range much greater than the maximum working distance.

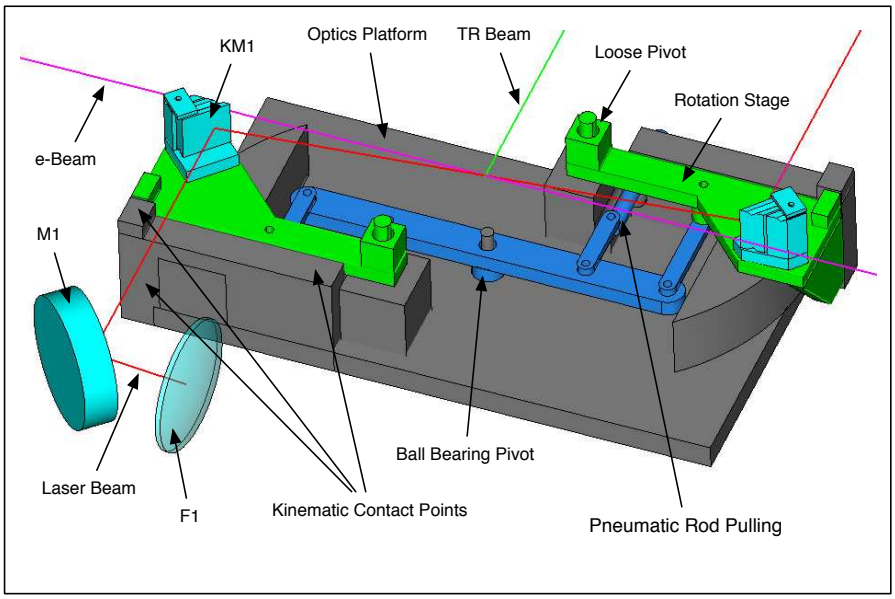

(a) Mirrors Inserted

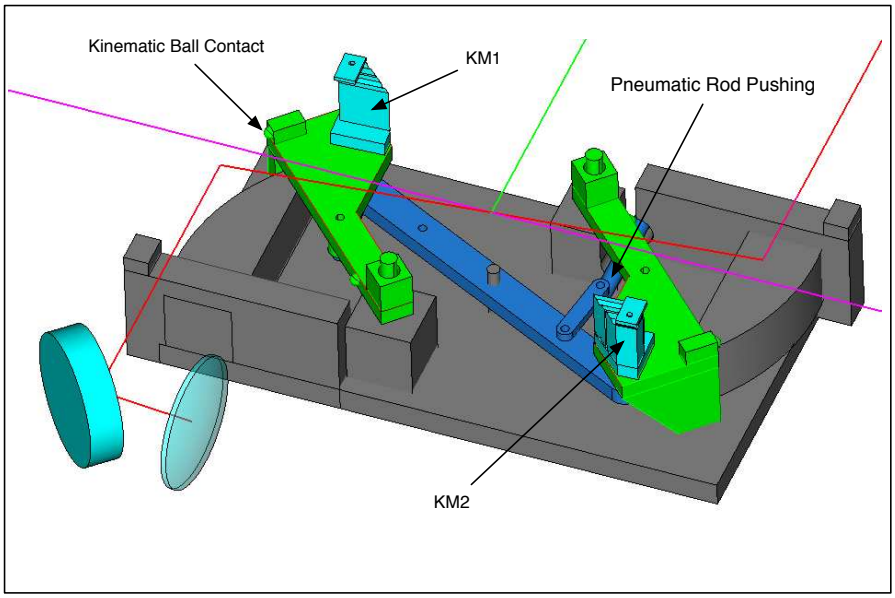

(b) Mirrors Retracted

Figure B.3: The kicker mirror retraction assembly swings the mirror stages away from the electron beam using a pneumatic actuator and linkage system.

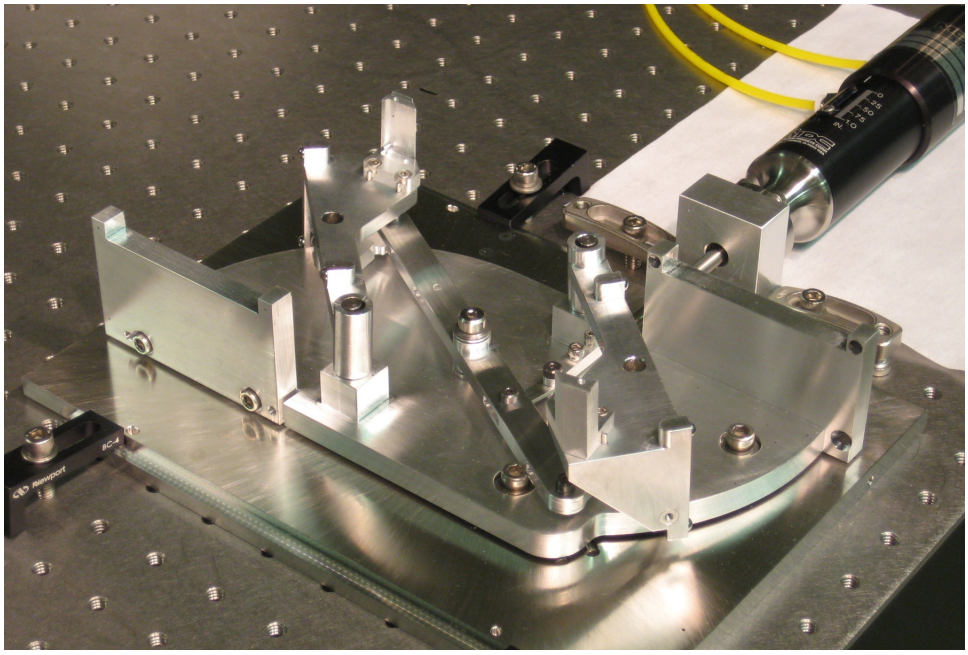

Figure B.4: The fully assembled mirror insertion mechanism is shown mounted on the floor of the vacuum chamber before assembly. The aluminum optics platform is mounted with a self aligning ball and groove design and is removable.

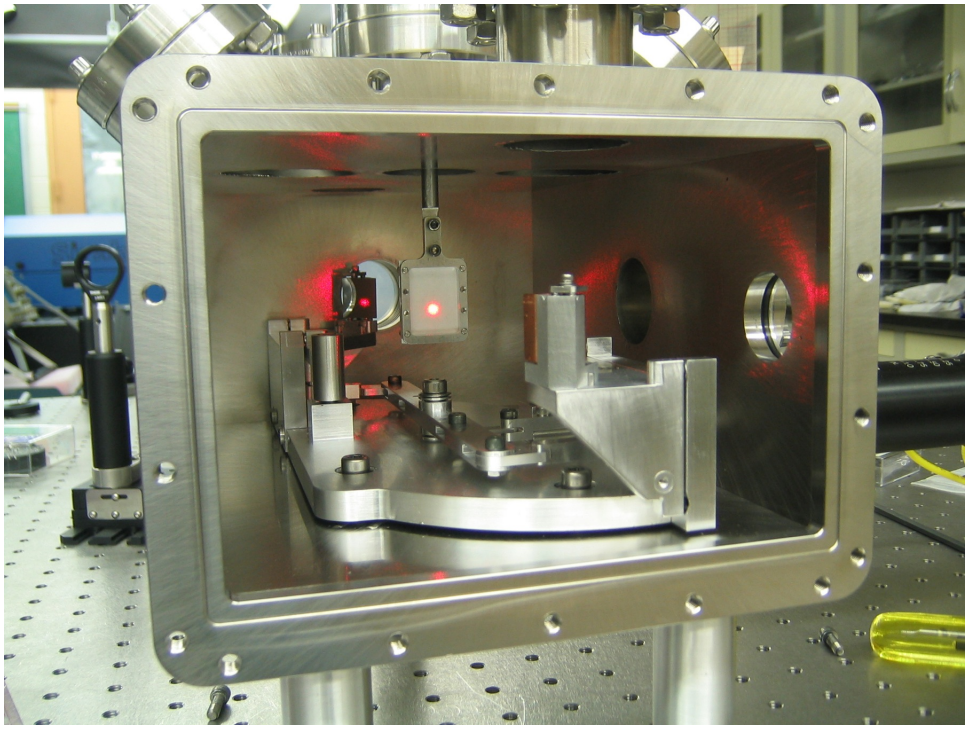

Figure B.5: The interior of the assembled vacuum chamber is shown with the upstream flange removed. The alignment HeNe beam can be seen on the far kicker mirror and on the paper alignment screen.

2. Using two flat turning mirrors, the beam is centered in the entrance and exit windows (P1 and P2). Note that due to the wedge angle of the windows the input and output beams are not necessarily parallel to the table.

3. Visual inspection of the beam position on the kicker mirrors (MK1 and MK2) shows that the spots are correctly positioned (centered vertically and 0.25" from the knife edge of the mirror).

4. The beam position on the IP target screen is within 0.5 mm of the horizontal center. The insertion depth of the actuator was set to center the beam vertically using the beam position to define the vertical plane.

5. This procedure was repeated with an uncertainty limited by the visual size of the beam.

The paper screen remains installed at the IP until this same procedure is used to align the laser injection optics on the MkV beamline with the chamber under vacuum. After the wire scanner records position of the aligned beam, the alignment screen is replaced with the final copper TR screen. The wire scanner calibration is then used to verify all future optical alignment.

Over ten cycles of the pneumatic mirror insertion mechanism the beam deflection measured on a CCD camera 1.27 m away. This experiment indicates that the beam position at the IP has an uncertainly of just 1.2 µm horizontally and 0.3 µm vertically over repeated actuations. This is negligible compared with the desired laser spot size of 31 µm at the IP. Over a two hour period the beam deflection drifts by about 12 µm. However, the motion is oscillatory about the starting position with a period ranging from 6 min to 20 min, which is consistent with typical cycles of the building air conditioning. The temperature at the final installation site on the MkV beamline is better controlled and this drift should prove negligible over an experimental run.

B.3 Vacuum Chamber Design

The x-ray interaction chamber shown in figure B.6 was fabricated from 1/4" thick stainless steel plates welded to a 3/8" thick stainless steel base plate in the form of a box. Stock ConFlat nipples are welded into precision machined ports. The internal dimensions of

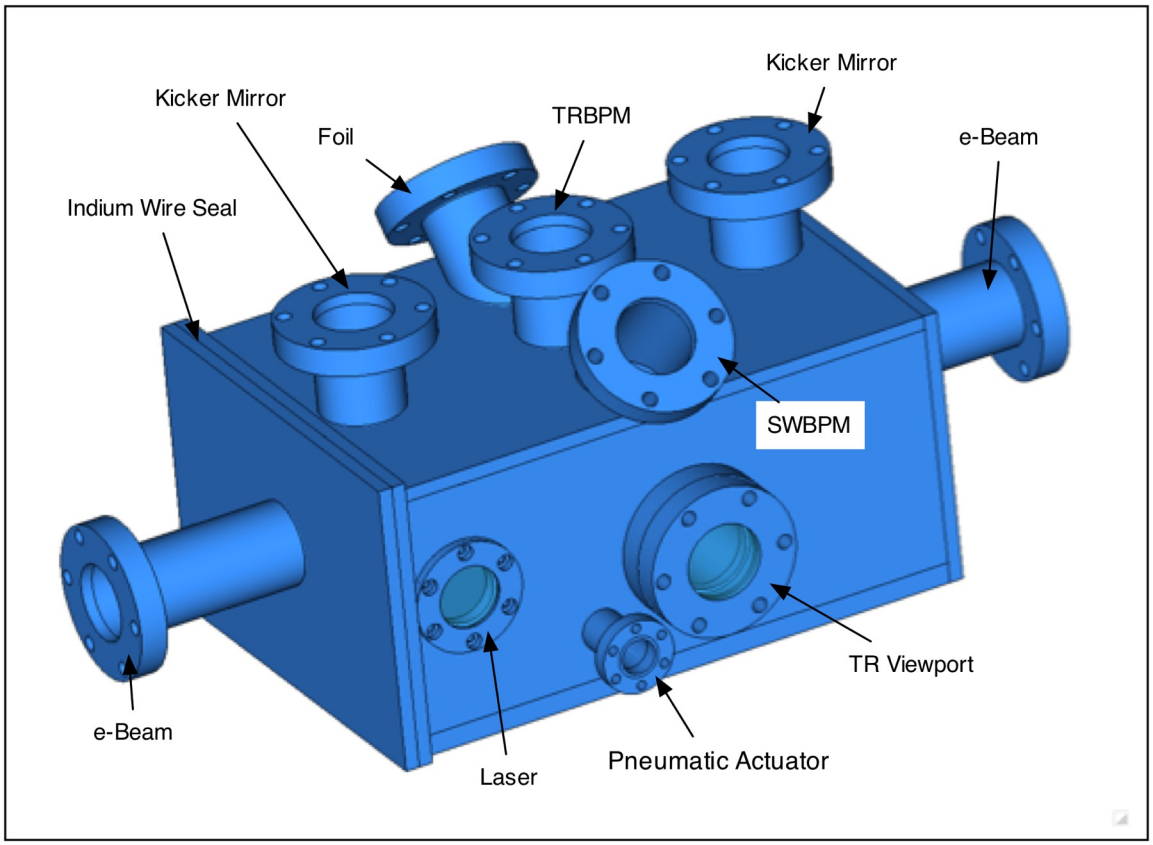

Figure B.6: The vacuum chamber provides three ports for insertion devices along with laser windows, a view port, and a pneumatic actuator motion feedthrough.

the box are 10.000" × 7.500" × 4.375" high. Dowel pins inserted into precisely drilled holes were used to align the panels for assembly and welding. Due to careful design, clamping, and welding procedures, TIG welding caused negligible distortion to the shape of the box. The final assembled dimensions match the design to within 0.002" after welding.

The chamber is secured to the beamline optical table after alignment by three legs with custom made aluminum mounting brackets. The chamber height is permanently set by the length of the legs. Figure B.7 shows the completed vacuum chamber installed in the MkV diagnostic chicane with its insertion devices installed.

B.3.1 Insertion Device Ports

Three of the flanges protruding from the top of the box are for the three insertion devices, the wire scanner (SWPBM), transition radiation screen, and bremsstrahlung foil.

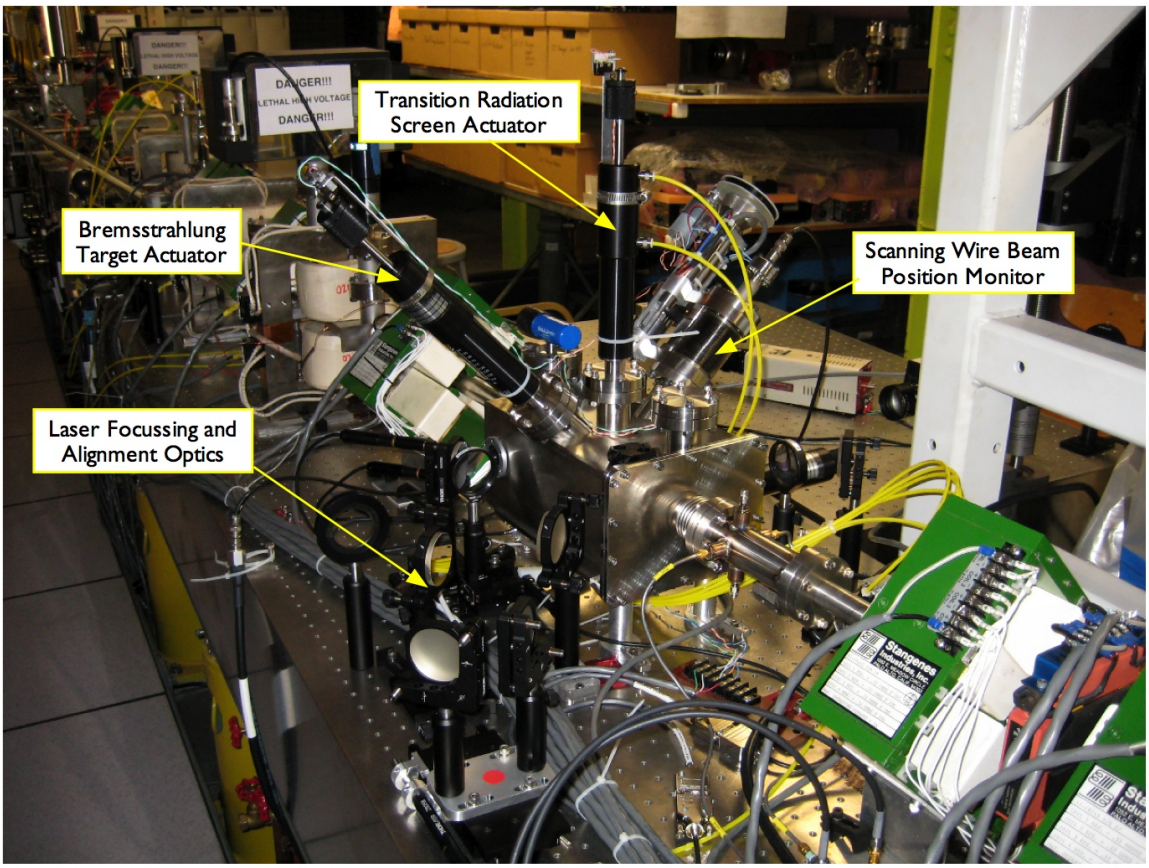

Figure B.7: The x-ray scattering chamber is installed in the MkV diagnostic chicane beamline. Three insertion devices and laser transport optics are also installed.

Standard 2.75” ConFlat flanges are used with 1.5” diameter pipes oriented 45° from one another and aligned radially from the e-beam axis. The interior surface of the chamber top plate is positioned 2” above the beamline so that the three 1.5” pipe penetrations in the plate are separated by 3/16” gaps for welding.

The faces of the 45° flanges are exactly 5” from the beam and the vertical flange face is 4” from the beamline. These distances were chosen to allow sufficient clearance for installation and tightening of nuts and bolts on each flange. All three flanges are rotatable and have clearance holes so that angular alignment of the insertion devices is possible. The angular alignment was well preserved during welding.

B.3.2 Laser Window Flanges

The ⌀1.25” windows P1 and P2 are mounted directly on the side walls of the vacuum chamber with o-ring seals. The windows are held in place by ⌀2” × 1/4” thick aluminum retaining flanges with six #6-32 screws each. The glands for ⌀1.25” × 1/16” thick o-rings are machined directly into the chamber walls leaving a 1.100” clear aperture for the beam. Buna-N o-rings are be used due to their superior radiation resistance in proximity to the electron beam.

B.3.3 Transition Radiation Port

Light from the transition radiation screen is viewed through a quartz viewport mounted on a 2.75” ConFlat flange welded to the side panel of the vacuum chamber. The quartz window is transmissive from ultra-violet to mm wavelengths and was chosen to provide access to as much of the TR spectrum as possible for a variety of experiments including measurements of THz radiation.

B.3.4 Pneumatic Actuator Port

The rotatable kicker mirror stages are actuated by the MDC #662000 1” pneumatic linear actuator. The actuator is mounted parallel to the TR port on a ConFlat mini-flange. The pneumatic actuator provides a piston surface area of $0.88\,\mathrm{in}^2$ delivering 53 lbs of force at 60 psi.

Full insertion of the mirror stages is accomplished when the pneumatic actuator is in its retracted state. The actuator does not provide a settable stop for this state so that

the full force of the actuator is used to seat the mirror stages. Since the stage retraction mechanisms on the optics platform are mounted kinematically in the chamber and held in place by springs, care must be taken not to unseat these kinematic points when the mirror stage is being pulled by the pneumatic actuator. A combination of spring tension and air pressure was chosen to satisfy this requirement.

The mirror stages are in their retracted position when the pneumatic actuator is inserted against its adjustable stop. This stop must be set appropriately to avoid impacting the mirror stages against the inner wall of the vacuum chamber.

B.3.5 Kicker Mirror Service Ports

Two additional vertically oriented flanges, identical in design to the TR screen port, are positioned directly above the two kicker mirrors. These 1.5" diameter ports provide sufficient access to the kicker mirrors for replacement if needed. One of these service ports is fitted with a Convectron gauge tube to monitor the vacuum pressure during pump-down and let-up.

Also accessible through the downstream service port is one of the retaining screws for the kinematic support platform. This platform is the common base for all components of the retractable mirror mechanism. The upstream retaining screws are accessible through main upstream service flange.

B.3.6 E-beam Ports

The electron beam enters and exits the vacuum chamber through 2.75" ConFlat flanges at the ends of the chamber. These flanges are mounted on flexible bellows to mechanically decouple the vacuum chamber alignment from the rest of diagnostic chicane vacuum system. The upstream e-beam port is attached to a 1/4" plate that mates to a flange on the vacuum chamber with an indium wire seal. The downstream e-beam port is permanently attached to the 1/4" wall of the vacuum chamber.

B.3.7 Vacuum Chamber Floor

The floor of the vacuum chamber is a 3/8" thick stainless steel plate. Three pair of hardened steel ⌀1/4" dowel pins form rails embedded in the plate oriented radially from the interaction point. Three steel balls attached to the bottom of the optics platform rest

on these rails and serve to self center it about the IP. The platform is then secured by three springs tensioned by screws to provide downward pressure. This design was chosen to ensure that the optics platform is unaffected by distortion of the vacuum chamber due to welding, clamping, or thermal expansion. Any relative expansion between the steel chamber and the aluminum platform will result in the balls sliding radially along the grooves, thus, maintaining centering.

Both longitudinal sides of the chamber floor protrude beyond the side walls by 1/4" with a thickness of 1/4" for use as reference surfaces for alignment. These surfaces are precision machined and separated from any welding seams; this separation also allows them to be easily reached with various gauging tools used to align the chamber.

B.3.8 Vacuum Chamber Alignment

With the top halves of the quadrupole magnets and the beam pipe removed in the vicinity of the IP a theodolite was precisely sighted along the electron beamline. A cylindrical target was fabricated with precision crosshairs centered exactly on the beamline center when inserted in a quadrupole magnet. This target was sighted at the upstream and downstream most quads to align the theodolite. Using the theodolite the chamber was installed such that the center of the paper alignment screen was aligned to the beamline. The theodolite was also used to establish a scribe line on the optical table parallel to the beamline. This line was then verified against the positions of the existing quadrupole magnets and used to rotate the chamber parallel to the beamline. A jig was assembled to then translate the chamber perpendicular to the beamline into its final position such that the alignment screen is again centered in the theodolite sight.

B.4 Electron Beam Diagnostics

In addition to housing the laser optics used to facilitate the Compton backscatter interaction, the scattering chamber serves as a platform for several important diagnostic tools. Three ports in the scattering chamber allow three independent insertion devices to have access to the interaction point. The insertion device geometry is shown in Figure B.8 and a Figure 5.4 shows the completed scattering chamber assembly.

In order to optimize the x-ray interaction it is necessary to detect very low initial x-ray fluxes in real time. However, in order to see these x-rays, the detector must be carefully

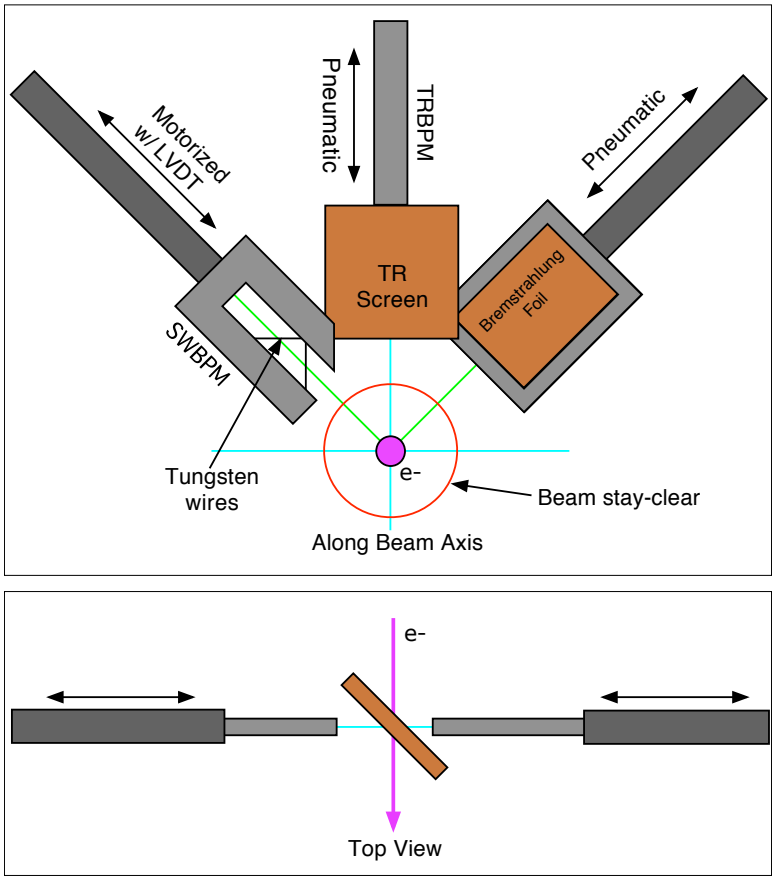

Figure B.8: The interaction point insertion devices are oriented at ang45 with respect to one another allow access to the IP from the top of the chamber. The TR screen is oriented at 45° incidence so that radiation can be imaged through the viewport on the side of the chamber. Retracted devices must be designed to stay clear of the region mark by the red circle to avoid collisions.

aligned to the 0.7° divergence beam 10 m away. A thin foil inserted into the electron beam at the interaction point can serve as an intense source of bremsstrahlung radiation. This radiation has a much broader spectrum than the Compton-backscatter source and thus significantly lower brightness. It is, however, perfectly co-aligned to the Compton x-ray source with similar beam divergence, without any alignment or synchronization sensitivity. The bremsstrahlung radiation also retains the picosecond time structure of the electron beam making it an ideal alignment and calibration source.

The bremsstrahlung source consists of a pneumatic actuator on the scattering chamber used to insert a 0.001" thick copper foil suspended on an aluminum frame into the electron beam at the interaction point. The ability to easily toggle between the bremsstrahlung and Compton x-ray sources with the press of a button will greatly aid in the alignment and calibration of the fast x-ray detector and associated electronics.

The second interaction point diagnostic is a transition radiation screen that may be inserted into the electron beam as a visual diagnostic. The TR screen consists of a 1 mm thick copper screen attached to a pneumatic actuator. The screen is inserted into the electron beam at 45° incidence so that the transition radiation exits chamber through a viewport oriented at 90° to the beamline. Images are then captured using a radiation tolerant Vidicon-tube TV camera for viewing and capture in the control room. Figure B.9 shows an image captured at the TR screen for calibration. In addition to the incoherent visible transition radiation, there exists the possibility to observe the coherent THz transition radiation produced by the screen via this viewport with an appropriate detector.

Development is also underway for a micro-pulse synchronization system using the TR screen. The relative phase between the electron bunches and laser pulses is adjusted using the delay stage described in Section B.1.3. TR light and laser coherent spontaneous radiation at the IP will be observed with a high speed photomultiplier tube with both beams following identical optical paths. The 2856 MHz component of the signal is mixed with a phase reference in the same phase measurement apparatus used by the feed-forward system described in Chapter 4. Nulling the relative phase between the two light sources ensured that the micro-pulses arriving at the interaction point are perfectly synchronized[59].

The final interaction point diagnostic is the scanning wire beam profiler, which is the subject of Chapter 5. The wire scanner is used to precisely measure the size and positions of both the electron and laser beams at the interaction point.

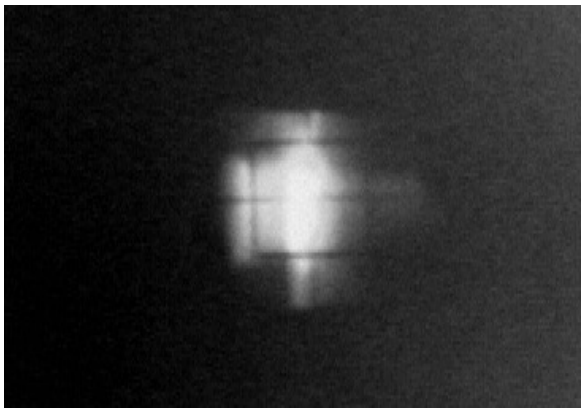

Figure B.9: The e-Beam is imaged at the IP using the TR screen. A large diameter beam is used in this image in order to fully illuminate the reticle for calibration. The reticle lines visible in the picture are separated by 0.1" for an image resolution of (35 µm × 35 µm) per pixel.

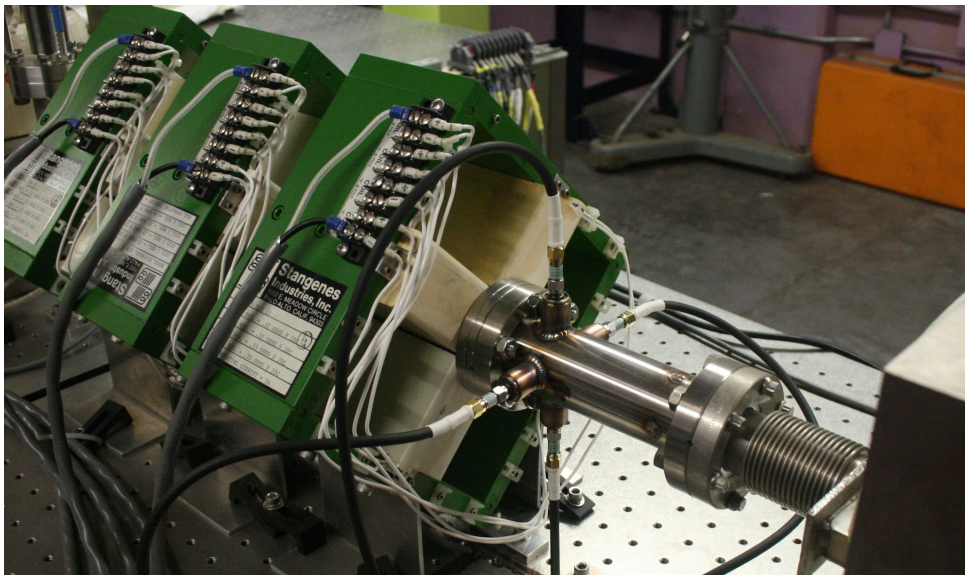

Figure B.10: Four strip-line beam position monitors are installed on the diagnostic chicane to monitor the beam position in real time for precise alignment to the quadrupole magnets and IP.

Other important diagnostics for x-ray generation are the strip-line beam position monitors (BPMs) installed before and after the scattering chamber. Figure B.10 shows one of the four BPMs installed on the MkV beamline. A comprehensive system of readout electronics developed at the University of Hawai'i allows the beam position to be precisely measured in real time at several beamline locations and displayed in the control room[60]. This system provides a precise and repeatable means of aligning the electron beam through the diagnostic chicane and x-ray interaction point. In order to sustain the intense free electron laser beam required for x-ray production, the alignment and focusing of the electron beam must remain optimized continuously. Thus, there is no way to independently control the electron beam alignment within the interaction region. The electron beam focal properties and alignment can only be adjusted before the laser operations begin. The strip-line BPMs provide a much more precise and repeatable means of recreating a painstakingly tuned electron beam configuration than is possible using images obtained from transition radiation screens.

B.5 Conclusion

The x-ray scattering chamber has performed as expected since installation and transmission and focusing of the infrared FEL beam has been demonstrated. The alignment and functionality of the kicker mirror retraction mechanism has been stable and has not required service in the 2.5 years since installation. The wire scanner has been successfully used to verify the alignment and focusing of the beam with the results presented in Chapter 5. Work is presently underway on an RF phase comparison technique to synchronize the arrival of electron and laser pulses at the interaction point.

Appendix C

Ray Tracing Equations

This appendix contains the vector analysis used to develop the ray tracing code described in Section 2.3.3.

C.1 Cylindrical Mirrors

Definitions:

$$\mathbf{p} \equiv \text{point on the surface of a cylinder} \tag{C.1}$$

$$\mathbf{a} \equiv \text{point on the cylinder axis} \tag{C.2}$$

$$\hat{\mathbf{n}} \equiv \text{unit vector along cylinder axis} \tag{C.3}$$

$$\mathbf{c} \equiv \text{surface normal at the point } \mathbf{p} \tag{C.4}$$

The equation of a cylinder with radius R, arbitrary position, and orientation is

$$||(\mathbf{p} - \mathbf{a}) \times \hat{\mathbf{n}}|| = R \tag{C.5}$$

An arbitrary ray can be parameterized as

$$\mathbf{p} = \hat{\mathbf{u}}t + \mathbf{s} \tag{C.6}$$

where $\hat{\mathbf{u}}$ gives the direction and $\mathbf{s}$ is the point of origin.

To find the intersection of the ray with the cylinder we insert (C.6) into (C.5) and solve the resulting quadratic for t, the position along the ray.

$$|(\hat{\mathbf{u}}t + \mathbf{s} - \mathbf{a}) \times \hat{\mathbf{n}}|^2 = R^2 \tag{C.7}$$

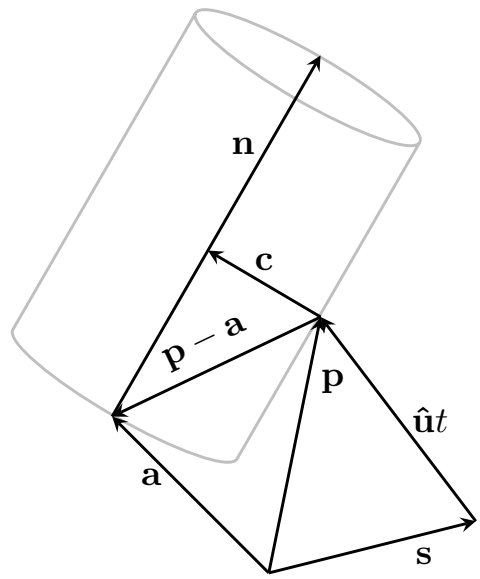

Figure C.1: Intersection of a line with a cylindrical surface

using the vector identities $|\mathbf{A} \times \mathbf{B}|^2 = |\mathbf{A}|^2|\mathbf{B}|^2 - (\mathbf{A} \cdot \mathbf{B})^2$ and $\hat{\mathbf{n}} \cdot \hat{\mathbf{n}} = 1$ yields

$$0 = |\hat{\mathbf{u}}t + \mathbf{s} - \mathbf{a}|^2 - ((\hat{\mathbf{u}}t + \mathbf{s} - \mathbf{a}) \cdot \hat{\mathbf{n}})^2 - R^2 \tag{C.8}$$

$$\begin{aligned} &= t^2 + s^2 + a^2 + 2t\hat{\mathbf{u}} \cdot (\mathbf{s} - \mathbf{a}) - 2(\mathbf{s} \cdot \mathbf{a}) - R^2 \\ &\quad - [t^2(\hat{\mathbf{u}} \cdot \hat{\mathbf{n}})^2 + (\mathbf{s} \cdot \hat{\mathbf{n}})^2 + (\mathbf{a} \cdot \hat{\mathbf{n}})^2 \qquad \text{(C.9)} \\ &\quad + 2t(\hat{\mathbf{u}} \cdot \hat{\mathbf{n}})(\mathbf{s} - \mathbf{a}) \cdot \hat{\mathbf{n}} - 2(\mathbf{s} \cdot \hat{\mathbf{n}})(\mathbf{a} \cdot \hat{\mathbf{n}})] \end{aligned}$$

This equation is then solved for t using the quadratic formula

$$t = \frac{-B \pm \sqrt{B^2 - 4AC}}{2A} \tag{C.10}$$

where A, B, C are given by

$$A = 1 - (\hat{\mathbf{u}} \cdot \hat{\mathbf{n}})^2 \tag{C.11}$$

$$B = 2(\mathbf{s} - \mathbf{a}) \cdot (\hat{\mathbf{u}} - (\hat{\mathbf{u}} \cdot \hat{\mathbf{n}})\hat{\mathbf{n}}) \tag{C.12}$$

$$C = s^2 + a^2 - R^2 - 2(\mathbf{s} \cdot \mathbf{a}) - ((\mathbf{s} - \mathbf{a}) \cdot \hat{\mathbf{n}})^2 \tag{C.13}$$

this quadratic gives the two values of t for which the ray intersects the cylinder.

The surface normal to the cylinder at the point $\mathbf{p}$(t) is

$$\mathbf{c} = (\mathbf{a} - \mathbf{p}(t)) - ((\mathbf{a} - \mathbf{p}) \cdot \hat{\mathbf{n}})\hat{\mathbf{n}} \tag{C.14}$$

$$\hat{\mathbf{c}} = \frac{\mathbf{c}}{||\mathbf{c}||} \tag{C.15}$$

We are only interested in the concave focusing surface so a test must be performed to select the t for which $\hat{\mathbf{c}} \cdot \hat{\mathbf{u}} < 0$.

C.2 Planar Surfaces

A plane in space with normal vector $\hat{\mathbf{n}}$ and containing the point $\mathbf{b}$ is described by

$$\hat{\mathbf{n}} \cdot (\mathbf{p} - \mathbf{b}) = 0 \tag{C.1}$$

intersection with the ray $\mathbf{p} = \hat{\mathbf{u}}t + \mathbf{s}$ can be easily solved or t

$$t = \frac{\hat{\mathbf{n}} \cdot (\mathbf{b} - \mathbf{a})}{\hat{\mathbf{n}} \cdot \hat{\mathbf{u}}} \tag{C.2}$$

C.3 Paraboloid

A paraboloidal reflector is not as easily represented in vector form. We start with a paraboloid with its axis of symmetry along the $\hat{\mathbf{x}}$ axis, and its apex at the origin. The focal length f is defined as the distance from the axis to the surface contour that reflects a ray incident along the $\hat{\mathbf{x}}$ axis at 90°. This surface is described by

$$0 = \frac{z^2 + y^2}{2f} - x \tag{C.1}$$

For convenience, we shift the coordinates such that point $z = -f, y = f/2$ is at the origin. Now, a ray incident on the origin $\mathbf{p} = (0, 0, 0)$ will reflect at 90°. The surface equation is now

$$0 = \frac{(z - f)^2 + y^2}{2f} - \frac{f}{2} - x \tag{C.2}$$

To find the intercept point of the ray $\mathbf{p} = \hat{\mathbf{u}}t + \mathbf{s}$ we insert its components into (C.2) and solve resulting quadratic equation for t.

$$0 = \frac{(u_x t + s_z - f)^2 + (u_y t + s_y)^2}{2f} - \frac{f}{2} - u_x t - s_x \tag{C.3}$$

$$\begin{aligned} &= t^2 \left(\frac{u_z^2 + u_y^2}{2f} \right) + t \left(\frac{2u_z s_z - 2u_z f + 2u_y s_y}{2f} - u_x \right) \\ &\quad + \left(\frac{s_z^2 + f^2 - 2s_z f + s_y^2}{2f} - \frac{f}{2} - s_x \right) \end{aligned} \tag{C.4}$$

we substitute into the quadratic formula in (C.10) with the parameters

$$A = \frac{u_z^2 + u_y^2}{2f} \tag{C.5}$$

$$B = \frac{2u_z s_z - 2u_z f + 2u_y s_y}{2f} - u_x \tag{C.6}$$

$$C = \frac{s_z^2 + f^2 - 2s_z f + s_y^2}{2f} - \frac{f}{2} - s_x \tag{C.7}$$

The surface normal at point $\mathbf{p}(t)$ is found by taking the gradient of (C.2)

$$\mathbf{n} = -\nabla \left(\frac{(z-f)^2 + y^2}{2f} - \frac{f}{2} - x \right) \tag{C.8}$$

$$= -\hat{\mathbf{x}} + \frac{y}{f}\hat{\mathbf{y}} + \frac{z-f}{f}\hat{\mathbf{z}} \tag{C.9}$$

$$\hat{\mathbf{n}} = \frac{\mathbf{n}}{||\mathbf{n}||} \tag{C.10}$$

C.4 Reflection

The law of reflection in vector form for an ray incident in direction $\hat{\mathbf{u}}$ on a surface with normal $\hat{\mathbf{n}}$ is

$$\hat{\mathbf{r}} = \hat{\mathbf{u}} - 2(\hat{\mathbf{n}} \cdot \hat{\mathbf{u}})\hat{\mathbf{n}} \tag{C.1}$$

Bibliography

[1] J.D. Hunter. Matplotlib: A 2D Graphics Environment. *Computing in Science Engineering*, 9(3):90 –95, may-june 2007. URL: http://matplotlib.org, doi:10.1109/MCSE.2007.55.

[2] Fernando Pérez and Brian E. Granger. IPython: A system for interactive scientific computing. *Comput. Sci. Eng.*, 9(3):21–29, May 2007. URL: http://ipython.org, doi:10.1109/MCSE.2007.53.

[3] M. Ettus. Universal software radio peripheral (USRP). Ettus Research LLC http://www.ettus.com.

[4] J.M.J. Madey and E.B. Szarmes. High efficiency monochromatic x-ray source using an optical undulator, June 3 2008. US Patent 7,382,861.

[5] FR Arutyunian and VA Tumanian. The Compton effect on relativistic electrons and the possibility of obtaining high energy beams. *Physics Letters*, 4(3):176–178, 1963. doi:10.1016/0031-9163(63)90351-2.

[6] R.H. Milburn. Electron scattering by an intense polarized photon field. *Physical Review Letters*, 10(3):75–77, 1963. doi:10.1103/PhysRevLett.10.75.

[7] R.H. Milburn, C. Bemporad, N. Tanaka, and M. Fotino. High-energy photons from compton scattering of light on 6.0-GeV electrons. *Physical Review*, 138(6B):1546–1549, 1965.

[8] Light source facilities. http://www.lightsources.org/cms/?pid=1000098, 2012.

[9] The Linac Coherent Light Source (LCLS). http://lcls.slac.stanford.edu/, 2012.

[10] The European XFEL. http://www.xfel.eu/, 2012.

[11] G. Priebe, D. Filippetto, O. Williams, YM Saveliev, LB Jones, D. Laundy, MA MacDonald, GP Diakun, PJ Phillips, SP Jamison, et al. Status of the inverse Compton backscattering source at Daresbury Laboratory. *Nuclear Inst. and Methods in Physics Research, A*, 2009. doi:10.1016/j.nima.2009.05.090.

[12] Valery Telnov. Principles of photon colliders. *Nuclear Instruments and Methods in Physics Research Section A: Accelerators, Spectrometers, Detectors and Associated Equipment*, 355(1):3–18, 1995.

[13] D. Bakalov, F. Brandi, G. Cantatore, G. Carugno, S. Carusotto, F. Della Valle, A. De Riva, U. Gastaldi, E. Iacopini, P. Micossi, E. Milotti, R. Onofrio, R. Pengo, F. Perrone, G. Petrucci, E. Polacco, C. Rizzo, G. Ruoso, E. Zavattini, and G. Zavattini. The measurement of vacuum polarization: The pvlas experiment. *Hyperfine Interactions*, 114:103–113, 1998. doi:10.1023/A:1012610102642.

[14] Thomas Heinzl. Strong-field QED and high-power lasers. *International Journal of Modern Physics A*, 27(15):1260010, 2012. doi:10.1142/S0217751X1260010X.

[15] E. Szarmes. Optical cavity for coherent superposition of optical pulses, May 12 2009. US Patent 7,532,649.

[16] Todd I. Smith, Paul Haar, and H. Alan Schwettman. Pulse stacking in the SCA/FEL external cavity. *Nuclear Instruments and Methods in Physics Research Section A: Accelerators, Spectrometers, Detectors and Associated Equipment*, 393(1-3):245–251, 1997. doi:10.1016/S0168-9002(97)00486-5.

[17] A. Bacci, C. Maroli, V. Petrillo, A.R. Rossi, L. Serafini, and P. Tomassini. Compact x-ray free-electron laser based on an optical undulator. *Nuclear Instruments and Methods in Physics Research Section A: Accelerators, Spectrometers, Detectors and Associated Equipment*, 587(2-3):388 – 397, 2008.

[18] Bryce T. Jacobson. *Design, Commissioning, and Operation of MkV Electron Beam Diagnostic Chicane*. PhD thesis, University of Hawai‘i at Mānoa, 2011.

[19] AGR Thomas, CP Ridgers, SS Bulanov, BJ Griffin, and SPD Mangles. Numerical calculations of a high brilliance synchrotron source and on issues with characterizing strong radiation damping effects in non-linear Thomson/Compton backscattering experiments. *arXiv preprint*, 2012. arXiv:1204.5259.

[20] V. Yanovsky, V. Chvykov, G. Kalinchenko, P. Rousseau, T. Planchon, T. Matsuoka, A. Maksimchuk, J. Nees, G. Cheriaux, G. Mourou, et al. Ultra-high intensity-300-TW laser at 0.1 Hz repetition rate. *Optics Express*, 16(3):2109–2114, 2008. doi:10.1364/OE.16.002109.

[21] E.B. Szarmes, A.D. Madden, and J.M.J. Madey. Optical phase locking of a 2.86-GHz harmonically mode-locked free-electron laser. *JOSA B*, 13(7):1588–1597, 1996. doi:10.1364/JOSAB.13.001588.

[22] A. Siegman. *Lasers*. University Science Books, Sausalito, CA, 1986.

[23] Barry Lienert. Zemax simulation of a four mirror cavity. Private Communication, March 2012.

[24] ISO/TR 11146-1:2005: Lasers and laser-related equipment — test methods for laser beam widths, divergence angles and beam propagation ratios — part 1: Stigmatic and simple astigmatic beams, 2005.

[25] PP Crooker, WB Colson, and J. Blau. Representation of a gaussian beam by rays. *American Journal of Physics*, 74:722, 2006. doi:10.1119/1.2201857.

[26] S. Fourmaux, S. Payeur, A. Alexandrov, C. Serbanescu, F. Martin, T. Ozaki, A. Kudryashov, and JC Kieffer. Laser beam wavefront correction for ultra high intensities with the 200 TW laser system at the Advanced Laser Light Source. *Optics Express*, 16(16):11987–11994, 2008. doi:10.1364/OE.16.011987.

[27] S.A. Reed. *Electron and proton acceleration using the 30 TW, 30 fs Hercules laser*. PhD thesis, The University of Michigan, 2008.

[28] S.W. Bahk, P. Rousseau, TA Planchon, V. Chvykov, G. Kalintchenko, A. Maksimchuk, GA Mourou, and V. Yanovsky. Characterization of focal field formed by a large numerical aperture paraboloidal mirror and generation of ultra-high intensity (10^{22}W/cm^2). *Applied Physics B: Lasers and Optics*, 80(7):823–832, 2005. doi:10.1007/s00340-005-1803-8.

[29] D. Burns, G.J. Valentine, W. Lubeigt, E. Bente, and A.I. Ferguson. Development of high average power picosecond laser systems. *Proc SPIE*, 4629:4629–18, 2002. doi:10.1117/12.469492.

[30] V. Telnov. Photon collider at TESLA. *Nuclear Instruments and Methods in Physics Research Section A: Accelerators, Spectrometers, Detectors and Associated Equipment*, 472(1):43–60, 2001. doi:10.1016/S0168-9002(01)01161-5.

[31] G. Klemz, K. Mönig, and I. Will. Design study of an optical cavity for a future photon collider at ILC. *Nuclear Instruments and Methods in Physics Research Section A: Accelerators, Spectrometers, Detectors and Associated Equipment*, 564(1):212–224, 2006. doi:10.1016/j.nima.2006.03.017.

[32] Eric B. Szarmes. An RF technique for cavity length synchronism, June 2002. Private Communication.

[33] K. Kuboki and M. Ohtsu. Frequency offset locking of algaas semiconductor lasers. *IEEE Journal of Quantum Electronics*, 23(4):388–394, 1987. doi:10.1109/JQE.1987.1073362.

[34] R. Wynands and A. Nagel. Precision spectroscopy with coherent dark states. *Applied Physics B: Lasers and Optics*, 68(1):1–25, 1999. doi:10.1007/s003400050581.

[35] O. Ishida, H. Toba, and F. Kano. Optical sweeper with double-heterodyne frequency-locked loop. *Electronics Letters*, 25(22):1495–1496, 1989. doi:10.1049/el:19891003.

[36] K. Kuboki, GH Shin, T. Kato, and M. Ohtsu. Performance and its evaluation of optical tracking generator/optical frequengy synthesizer by semiconductor lasers. *Conference on Precision Electromagnetic Measurements, CPEM 88 Digest*, pages 24–25, 1988. doi:10.1109/CPEM.1988.671153.

[37] P. Horowitz and W. Hill. *The Art of Electronics*. Cambridge University Press, New York, 1989.

[38] M. Prevedelli, T. Freegarde, and TW Hansch. Phase locking of grating-tuned diode lasers. *Appl. Phys. B*, 60:S241–S248, 1995.

[39] Samuel M. Goldwasser. Sam's Laser FAQ. http://www.repairfaq.org/sam/laserfaq.htm, 2012.

[40] Eric Blossom. Gnu radio: tools for exploring the radio frequency spectrum. *Linux J.*, 2004(122):4–, June 2004. http://gnuradio.org.

[41] K. Kuboki and M. Ohtsu. An Allan variance real-time processing system for frequency-stability measurements of semiconductor lasers. *IEEE Transactions on Instrumentation and Measurement*, 39(4):637–641, 1990.

[42] NumPy: Numerical python. `http://numpy.scipy.org/`.

[43] CJ Hawthorn. Littrow configuration tunable external cavity diode laser with fixed direction output beam. *Review of Scientific Instruments*, 72(12):4477, 2001. `doi:10.1063/1.1419217`.

[44] Eric B. Szarmes. Free electron laser performance simulations. Private Communication, Feb 2012.

[45] wxPython GUI Toolkit. `http://wxpython.org`.

[46] E.B. Szarmes. Classical free-electron laser theory. Unpublished course reader, August 1998.

[47] Eric B. Szarmes. Free electron laser dynamic desychronism. Technical report, University of Hawai'i at Mānoa, 2012.

[48] R. J. Bakker, G. M. H. Knippels, A. F. G. van der Meer, D. Oepts, D. A. Jaroszynski, and P. W. van Amersfoort. Dynamic desynchronization of a free-electron laser resonator. *Phys. Rev. E*, 48:R3256–R3258, Nov 1993. `doi:10.1103/PhysRevE.48.R3256`.

[49] RI Cutler, J. Owen, and J. Whittaker. Performance of wire scanner beam profile monitors to determine the emittance and position of high power CW electron beams of the NBS-Los Alamos racetrack microtron. *Proc of the PAC-1987*, 625, 1987.

[50] MC Ross, JT Seeman, E. Bong, L. Hendrickson, D. McCormick, and L. Sanchez-Chopitea. Wire scanners for beam size and emittance measurements at the SLC. In *IEEE Particle Accelerator Conf., San Francisco, CA*, 1991. `doi:10.1109/PAC.1991.164580`.

[51] Stephen P. Malton. *Laser Interactions with High Brightness Electron Beams*. PhD thesis, University College London, 2007.

[52] Chad B. McKee. *Creation, Transport, and Measurment of Bright Relativistic Electron Beams*. PhD thesis, Duke University, 1994.

[53] R. W. P. Drever, J. L. Hall, F. V. Kowalski, J. Hough, G. M. Ford, A. J. Munley, and H. Ward. Laser phase and frequency stabilization using an optical resonator. *Applied Physics B: Lasers and Optics*, 31:97–105, 1983. doi:10.1007/BF00702605.

[54] E.D. Black. An introduction to Pound-Drever-Hall laser frequency stabilization. *American Journal of Physics*, 69:79–87, January 2001. doi:10.1119/1.1286663.

[55] E.B. Szarmes. Phase locked free electron laser with rational mode locking, 2003. US Patent 6,643,314.

[56] M.R. Hadmack. Optical transport system extension for x-ray experiments. Design Report AHI01-BLDG-3271-002-3D, University of Hawai‘i at Mānoa, 2008.

[57] I.V. Pogorelsky, I. Ben-Zvi, T. Hirose, S. Kashiwagi, V. Yakimenko, K. Kusche, P. Siddons, J. Skaritka, T. Kumita, A. Tsunemi, et al. Demonstration of 8×10^{18} photons/second peaked at 1.8 Å in a relativistic Thomson scattering experiment. *Physical Review Special Topics-Accelerators and Beams*, 3(9):90702, 2000. doi:10.1103/PhysRevSTAB.3.090702.

[58] CVI Melles Griot. Fundamental optics guide, 2012. https://www.cvimellesgriot.com/Products/Documents/TechnicalGuide/Fundamental-Optics.pdf.

[59] Eric B. Szarmes. Proposed mirror assembly for synchronizing e-beam and laser micropulses at IP. Private Communication, Feb 2012.

[60] B.T. Jacobson, M.R. Hadmack, J.M.J. Madey, and P. Niknejadi. Modular logarithmic amplifier beam position monitor readout system at the University of Hawai‘i. In *Proceedings of IBIC2012, Tsukuba, Japan*, 2012.